Analysis of Liquid Sheet Breakup and Characterisation of Plane Prefilming and Nonprefilming Airblast Atomisers

Vom Fachbereich Maschinenbau
an der Technischen Universität Darmstadt
zur
Erlangung des Grades eines Doktor-Ingenieurs (Dr.-Ing.)
genehmigte

DISSERTATION

Vorgelegt von

Umesh Chandra Bhayaraju
aus Hyderabad, Indien

Berichterstatter:	Prof. Dr.-Ing. C. Tropea
Mitberichterstatter I:	Prof. Dr.-Ing. R. Mönig
Mitberichterstatter II:	Prof. Dr.-Ing. M. Hampe
Tag der Einreichung:	20th Juni, 2007
Tag der Mündlichen Prüfung:	30th August, 2007

Darmstadt 2007

D17

Erklärung

Hiermit erkläre ich, dass ich die vorliegende Dissertation selbständig verfasst und nur die angegebenen Hilfsmittel verwendet habe. Ich habe bisher noch keinen Promotionsversuch unternommen.

Darmstadt, den 20th Juni, 2007

Umesh Chandra Bhayaraju

ACKNOWLEDGEMENTS

The following work is performed during my activities as a Researcher at Institute of Propulsion Technology, DLR Cologne, Germany.

I would like to thank Prof. Cameron Tropea at TU Darmstadt for being my Guide and first referee for my dissertation work. I had good discussions with him during my presentations at the university. His valuable suggestions on my work are greatly acknowledgeable.

I would like to thank Prof. Reinhard Mönig, Director, Institute of Propulsion Technology, DLR Cologne, for giving me an opportunity to work at the Institute. It was a brilliant experience to be part of a highly professional research environment.

I would like to thank Dr.-Ing. Christoph Hassa, at Institute of Propulsion Technology, DLR Cologne, for providing an opportunity to carry out research work on two-phase flows at LPP test rig and supervising my Doctorate work for the past 4½ years. He has been a constant source of knowledge, encouragement and support through out this work. I had wonderful time discussing about intricacies of measurements and how to go about solving varied technical problems. I appreciate his patience and his positive attitude during the course of the project.

I wish to thank my colleague Dr.-Ing. Thomas Behrendt for his support during PDA measurements at LPP test rig. I wish to express my gratitude to Michael Rachner for assisting me in several ways in and out of DLR. I wish to thank Dr. Christian Willert for lending me his PIV software. I wish to thank Gigacentre, Köln for allowing me to use their Laptop facility to write my dissertation in late nights.

I wish to thank my colleagues Fabrice Giuliani, Julian Becker, Johannes Koopman, Ulrich Meier, Olaf Diers, Dennis Schneider, Timea, Stefan, Johannes Heinze, Martin, Stefan Glum and my friends Ramesh, Krishna for making my stay at DLR a memorable event. I wish to thank Marco Putz for manufacturing several accessories during experimental campaigns and assisting me in maintenance of LPP test rig.

Finally, I wish to thank my family for being a constant source of courage and inspiration for my studies.

Cologne, June 2007

Umesh Chandra Bhayaraju

TABLE OF CONTENTS

LIST OF FIGURES

LIST OF TABLES

NOMENCLATURE

Latin characters	*units*	*description*
a	m/s²,	acceleration of a particle,
	mm	half width of liquid sheet
C^*		Efficiency of atomisation
C_D	-	drag coefficient of a droplet
D	µm	diameter
d	µm	diameter
k	1/m	space coefficient
f, F	Hz	frequency
$GSMD$	µm	global SMD
L	mm	ligament spacing
l	mm	prefilming length
m	kg/s	mass flow rate
P	bar	pressure
q	-	Momentum flux ratio,
	-	constant
Q	-	fraction of total volume of a certain diameter class
n	-	wave number, refractive index
N		droplet count
s	µm	slit width
SMD	µm	diameter based on volume to surface of droplet
t	s	time

t	μm	thickness
T	K	temperature
u	m/s	velocity
U	m/s	velocity in transverse direction
v	m/s	velocity
V	m/s	velocity in axial direction
V	m^3/s	volume flux
X	-	constant
x , y, z	mm	coordinates
X, Y, Z	-	coordinate axes

Greek characters	***units***	***description***
μ	kg/m.s	dynamic viscosity
ρ	kg/m^3	density
σ	N/m	surface tension
β	-	growth rate
α	°	scattering angle
τ	s, N	time, shear force
υ	m^2/s	kinematic viscosity
Φ	°	scattering angle
Δ	-	dispersion of spray
δ	μm	fringe spacing
ψ	°	Brewster angle
λ	nm	wave length
θ	°	angle between beams

Subscripts	***description***
10	mean diameter
20	diameter based on surface of droplet
30	diameter based on volume of droplet
32	diameter based on Volume to Surface of droplet
0.1	10% volume undersize diameter
0.5	50% volume undersize diameter
0.9	90% volume undersize diameter
a, A	air
c	characteristic
k	kerosene
l	liquid
L	length
m, max	maximum
min	minimum
mean	mean
vol	volume
o	initial, minimum
p	particle
r	ratio
rel	relative
rex	relaxation time
rms	root mean square

Superscripts	*description*
-	time averaged
,	ratio

Non-Dimensional Numbers		*Definition*
Oh	(Ohnesorge Number)	$\frac{\mu_l}{(\rho_l \sigma d_o)^{0.5}}$
Re	(Reynolds Number)	$\frac{u_a D}{\upsilon}$
Bo	(Bond Number)	$\frac{D^2 a \rho_k}{\sigma}$
We	(Weber Number)	$\frac{\rho_a u_{rel}^2 t_l}{\sigma}$
ST	(Strouhal Number)	$\frac{fD}{u_a}$
St	(Stokes Number)	$\frac{\tau_{rex}}{\tau}$
T_u	(Turbulent Intensity)	$\frac{u_{rms}}{u}$

Abbreviation	*description*
AFR	Air to Fuel Ratio
CCD	Charge Coupled Device
ICAO	International Civil Aviation Organisation
IR	Infra Red
LDA	Laser Doppler Anemometry
LDI	Lean Direct Injection
LIF	Laser Induced Fluorescence
LPP	Lean Premixed Prevapourised
LP(P)	Lean Premixed and Prevapourised
PDA	Phase Doppler Anemometry
PIV	Particle Image Velocimetry
RMS	Room Mean Square
RQL	Rich-Burn Quick-Quench Lean-Burn
SC	Staged Combustion
SMD	Sauter Mean Diameter
SNR	Signal to Noise Ratio

CHAPTER 1

INTRODUCTION

1.1 INTRODUCTION

Aircraft engines produce emissions that are similar to other emissions resulting from fossil fuel combustion. However, aircraft engines emissions are unusual as a significant proportion is emitted in the upper altitudes of the atmosphere. These emissions give rise to important global environmental concerns like the depletion of the ozone layer, formation of cirrus clouds and also on local air quality at ground level near airports. The details of emissions and their effects are reported in the ICAO report [39]. The report stresses the reduction of NO_x, CO_2 and unburnt hydrocarbons by aircraft engines.

The situation of emissions by aircraft is aggravated by increasing levels of combustor inlet pressure and temperatures. Several concepts like RQL, LPP, LP(P), LDI, SC are developed to reduce NO_x emissions by aircrafts. These concepts require high degree of homogeneity and rate of mixing of liquid fuel with air in the combustor. The initial phase of mixing of liquid fuel is the disintegration of liquid by the process of atomisation. Homogeneous mixing involves the rate of production of fine atomisation of fuel to prevent single droplet combustion and spatial distribution of the fuel spray within the combustor [28]. Ignitability and flame stability are dependent on the drop size distribution and air-spray mixture close to the atomiser. The mixing of spray and surrounding air depends on the size distribution of the spray produced by the atomiser, the flow field created by the atomiser and the fluid dynamic properties of the fuel and air mixture. Therefore, the design of the atomiser and the nature of the atomisation play a key role in the efficient burning of fuel and the overall design of a gas turbine combustor.

The design of the atomiser is primarily dependent on the practical application and on the type of energy used for atomisation [48]. Accordingly there are two main classifications:

a) Pressure atomisers that use pressure head of the liquid for atomisation. Depending on the application there are further classifications based on the design: as plain orifice atomisers, pressure-swirl atomisers, square atomisers, duplex atomisers, dual orifice atomisers, spill return atomisers, fan spray atomisers.

b) Pneumatic atomisers that use the kinetic energy of air for atomisation. Again, depending on the application and design there are further classifications like twin-fluid atomisers, air assist atomisers, airblast atomisers, etc. Apart from the two main classifications of atomisers, there are other types of atomisers like rotary atomisers, electrostatic atomisers, ultrasonic atomisers, and effervescent atomisers etc., which use different forms of energy to achieve atomisation. The air assist and airblast atomisers are similar except that air assist atomisers use large pressure drop of air and low mass flow rates of air to achieve atomisation whereas airblast atomisers use low pressure drop of air and high mass flow rates of air to achieve atomisation.

The current gas turbine combustors employ airblast atomisers as the primary atomizing devices for low pollution concepts and are the present topic of interest. The principle advantage of airblast atomisers is their ability to produce a fine spray and quick mixing in the early stages, especially for combustion systems operating at high pressure. Also, they ensure thorough mixing of fuel and air and are characterised by comparatively low soot formation and high potential to reduce emissions.

At present two prominent types of airblast atomisers are used in aero-engine combustors. Figure 1.1 shows typical designs of nonprefilming and prefilming atomisers. In nonprefilming airblast atomisers, atomisation is achieved by spreading the fuel into a thin annular sheet and exposing it to the shearing action of high velocity co-flowing air streams on both sides. In prefilming airblast atomisers, usually fuel from a pressure swirl atomiser forms a hollow cone spray. The spray impinges on a swirler cup forming a thin annular liquid film or sheet that is transported by the inner flow to the atomiser lip. Swirled air streams on both sides of the swirler cup induce high shear rates in the liquid film causing atomisation. Though both concepts are similar, the interaction of the inner air stream with the liquid film leads to different film properties at the atomiser lip for the case of the prefilming airblast atomisers. However the relative merits of one concept over the other with respect to atomisation are not fully known.

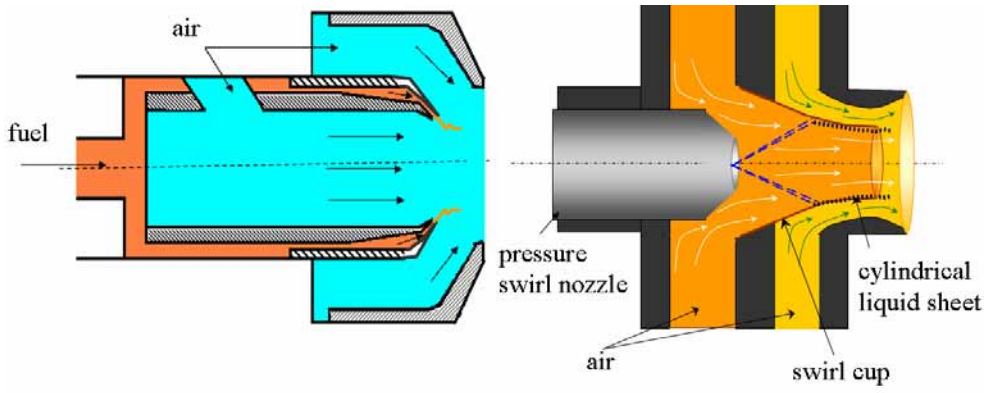

Fig. 1-1 Nonprefilming and prefilming airblast atomisers

Hence the study of atomisation of the liquid sheet is sought for both types of airblast atomisers. This is the objective of the present investigation. Moreover the effect of high pressure conditions on the liquid sheet breakup has to be understood for accessing the practical advantages of both concepts. Several research groups worked on different aspects of atomisation, atomiser development and basic studies on liquid sheet breakup. The following sections discuss the previous works that are pertinent for the present study.

1.2 LITERATURE SURVEY

The atomiser design is considered effective if maximum specific surface area of the fuel is achieved that increases mixing and evapouration of fuel. The increase in specific area and mixing of the fuel is one important prerequisite for efficient combustion, a wider operating range and lower emissions. The liquid fuel is usually discharged through the atomiser in the form of a liquid jet or a liquid sheet. Hence, it is necessary to understand the breakup of liquid jets, sheets, secondary breakup of droplets, and the fluid dynamics involved in liquid-air interaction for efficient design of atomisers. New developments are made in the measurement methodologies in two-phase flows for quantification of mean droplet sizes and measurement of parameters that govern the complex two-phase flow physics.

The following sections give a brief overview of the past literature with a specific interest to liquid sheet break-up and the advanced optical measurement techniques adopted in the present research.

1.2.1 Breakup of Liquid Jets and Sheets

(A) Breakup of Liquid Jets

Research groups studied experimentally and theoretically the atomisation of liquid jets. The focus was on the interaction of the forces driving the process of breakup of liquid jets- inertial forces, surface tension forces, aerodynamic forces, viscous forces- that act on or in liquid jets and parameters that govern these forces. The breakup of liquid jets is widely considered as generic atomisation process. Hence, it is necessary to have an overview of studies on liquid jets, even though the present research program deals with the breakup of liquid sheets.

The first simplified theoretical model, which is generally accepted for the breakup of liquid jets, was developed by Rayleigh [66]. Rayleigh considered the method of propagation of small disturbances to predict the critical conditions under which a *non-viscous laminar liquid jet* breaks up in a quiescent environment under the action of gravitational and surface tension forces. It was concluded that the small disturbances on

the surface of the liquid jet grow exponentially when the wavelength of the disturbance is equal to the circumference of the liquid jet. This type of breakup mechanism is called Rayleigh breakup. The average drop size obtained after the breakup is given by D=1.89d, where D is the diameter of the droplet and d is the diameter of the liquid jet. The theory was proved experimentally by Tyler [83].

Weber [86] theoretically considered the effect of *viscosity of the liquid jet*, *aerodynamic forces and the drag* on droplet formation. He found that the relative velocity between the liquid jet and the surrounding air reduces the wavelength at which the jet breakup occurs. Supporting Weber's theoretical model, Haenlein's [31] experimental results identified four regimes of liquid jet breakup, as shown in Figure 1.2 These are, a) formation of drops without influence of air, termed as Rayleigh Breakup as explained earlier, b) formation of drops under the influence of air, existence of symmetric dilational waves on the liquid jet, c) formation of drops due to waviness of the jet, where sinuous waves are formed on the liquid jet, d) complete disintegration on liquid jet.

Further experimental measurements were carried out in high velocity regimes of surrounding air and liquid jet. Ohnesorge [58] based on visualisation measurements correlated the disintegration mechanisms of liquid jets of various diameters with the non-dimensionless Ohnesorge number and Reynolds number of liquid jets. Further studies were carried out by Sleicher [79], Schweitzer [75] on the effect of *velocity profile and turbulence* of liquid jets on atomisation. Efforts were also taken to measure the breakup length as a function of jet velocity. Sterling and Sleicher [81] developed a theoretical model by modifying Weber's model on liquid jet breakup length. Eroglu and Chigier [24] experimentally measured the intact lengths of liquid jets over a jet Reynolds number range of 18000 and Weber number range of 260.

Under the conditions prevalent in Gas turbine combustion, the liquid jet is

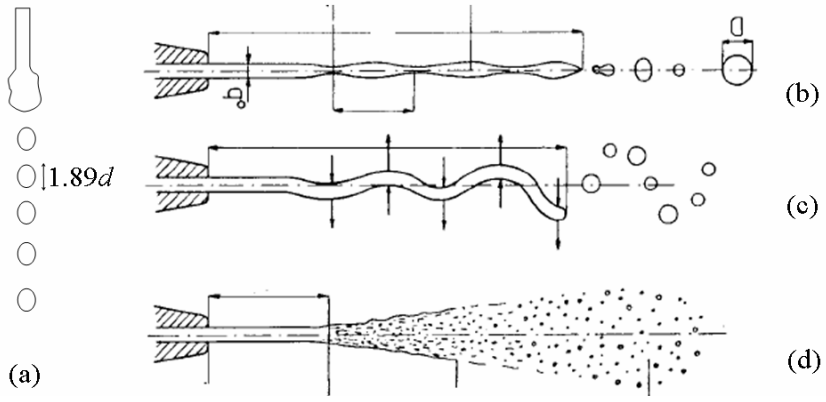

Fig. 1-2 Breakup regimes of liquid jet

injected into a crossflow. The disintegration occurs mainly due to two mechanisms. These are termed as Surface breakup mechanism, characterised by the gradual erosion of Jet as droplets are stripped off from the surface of the liquid jet by the shearing action of the crossflow [63] and Column Breakup mechanism, which is initiated by the growth of waves on the surface of the jet and possibly also on instabilities within the jet. The surface breakup of jets bears some analogy to the behaviour of liquid sheet disintegration at elevated pressure and velocity conditions.

(B) Breakup of Liquid Sheets

Though from the study of breakup of liquid jets one can fairly well understand the general atomisation mechanism of liquids, most of the practical atomisers in gas turbine applications produce cylindrical or conical liquid sheets. The present research program focuses on the breakup of liquid sheets in nonprefilming and prefilming atomisers. Hence understanding of liquid sheet breakup in such applications is more crucial.

Theoretical Investigations of Liquid Sheet Breakup

York et al. [89] studied theoretically the disintegration of *planar non-viscous liquid sheets* of finite thickness. Instability and wave formation at the interface of liquid and air is considered to be the major factor for the breakup of liquid sheet into drops. The force balance between the surface tension and aerodynamic forces is used as the stability criterion for the wave. Hagerty and Shea [32] reduced the analytical difficulties in York's analytical treatment of liquid surface as 'hyperboloid of revolution'. They extended the analytical work to *flat non-viscous liquid sheets* by a slender orifice, which may be subjected to waves of any desired frequency. *They concluded that only two types of waves are possible on the surface of a liquid sheet.* Each of the surfaces of the liquid sheet can be in-phase to produce sinuous waves or they can be out-of-phase to produce dilational waves. Both waves are unstable over the same range of frequencies.

The equation for stable frequencies is given by

$$f_c = \frac{\rho V^3}{2\pi\sigma} \qquad \text{Eq. 1-1}$$

where f_c is the frequency, ρ is the density of air, V is the velocity of air, σ is the surface tension of liquid.

They have also predicted the growth rate factors for both sinusoidal and dilational waves. The growth rate factor for sinusoidal and dilational waves is given by

$$\beta_s = \left(\frac{n^2 V^3 \rho - n^3 \sigma}{\tanh na} \right)^{0.5} \quad \frac{\beta_s}{\beta_d} = \coth na \qquad \text{Eq. 1-2}$$

where β is the growth factor, n is wave number of disturbance, ρ is density ratio, a is half-width of liquid sheet. The growth rate of sinuous waves is always greater than that of dilational waves.

Lin [50] showed that in the absence of ambient gas, the viscous liquid sheet is asymptotically stable with respect to temporally or spatially growing disturbances when the Weber number is smaller than one half. However most of the theoretical works cited above don't take into account the aerodynamics and viscous effects of the surrounding air on the liquid sheet breakup.

Taylor [83] showed in his study that interfacial wavelength decreases by orders of magnitude when the *viscosity of the surrounding air is neglected*. Rangel and Sirignano [64, 65] have investigated both theoretically and computationally using vortex discretion theory, the instabilities of a finite thickness liquid sheet by considering the *effect of surface tension and density difference* between the two fluids (liquid sheet and surrounding fluid). It was concluded that the density ratio between the fluids effect the growth rates of sinuous and dilational waves. In sinuous modes the ligament spacing is equal to half of the wavelength whereas in dilational modes the ligaments spacing is equal to one wavelength. Mehring and Sirignano [55] have further extended the theory to annular sheets. Efforts are also under way to improve the mathematical modeling to high velocity regimes. Senecal et al. [77] have developed a linear stability model to predict the wave growth in high speed regimes. Dombrowski and Johns [18] have tackled analytically more realistic case where the fluid viscosity is considered and the thickness of the liquid sheet diminishes as it moves away from the orifice.

Experimental Investigations of Liquid Sheet Breakup

Dombrowski and Fraser [19] have reported initial photographic investigations on the breakup of conical liquid sheet emerging from pressure swirl nozzle and fan spray nozzles. The co-flowing air streams interact with the liquid sheet at the exit of the nozzle. They concluded that the fundamental principle of disintegration of liquid is the increase of the surface area of a liquid sheet or jet until it becomes unstable and disintegrates. *Even though several disintegration modes can be described for a liquid sheet, the final phase of the breakup mechanism is always the breakup of the liquid thread or jet*. Three modes of sheet disintegration are described viz. rim, wavy and perforated disintegration, Figure 1.3. In rim disintegration, the edges of the liquid sheet form into thick edges due to surface tension forces and break up as liquid jets. In wavy disintegration, the major wave disturbances in the surrounding air causes sheet

disintegration. In perforated-sheet disintegration, point disturbances on the liquid sheet puncture the liquid sheet at regions where the liquid sheet is very thin. The holes expand resulting in rim like structures which break similar to liquid jets. Dombrowski and Fraser investigated the *effect of turbulence* in the liquid. They have observed that the effect of turbulence is significant. The parametric *analysis on density, viscosity and surface tension of liquids* showed that the effect of density is negligible. The viscosity and surface tension have a similar effect which is to improve the stability of the liquid sheet.

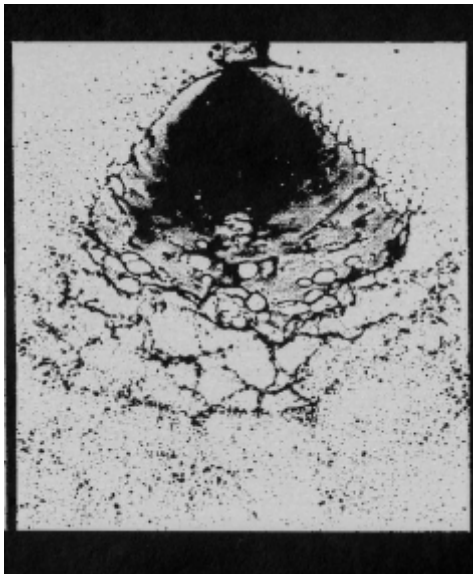

Fig. 1-3 Typical breakup of liquid sheet from single hole nozzle

Crapper et al. [15, 16] perturbed the fan-shaped sheets by vibrating the nozzle at fixed frequencies. They found that the wave growth depends on the sheet velocity and distance from the nozzle. *The photographic evidence showed the formation and movement of vortices in the surrounding air indicating an influence of vortices on the breakup of liquid sheet.* Fig. 1-4 shows the vortex growth at the surfaces of the liquid sheet. They have also developed methods to measure the growth rates of low amplitude waves at any distance from the nozzle.

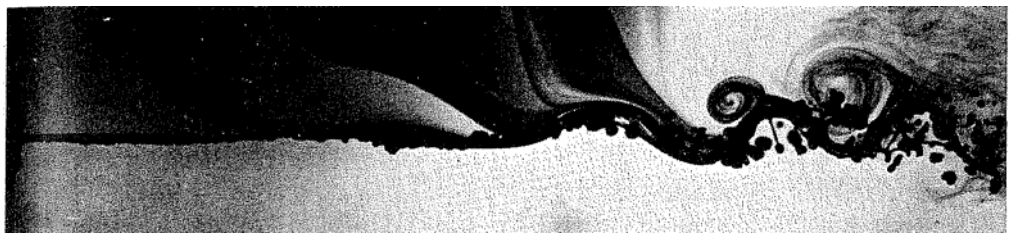

Fig. 1-4 Vortex growth on the surface of the liquid sheet.

Mansour and Chigier [53] experimentally studied the aerodynamic instabilities of liquid sheets in air-assist atomisers. Detailed measurements of frequencies of oscillations of liquid sheet were performed. Similar modes of breakup as from earlier researchers are observed. It was concluded that introducing air in the nozzle is similar to forced vibrations induced on the nozzle. As the frequency of the force vibrations approach that of natural frequency of the nozzle, resonance is established. At resonance, the maximum spray angle is achieved.

Stapper et al. [80] studied the *role of air and liquid velocities* on the formation, size and lifetime of ligaments. They observed two breakup mechanisms termed as cellular breakup and stretched streamwise ligament breakup. Figure 1.5, shows the schematic of the breakup mechanisms.

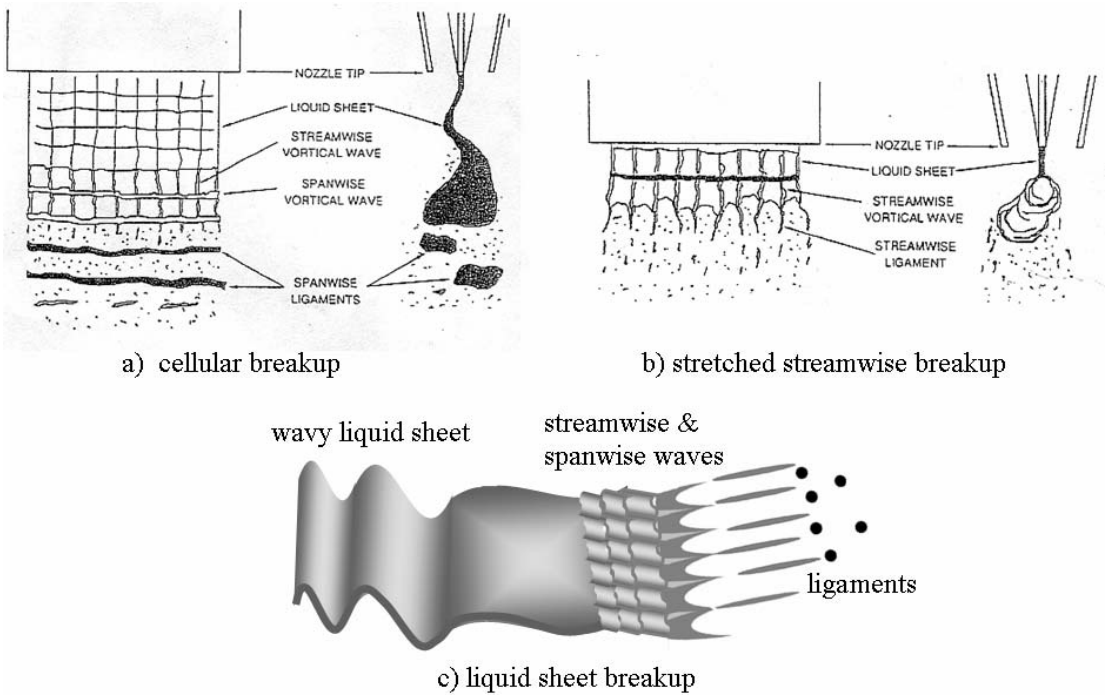

Fig. 1-5 Breakup regimes of liquid sheet (Stapper et al., 1992)

Cellular breakup occurs when the relative air velocity to liquid is high. The spanwise vertical waves that propagate across the direction of flow have equal strength to the streamwise vertical waves that propagate along the direction of flow. The studies revealed that the ratio of liquid/air velocity is a key factor for ligament formation and breakup. The stretched streamwise ligament breakup occurs at low liquid velocities. The streamwise vertical waves are dominant in the breakup process. The liquid sheet is stretched by the co-flowing air streams causing the membranes between the streamwise waves to burst. The streamwise ligaments break subsequently similar to liquid jet breakup.

Berthoumieu et al. [7, 8] studied both experimentally and computationally the behaviour of a planar liquid sheet with an aspect ratio of 60 and compared it with the annular liquid sheet. The initial curvature of the annular liquid sheet gives it a higher rigidity resulting in lower oscillation frequencies. The ligament spacing is smaller in case of the annular liquid sheet.

Some works are reported on breakup mechanisms at high pressure and high velocity surrounding air, which is a more realistic situation. The liquid sheet disintegration research at high velocities of air, typical for airblast atomisers as in the present topic of interest, was further studied by Arai and Hashimoto [2], and Rizk and Lefebvre [67]. However, the focus was on final drop size distribution and effect of nozzle geometry on fuel placement. Berthoumieu [9] has carried out visualisation experiments on liquid sheets emanating from a nonprefilming atomiser by varying the liquid surface tension, pressure and velocity of air at constant momentum flux ratio of air. It was found that the liquid breakup mechanism depends on the static pressure of air at constant momentum flux. This issue is addressed in the present experimental study.

The research works discussed above are on the liquid sheet between two coflowing air streams. In the present research program, a prefilming atomiser is used where there is interaction of only one air stream with the liquid sheet until a certain distance after which both air streams interact as explained in the beginning of this chapter. This could have a significant effect in on the breakup process in particular in high speed flow situations. There are not many research groups working on basic studies of breakup of liquid sheet on a prefilming surface. Berthoumieu et al. [7] studied the breakup of liquid sheet on a prefilming surface. Their research work was focused on estimating the frequencies of the liquid sheet before disintegration. They have related the ligament spacing with frequencies and considered the effect of thickness of the liquid sheet and velocity of liquid and air. Yule et al. [90, 91] have also carried out similar work on liquid sheet breakup. A flat sheet was produced by impinging of a liquid jet on a flat plate similar to the present study. They found that the gas velocity influences primary breakup and velocity ratio between air and liquid can have influence on primary breakup. Table 1.1 shows the operating ranges studied by research groups on liquid sheets.

As stated above there is no pertinent literature available on the breakup of liquid sheets on the prefilming surface at realistic operating conditions (high velocities and pressures of surrounding air). During the study of liquid sheet breakup in the present research program, further literature survey is needed to understand the propagation of waves on liquid surface. Usually, the small amplitude waves on the liquid surface are considered to be capillary waves. Capillary waves are formed due to surface tension forces. Surface tension forces are most effective at short scales, about one centimeter or

less, in the present case. Thus surface tension forces act as a restoring force; crests try to become lower and troughs higher. The propagation of such waves is explained by Einstein [22] by considering the force balance between the static and dynamic pressures that arise between two points of different elevation on the surface. The Einstein work on wave propagation is extendable to the gravity waves formed in the ocean. Gravity waves when they approach sea shore form shallow waves. Shallow waves are formed due to the action of gravity. Gravity acts like a restoring force. The similarity of propagation of these waves is explained by Kenyon [44, 45]. A similar behaviour of waves formed on the surface of the liquid sheet on the prefilming surface and propagation of waves was observed by Umesh et al. [84, 85]. This is explained in Chapter 3 in a more detailed manner in the discussion on breakup mechanism of liquid sheet on prefilming surface.

Investigators	*Thickness of liquid film (mm)*	*Velocity of liquid (m/s)*	*Velocity of air (m/s)*	*Pressure of air (bar)*
Rizk&Lefebvre [67]	0.089-0.4	1-5	55-120	atmospheric
Mansour et al. [53]	0.254-1.45	1-16	0-145	atmospheric
Stapper et al. [80]	0.508	1-5	0-60	atmospheric
Lozano et al. [51]	0.95	0.2-2.45	8-65	atmospheric
Berthoumeiu♦ [9]	0.3	0.5-2	60-90	1.65-15
Yule et. al. ♦ [91]	2.5	1.5-3	10-20	atmospheric
Present Study	0.3	0.2-2	30-90	1.7-6

Table 1-1 Operating ranges studied by research groups on liquid sheets

Drop Size Correlations for Airblast Atomisers

As explained in the previous sections, there is still a lack of experimental knowledge on spray formation from liquid sheets. A few research groups obtained correlations for the drop size from the airblast atomisers. Parametric analysis has to be performed experimentally to obtain empirical correlations between mean drop sizes and operating conditions for specific atomiser designs. This is essential from the engineering point of view for the design of effective atomisers. Lefebvre [47] developed airblast atomisers in which the angle of impingement of air on the liquid sheet is either parallel or impinges at an appreciable angle. It was found that if the impingement angle is high, it will restrict the formation of waves on the liquid sheet. The liquid sheet

♦the study was on prefilming type atomiser

breaks instantaneously, termed as prompt atomisation. The prompt atomisation is characterised by a broad range of drop sizes in the spray and a lack of sensitivity of mean drop size to variation of viscosity, atomizing air pressure and initial thickness of the spray. An equation is derived for mean drop size based on the assumption that the controlling process of prompt atomisation is the ratio of energy required for atomisation to the kinetic energy of air. The equation is given as

$$SMD = 3.\left[\frac{1}{t} + \frac{0.007\rho_L U_A^2}{4\sigma(1+\frac{1}{AFR})}\right]^{-1} \qquad \text{Eq. 1-3}$$

where *SMD* is the mean diameter based on volume-to-surface ratio of droplets, t is the thickness of the liquid sheet, U_a is the velocity of air, *AFR* is air-to-fuel ratio. For plain-jet type of airblast atomisers SMD is given by

$$SMD = 3.\left[\frac{2}{d_o} + \frac{C^*\rho_L U_A^2}{4\sigma(1+\frac{1}{AFR})}\right]^{-1} \qquad \text{Eq. 1-4}$$

where d_o is the initial diameter of the liquid jet, C^* is efficiency of atomisation.

Jasuja [41] has given detailed developments in formulating correlations by various research groups for plain jet and prefilming airblast atomisers as shown in Figure 1.6. The focus was on recognising the key parameters of air and the liquid. Accordingly, correlations were developed for SMD of the spray. The correlations contain two key components, the first term dominated by properties of air and second term by viscosity of liquid.

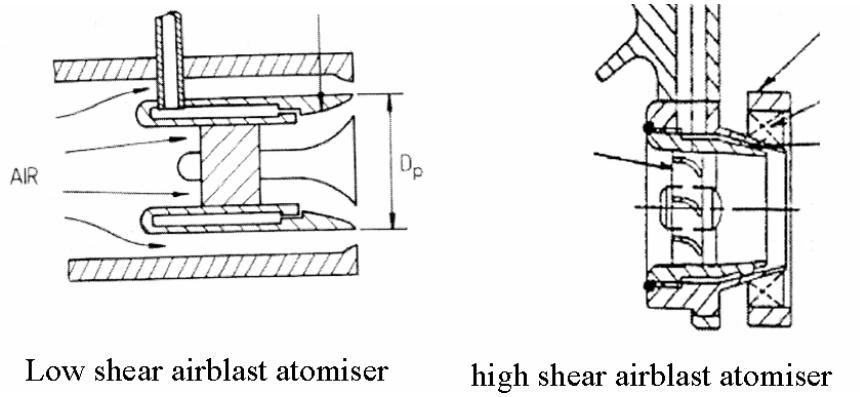

Fig. 1-6 Typical prefilming airblast atomisers

For prefilming airblast atomisers, SMD is proportional to

$$\frac{SMD}{l_c} \propto \left(\frac{\sigma}{\rho_{\acute{a}} u_a^2 l_c} \right)^{0.5} \left(1 + \frac{1}{AFR} \right) \qquad \text{Eq. 1-5}$$

where l_c is the characteristic length of the prefilming surface.

However, there are several factors that have to be taken into consideration in using these correlations. One has to take into account the geometric similarity of atomisers in arriving at these correlations and also the operational regimes under which these correlations are valid. Brandt [12] has provided a correlation for a prefilming airblast atomiser similar to the atomiser used in the present research program. It is given by

$$SMD \propto b_k^{0.3} . \frac{\sigma_k^{0.5}}{\rho_a^{0.3} u_a} \qquad \text{Eq. 1-6}$$

where SMD is the Sauter mean diameter (μm), b_k is the liquid loading (kg/s/m), σ_k is the surface tension of kerosene (N/m), ρ_a is the density of air (kg/m³), u_a is the relative velocity between liquid sheet and air (m/s). The liquid loading is calculated as $\rho_l . V_l . t_l$, where t_l is the thickness of the liquid sheet (μm). Table 1.2 shows the operating conditions at which prefilming atomisers are studied by research groups and the power dependency of the parameters they obtained.

1.2.2 Spray Dispersion

Secondary Atomisation of Droplets

The breakup of the liquid jet or sheet into ligaments and further into large droplets is usually termed primary breakup. The research work cited above primarily deals with the primary breakup and the correlations obtained are for the final drop size. In realistic cases, the most essential information is the final droplet size. The large droplets which are formed during primary breakup may further break into smaller droplets depending on the aerodynamic forces, surface tension and viscous forces acting on large droplets. This is termed secondary atomisation. The information on secondary atomisation and the dispersion of the spray is necessary for understanding the fuel placement and mixing of spray in the combustor. For low viscosity, the droplet breakup is primarily controlled by aerodynamic forces and surface tension forces. The effect of these forces can be represented by the non-dimensional Weber number given by

$$We_p = \frac{\rho_a u_{rel}^2 D_o}{\sigma} \qquad \text{Eq. 1-7}$$

where u_{rel} is the relative velocity between air and liquid. The critical Weber number for breakup of a drop in constant velocity air stream is 22, Heinze [37]. For liquid droplets suddenly exposed to high velocity air stream, the critical Weber number is 13.

	Operating conditions				*Power dependency*			
Investigators	Liquid	(P_a) (bar)	(U_l) (m/s)	(U_a) (m/s)	(U_a)	(ρ_a)	(ρ_l)	(σ)
Brandt et al. [12]	Jet A1 Fuel	3-14.5	1-2	120	-1	-0.3	0.3	0.5
Rizkalla & Lefebvre [68]	-	0.1 - 0.85	-	70-125	-1.0	-1.0	0.5	0.5
Jasuja [40]	Residual oil	0.1-0.86	-	55-135	-1.0	-1.0	0.5	0.5
El-Shanawany & Lefebvre [23]	Water, Kerosene	0.1-0.85	-	60-190	-1.2	-0.7	0.1	0.6
Lefebvre [49]	-	-	1	-	-1.0	-0.5	0	0.5

Table 1-2 Power dependency on Mean drop size of parameters

For accelerating droplets the deformation and breakup of a droplet is represented by the non-dimensional Bond number given by

$$Bo = \frac{D^2 a \rho_l}{\sigma} \qquad \text{Eq. 1-8}$$

where ρ_l is the density of liquid and a is the acceleration of the droplet, It is given by (Blümcke et al. [10])

$$a = \frac{du_p}{dt} = \frac{3}{4}\frac{\rho_a}{\rho_p}\frac{\nu_a C_D \,\mathrm{Re}_p}{D^2} U_{rel} \qquad \text{Eq. 1-9}$$

$$C_D = \frac{24}{\mathrm{Re}_p}(1+\frac{1}{6}\mathrm{Re}_p^{2/3}) \qquad \text{Eq. 1-10}$$

where C_D is the drag coefficient droplet, Re_p is the Reynolds number of the droplet, u_p is the velocity of droplet, ν_a is the kinematic viscosity of air and D is the diameter of droplet. If the Bond number is greater than 0.6 then it implies the deformation of spherical droplets into an ellipsoidal droplet with an aspect ratio of greater than 10%. The knowledge of the Bond number plays an important role as it gives an indication of measurement locations of the PDA Measurements in the spray.

Turbulent Particle Dispersion and Mixing

Apart from understanding breakup mechanisms of liquid jets/sheets and droplets, it is essential to understand the dispersion of droplets in the turbulent gas phase if one has to estimate the mass flux distribution of a spray both spatially and temporally in a gas turbine combustor. The key issue is the interaction of the particles with the turbulence in the flow and the particle response to the turbulent fluctuations. Usually the turbulence in a fluid flow is represented by Reynolds decomposition of the instantaneous velocity of the flow. The instantaneous velocity is represented as

$$\overline{u}_i = U_i + u_i \qquad \text{Eq. 1-11}$$

where is U_i time average component of velocity over a period of time and u_i is fluctuating component of instantaneous velocity also called turbulent fluctuations. Over a time domain the turbulent fluctuations are represented by the root mean square of turbulent fluctuations, u_{rms}, also called turbulent strength. It is given by

$$u_{rms} = \sqrt{\sum\left(u^2\right)} \qquad \text{Eq. 1-12}$$

A key parameter characterising the particle dispersion behaviour in a turbulent fluctuating flow is the Stokes number, St, defined as the ratio of aerodynamic response time of the particle τ_{rex} (particle relaxation time) to the characteristic time scale of turbulence, τ.

It is given by

$$St = \frac{\tau_{rex}}{\tau} \qquad \text{Eq. 1-13}$$

It gives a measure of the degree to which a droplet follows the flow sincerely considering its inertial properties versus changing flow conditions. Bigger droplets tend

to have stronger inertial effects and follow the flow rarely where as smaller droplets tend to follow the flow. Below Stokes number < 0.1 indicates that droplets follow the flow more precisely. Stokes number > 10 indicates that droplets have their own trajectory governed by their inertial forces. Even though the ability of the droplet to follow the flow depends on the droplet size, it also depends on the response of the droplet to the characteristic length scales of eddies in a usually turbulent flow. Depending on the droplet size class and the eddy length scale, selective dispersion effects can exist. These are normally represented by particle/droplet relaxation time, i.e., the time taken by a droplet to reduce the relative velocity with air by a factor of 37%, and characteristic time of the mean flow field, i.e., spatial variation of gas velocity. The characteristic time of large eddies is normally considered as the time scale of turbulence. The particle relaxation time is based on the aerodynamic forces acting on the particle and the time taken by the particle to decelerate by 1/e times its initial velocity. It is given by

$$\frac{du}{dt} = -\frac{u}{\tau_{rex}} \qquad \text{Eq. 1-14}$$

Experimental and numerical investigations on particle dispersion in turbulent flows are reported by Synder and Lumley [82], Lazaro and Lasheras [46], Hassa et al. [33], Aggarwal et al. [1]. The forces acting on the particle are estimated and calculated. Several equations are given for estimating the drag on the particle in different regimes of the flow. Typically for small Particle Reynolds numbers Re_p<1, the force acting on the particle is given by $F = 3\pi\mu_a u_r D_p$

and for Particle Reynolds numbers, 1000< Re_p<200000, it is given by

$$F = C_D \frac{\pi D_p^2}{8} \rho_a u_{rel}^2 \qquad \text{Eq. 1-15}$$

For Re_p < 1, the particle relaxation time is given by

$$\tau_{rel} = \frac{1}{18} \frac{\rho_p}{\mu_a} D_p^2 \qquad \text{Eq. 1-16}$$

where μ_a is the dynamic viscosity of air.

Spray Characterisation

The spray from the atomisation process is usually chaotic and results in a wide spectrum of droplet sizes. Due to the lack of measurement techniques, that can accurately measure droplet size distributions and also for condensing the data, the

droplet size distributions are expressed more analytically by statistical and empirical equations as a function of operating parameters. It is also essential to represent the droplet size distribution in a concise mathematical expression if one has to model the transport phenomena of mass and heat transfer in a two phase dispersed flow system.

One of the initial research groups that worked on representing the particle size distribution in mathematical form is Rosin and Rammler [69]. They represented the particle size distribution data obtained from pulverisation of coal in a mathematical form

$$1 - Q = \exp -(D / X)^q \qquad \text{Eq. 1-17}$$

where Q is the fraction of the total volume contained in drops of diameter less than D, X and q are constants. The advantage of this mathematical form is that one can represent the drop size distribution with just two parameters X and q. The constant q measures the spread of drop sizes. A higher value of q implies that the spray is more uniform. Its value usually lies in the range of 1.5 to 4. X is a representative diameter of some kind. Usually X is the drop diameter such that 63.2% of the liquid volume lies in the drops of smaller diameter.

The Rosin and Rammler equation is a generic power law equation representing the size distribution. Mugele and Evans [57] after analysing various functions of representing the spray distributions have come up with an upper limit mathematical function. The function represents the volume distribution equation and is given by

$$\frac{dQ}{dy} = \delta \exp \frac{-\delta^2 y^2}{\sqrt{\pi}} \qquad where \qquad y = \ln \frac{aD}{D_m - D} \qquad \text{Eq. 1-18}$$

As y goes from – 8 to + 8, D goes from D_o to D_m. δ is related to the standard deviation of y. D_o and D_m are the minimum and maximum droplet size.

Though the mathematical size distribution functions bring the mathematical simplicity and ease in the usage in computations, it is sometimes more convenient to work with mean and weighted diameters for a distribution in engineering applications. The commonly used mean diameters are

$$D_{10} = \frac{\int_{D_0}^{D_m} D(dN/dD)dD}{\int_{D_0}^{D_m} (dN/dD)dD} \qquad \text{Eq. 1-19}$$

for comparison of distributions,

$$D_{20} = \left[\frac{\int_{D_0}^{D_m} D^2 (dN/dD) dD}{\int_{D_0}^{D_m} (dN/dD) dD} \right]^{\frac{1}{2}} \quad \text{Eq. 1-20}$$

for processes where surface area is a controlling factor,

$$D_{30} = \left[\frac{\int_{D_0}^{D_m} D^3 (dN/dD) dD}{\int_{D_0}^{D_m} (dN/dD) dD} \right]^{\frac{1}{3}} \quad \text{Eq. 1-21}$$

for processes where volume is a controlling factor.

Sauter Mean Diameter (SMD) is used for applications related to gas turbines where it involves mass transfer, evaporation and combustion. SMD is given by

$$D_{32}(SMD) = \frac{D_{30}}{D_{20}} \quad \text{Eq. 1-22}$$

SMD is the diameter of the drop whose ratio of volume of drop to surface area is same for the entire spray. It is a crucial parameter for mass transfer and combustion related applications. Also of significance for combustion are $D_{0.1}$ where 10% of the total volume is in smaller droplets, $D_{0.9}$ where 90% of the total liquid volume is in drops of smaller droplets, and $D_{0.5}$ also called mass mean diameter, where 50% of the total liquid volume is in drops of smaller droplets. The locations of characteristic diameters on a size distribution curve can be seen in Figure 1.7.

Another parameter that is used to represent the spray is dispersion. The dispersion indicates the range of droplets in a distribution. It can be represented by parameters like droplet uniformity index, dispersion index, dispersion boundary factor. The most commonly used is relative span factor, defined by

$$\Delta = \frac{D_{0.9} - D_{0.1}}{D_{0.5}} \quad \text{Eq. 1-23}$$

where $D_{0.9}$ is 90% volume undersize diameter, $D_{0.1}$ is the 10% volume undersize diameter and $D_{0.5}$ is 50% volume undersize diameter. The relative span factor gives a direct indication of the range of drop sizes relative to mass mean diameter.

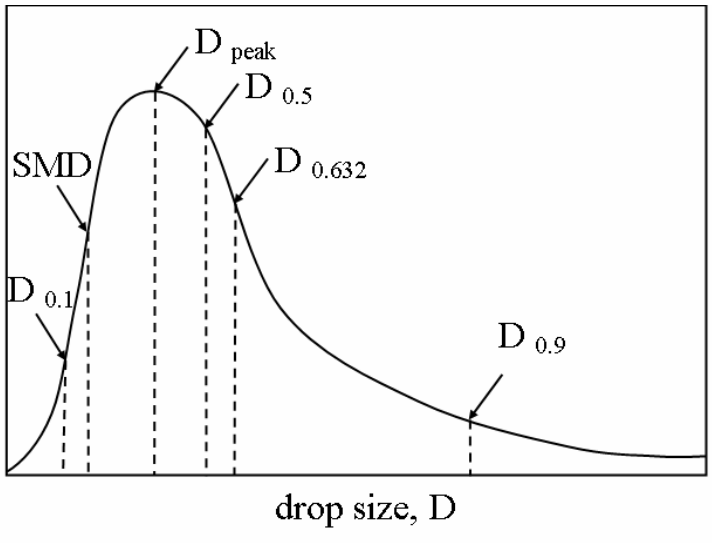

Fig. 1-7 Size distribution curve

1.2.3 Nonintrusive Measurement Techniques

The present study adopts an experimental approach towards quantifying the parameters that govern the atomisation. Hence, it is essential to refer to developments in measurement techniques in two-phase flows particularly for applications in gas turbine combustors.

The significant information that is required in characterising the spray from the point of view of combustor development is the fluid dynamic aspects of the spray and air. Parameters like size distribution of the droplets, velocity, evaporation rates, density, temperature, mass flux distribution of the droplets, local velocity, temperature, density of air are essential for understanding and modeling of the two-phase flow interaction. Several novel non-intrusive techniques like LDA, PDA, 3C-LIF-PDA, Rainbow refractometry, IR absorption, PIV etc, have been developed over the past decades to measure these parameters under realistic conditions. However, the critical challenges still exist for measurements in two phase flows.

Background shadowgraphy has been adopted for qualitative analysis of atomisation and breakup mechanisms in liquid jets and sheets. Presently, the images acquired either with background shadowgraphy or by laser sheet illumination are providing quantitative information of size and velocity field of the spray. The emerging technique PIV has been receiving attention to provide velocity information in the near-field of the atomiser where other non-intrusive measurement techniques like PDA cannot measure accurately. Research works have been reported recently applying PIV to measure velocity fields of both the air and the fuel phase simultaneously. Driscall et al. [20] have used two double pulse lasers with different wavelengths and two double-

frame cameras to image simultaneously the injected fuel and entrained air to determine the 2D velocity vector fields of both phases using cross-correlation PIV. The use of two different wavelengths of lasers allows spectral separation of signals.

PDA (Phase Doppler Anemometry) is the most sophisticated instrument used in spray analysis in the current research on two phase flows and used in the current research program. It is described by Flögel [27] relating the phase difference between the Doppler signal from two detectors as the particle passes through a fringe space to the particle diameter. The details of the working principle are given in chapter 2. The main challenges in using a PDA system are to access the core of the spray, measure high velocity fluctuations and measure small particles. This requires a small probe volume, high laser power and advanced signal processing [3]. As of today, still several developments are underway to use PDA in dense sprays to measure the liquid mass flux which is a crucial factor for determining the evaporation rates of the spray [73]. The measurement of mass flux depends mainly on measuring the size of the measurement volume accurately. Saffman et al. [72] proposed an algorithm for measuring mass flux by computing the cross-section of the particles for a one dimensional flow. The mean burst length for each particle size class is used to determine the diameter of the measurement volume and therefore the particle cross-section. Brandt [11] proposed an extension of Saffman mass flux algorithm to two dimensional flows, to measure mass flux in any direction and a correction algorithm that considers the effect of the slit in the receiving optics on the effective size of the measurement volume. Figure 1.8 shows the cross section of the measurement volume. The effective measurement volume seen by the receiving optics is the area of $(L1+L2).D_e$. The true burst lengths are limited in the regions due to the slit effect and the true burst length is proportional to slit width and the scattering angle. If the effect of slit is not considered as in the algorithm by Saffman, the measured burst lengths are smaller. This gives smaller measurement volume cross-section and higher mass fluxes. This is corrected in the algorithm by the following correction.

$$Burstlength(true) = Burstlength(measured).\frac{\frac{D_e^2}{\tan(\varphi)} + \frac{s}{\sin(\varphi)}}{\frac{s}{\sin(\varphi)}} \quad \text{Eq. 1-24}$$

where D_e is the Gaussian beam diameter, s is the slit width, φ is the scattering angle. Behrendt and Hassa [5] extended the 2D algorithm of Brandt to three dimensional flows by considering all 3 velocity components. However, in the present experimental campaign, a 2D standard PDA system is used and Brandt's 2D algorithm is used to measure the mass flux.

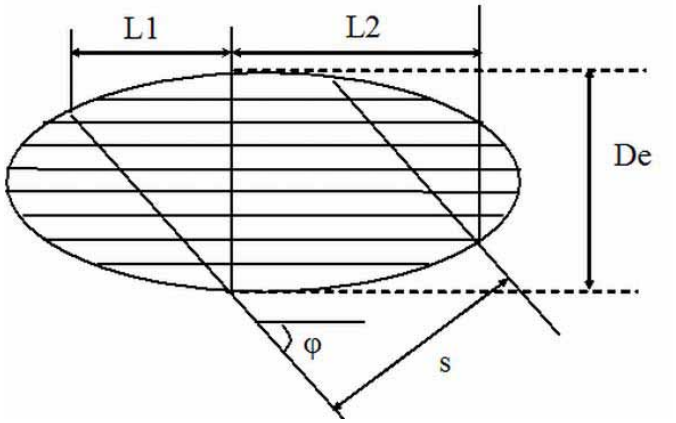

Fig. 1-8 Measurement volume as seen by the receiving optics

1.3 SCOPE OF THE THESIS

As presented in the previous sections, research works both theoretical and experimental exist on the liquid sheet breakup mechanism, some addressing the basic mechanism of liquid sheet breakup sandwiched between two co-flowing air streams, some quantifying the parameters that govern the fuel placement and dispersion of the spray for specific type of atomiser. Most of the investigations are under unrealistic geometrical and operating conditions. A few issues that are not yet addressed are: does the prefilming surface have any effect on the global properties of the spray at various operating conditions? Whether the prefilming airblast atomiser is a better choice or the nonprefilming airblast atomiser under realistic operating conditions of gas turbines? Some fundamental issues that have to be addressed are: what is the effect of air density and prefilming length on the physics of the liquid sheet breakup irrespective of the application of the atomiser, since such an understanding will improve the quality of modeling of two phase flow related problems at realistic operating conditions.

In view of the above needs, the objective of this work is to experimentally characterise the drop size of nonprefilming and prefilming airblast atomisers at elevated pressures. The study of the phenomena of the liquid sheet breakup of the nonprefilming and prefilming atomisers is undertaken to understand whether the breakup mechanism of the liquid sheet has any influence on the final drop size of the atomisers.

In order to meet the above objectives, a nonprefilming and a prefilming airblast atomiser are tested at DLR, in the LPP Test rig under elevated pressure. Flow visualisation experiments are conducted at various operating conditions to study the liquid sheet breakup for prefilming and nonprefilming atomiser. PDA measurements are conducted to characterise the spray for both the atomisers under various operating conditions. Although the present work has been performed to understand the breakup of the liquid sheet for two types of airblast atomisers, the studies have been restricted to

ambient temperature conditions, which is somewhat modest in the context of realistic gas turbine operating conditions. The characterisation of atomisers is performed at the maximum air pressure of 6 bar due to mass flow rate limitations at the test rig at ambient temperature conditions. The effect of change in length of the prefilmer is not studied which could be an important parameter that can govern the atomisation. These conditions are necessary to retain a degree of simplicity in the geometry of the atomiser and understand the effect of other parameters that govern the physics of the phenomena.

1.4 OUTLINE OF THE THESIS

The present chapter highlighted the ongoing research in the field of liquid atomisation related to gas turbine technology, development of measurement techniques in two phase flows and fundamental research on liquid sheet breakup. Chapter II describes the experimental facilities used and measurement techniques adopted in the present study. The results are presented in two chapters. Chapter III describes the results obtained through flow visualisation measurements. Detailed analysis is described on the breakup mechanism of the liquid sheet on the prefilming surface and comparison is made with the classical liquid sheet break-up. PIV is applied to measure the velocity field near to the atomiser. Chapter IV presents the characterisation of the spray for both prefilming and nonprefilming atomisers. Detailed analysis of PDA measurements and comparison of the results between the two atomisers is presented. Chapter V presents the conclusions of the present study on airblast atomisers and outlines the recommendations for future work on this subject.

CHAPTER 2

EXPERIMENTAL SETUP

An experimental approach is adopted in the present study to investigate the liquid sheet breakup mechanism in two types of atomisers' viz. nonprefilming and prefilming atomisers. This chapter presents a description of the test facility and experimental techniques used. The experimental study is broadly classified into two sections:

1. Study of liquid sheet breakup mechanisms in non-prefilming and prefilming atomisers

2. Characterisation of spray of non-prefilming and prefilming atomisers

The study of liquid sheet breakup mechanisms is based on high speed background shadowgraphy. The characterisation of the spray is carried out by LDA and PDA measurements. The experiments are conducted in the LPP (Lean Premixed Pre-vapourised) test facility at DLR, Köln-Porz.

2.1 EXPERIMENTAL TEST FACILITY

The LPP test facility is designed to carry out research on non-reacting two-phase flows at high static pressure and temperature simulating real gas turbine inlet conditions to the combustor. A schematic of the test facility is shown in Figure 2.1. The test facility can be operated at a maximum static pressure of 20 bar and static temperature of 850 K. The central air reservoir at 60 bar provides continuous supply of air. A series of control valves regulate the air pressure to 20 bar to the test facility. The incoming air supply is divided into two lines, viz. the primary and secondary air flow. The air flow rate in these two lines can be further controlled independently by control valves. The primary air flows through a 520 KW electrical heater providing preheated air to the LPP test section. The secondary air is used to cool the test section. At maximum operating conditions given by the current set of valves, the mass flow rate in the test section is 1.3 kg/s. The fuel to the test section is supplied by a 100 liters liquid fuel container. The container is pressurised by nitrogen. Usually, around 40 bar pressure is required in the container to supply the required amount of fuel to the test section.

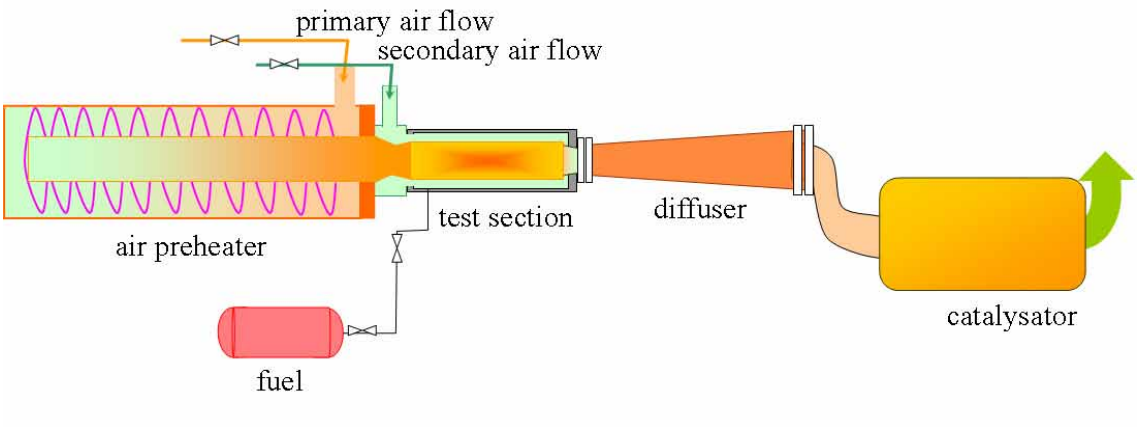

Fig. 2-1 LPP test facility

At high pressures, nitrogen can dissolve in the liquid fuel, hence an inflatable bag is provided inside the container. Nitrogen is supplied to the inflatable bag which pressurises the fuel, hence avoiding direct contact between liquid fuel and nitrogen. In the present study kerosene is used as fuel. Both the air streams along with the unburnt fuel exit through a sonic hole. Due to environmental concerns, the unburnt fuel in the air is decomposed in a catalysator before being released into the atmosphere. Due to the limited capability of catalysator, a maximum fuel mass flow rate of 10 g/s is achievable in the test section.

Test Section

A rectangular test section is designed by taking into consideration the requirements of thermal load and stress at maximum operating conditions of pressure and temperature, mounting various types of atomisers & injectors in the test section, and optical access for non-intrusive measurements. A schematic of the test section is shown in Fig. 2.2.

The frame of the rectangular test section is made up of stainless steel. It has two glass channels providing optical access from three sides to the test section. The primary glass channel is made up of quartz (Herasil make) glass. The length of the quartz channel is 200 mm long, its cross section 40x40 mm and the walls are 5 mm thick. The preheated air enters the quartz channel. The secondary cooling channel surrounding the primary quartz channel is made of thick glass pressure windows on three sides, and the stainless steel test section frame on the bottom side for mounting atomisers and pressure transducers. During high temperature operating conditions, the static pressure in both channels is maintained on a similar level so that the inner quartz channel withstands only temperature gradients while the outer pressure windows withstands pressure gradients. As the primary channel is made of glass, measuring pressure in the primary channel is difficult along the test section. Therefore the pressure in the primary channel

is measured at the inlet and outlet of the channel. The mass flow rates in the test section are measured by vortex meters (Foxboro Inc.) and verified with the flow through a sonic hole. The error in mass flow measurements is ~ 0.5 %.

At the exit of the test section, air from both the channels merges and leaves the test section through a sonic hole. The sonic hole provides the ability to independently vary the pressure in the quartz channel at a constant velocity. Different diameter sonic holes are used to vary the air velocity. The mass flow rate of kerosene is measured by Coriolis meters of Rheonik make. The error in the measurement is < 0.2 %. A circular hole is provided in the quartz channel for mounting atomisers. The atomiser is mounted at 30 mm from the entrance of the test section.

2.2 DESIGN OF THE AIRBLAST ATOMISERS

Airblast atomisers are designed to conduct basic studies on liquid sheet atomisation of prefilming and non-prefilming atomisers. The liquid sheet is mostly of cylindrical shape in practical airblast atomisers as explained in Chapter 1. However, in the experimental studies presented here, the cylindrical liquid sheet is approximated to a 2D planar liquid sheet model, Figure 2.3.

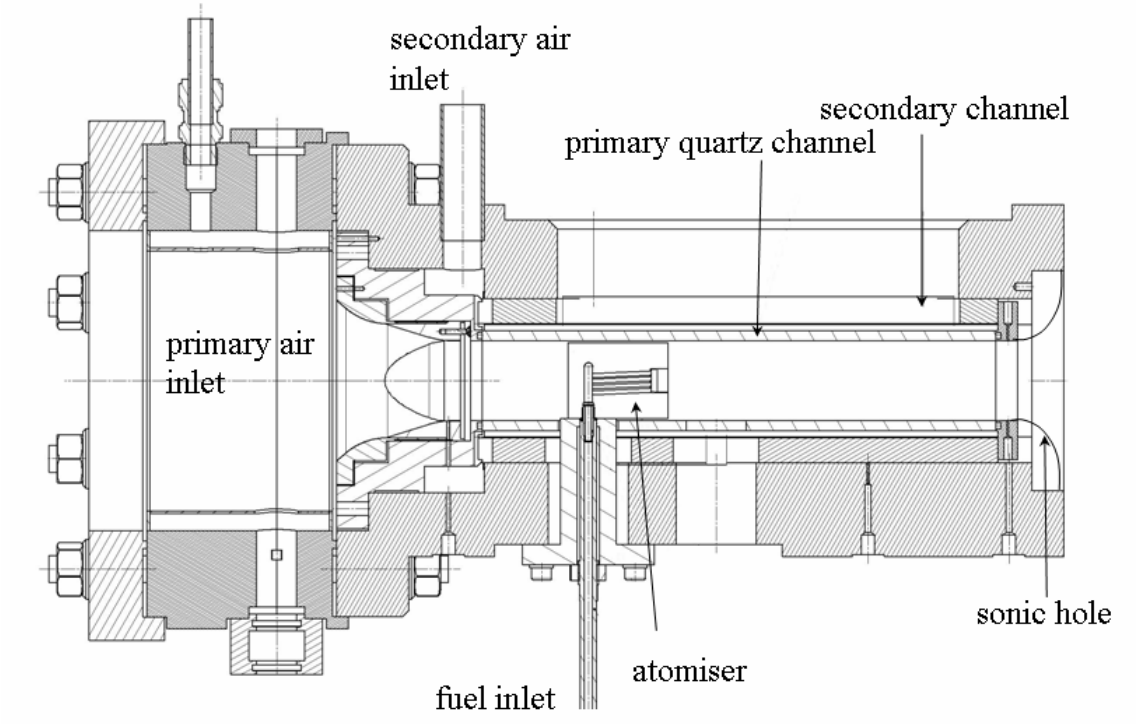

Fig. 2-2 LPP test section

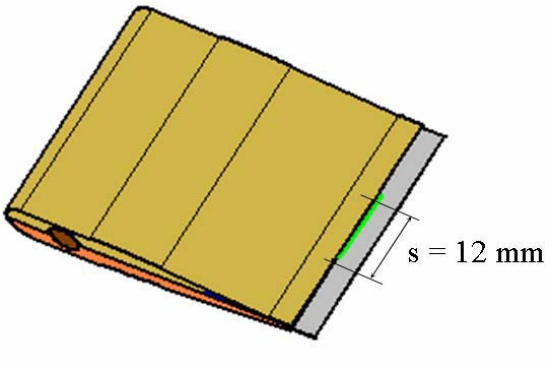

Fig. 2-3 2D prefilming airblast atomiser model

The 2D planar sheet approximation is considered valid if the ratio of the span of the liquid sheet to the thickness of the liquid sheet is greater than 10 [43]. In the set of atomisers designed, the span to thickness ratio is greater than 40. The advantages of having a 2D planar liquid sheet are firstly, the 2D liquid sheet eases visualisation of liquid sheet breakup mechanisms. Secondly, detailed comparison of spray measurements can be made between two different types of airblast atomisers. Also, the fuel consumption is less for a set of experiments.

Of particular significance in the design process is achieving a uniform 2D liquid sheet at the exit of the atomiser slit. This is achieved by channeling the fuel flow inside the atomiser. Figure 2.4 shows the internal geometry for the atomisers. The liquid enters the atomiser through a cylindrical duct as shown in the figure. The liquid is split into 4 rectangular channels. The width of the channel is 2 mm, 36.5 mm long and ~ 0.9 mm thickness. The spacing between the channels is 0.9 mm. The liquid streams flowing through the channels merge inside the atomiser at 9 mm before the atomiser slit. Visualisation at the atomiser slit gave an indication that the disturbances caused by the merging of the liquid channels inside the atomiser are suppressed in this region. Flow

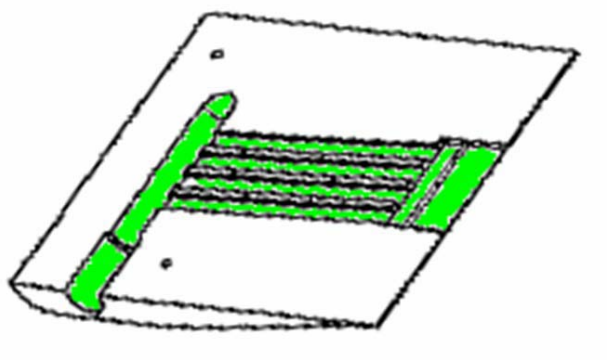

Fig. 2-4 Channeling of fuel inside the atomiser

visualisation experiments and PDA measurements showed that the liquid sheet is uniform along its span (Chapter 3, 4).

Initially, a first set of prefilming and nonprefilming airblast atomisers were designed as shown in Fig. 2.5. Also, a transparent atomiser was designed with a variable prefilming surface. These atomisers were made of brass. The impingement angles at the atomiser slit were typically 5º and 7º. The width of the atomiser is 19 mm, thickness & width of the slit are 300 μm & 18 mm and the length of the atomiser is 50 mm.

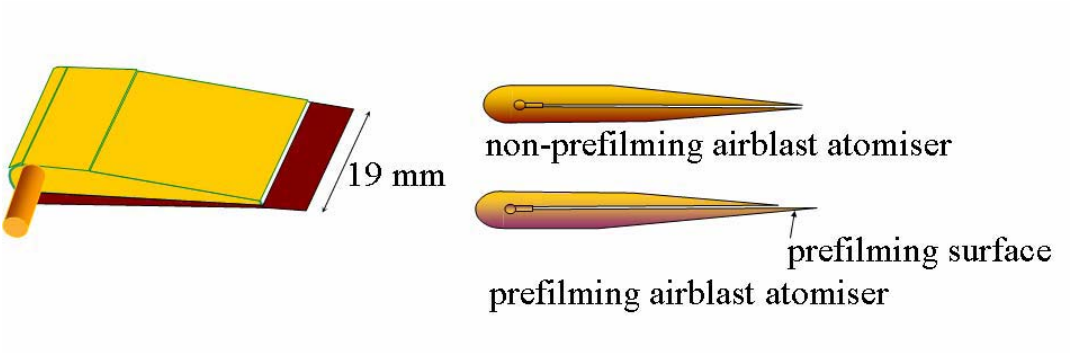

Fig. 2-5 Airblast atomisers for visualisation studies

However, these atomisers had aerodynamic problems due to different impingement angles, and the atomiser spanning only half of the test section height (test section height is 40 mm whereas the atomiser width is 19 mm). The combined effect of the nonuniform pressure distribution and the width caused formation of 'wing-tip vortices' at the edges of the atomiser, as shown in Mie scattering images, Figure 2.6, of cross sectional planes along the axial direction of flow. This has caused change in behaviour of the spray dynamics. There were several practical problems in using these atomisers like leakage, improper welding, and thermal stresses on material at high temperatures.

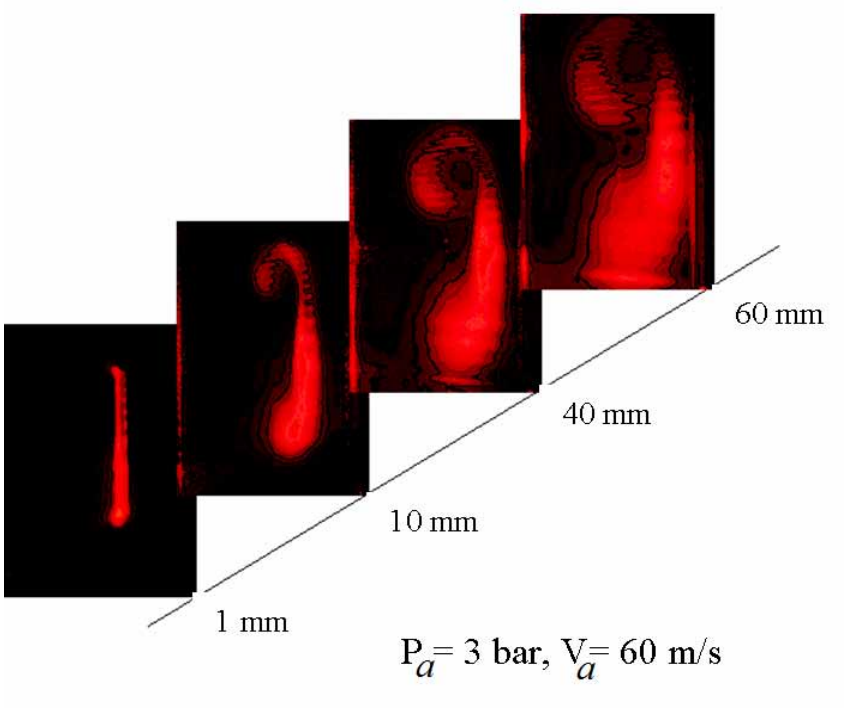

Fig. 2-6 Mie scattering images of the spray

Hence the first set of atomisers was discarded and a second set of atomisers are manufactured. However, the first set of atomisers are used in some cases for flow visualisation as they are performed in the centre of the span of the liquid sheet and the edge effect of the atomiser has little influence on the liquid sheet breakup.

Due to complexity in the atomiser design and difficulty in manufacturing of the atomisers, two atomisers are designed in the second set, a prefilming airblast atomiser with 4 mm prefilming surface and a non-prefilming airblast atomiser. Figure 2.7 and Figure 2.8 show the design of the atomisers. Nickel based alloys are used for the manufacturing of the atomisers. These atomisers can withstand high thermal loads and can be used to test the atomisers at realistic gas turbine operating conditions. The internal geometry for these new atomisers is similar to the first set of atomisers. The new atomisers span the whole test section. The span of the new atomisers is 38 mm. However, the span of the liquid sheet is 12 mm. The impingement angle at the atomiser slit is 0° from both sides of the atomiser.

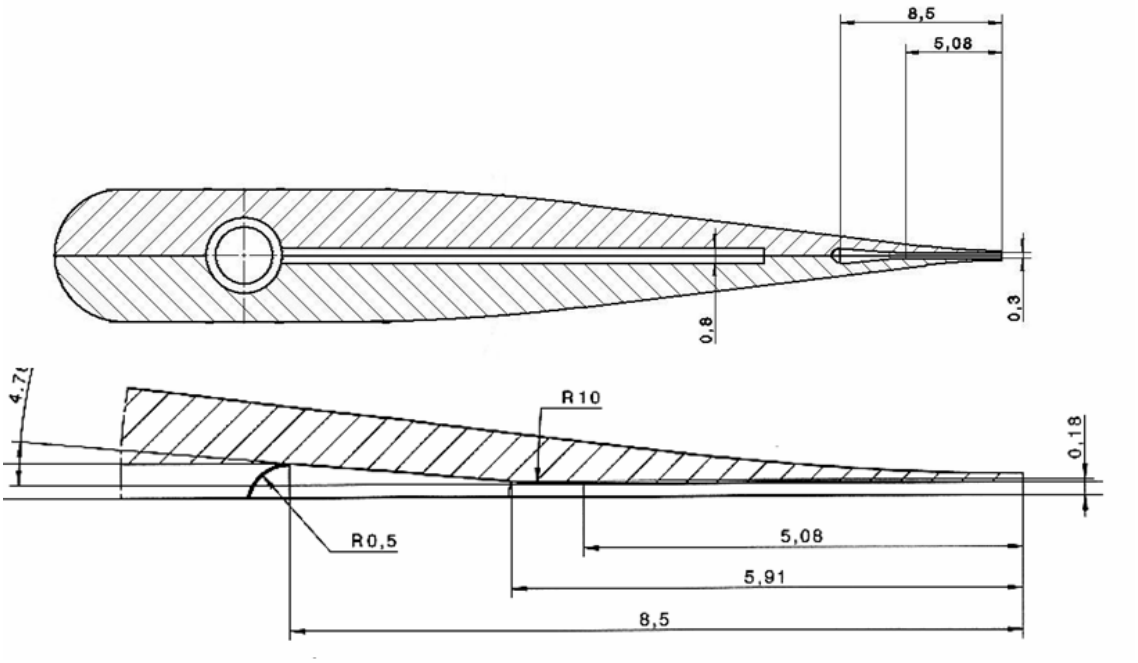

Fig. 2-7 Nonprefilming airblast atomiser model

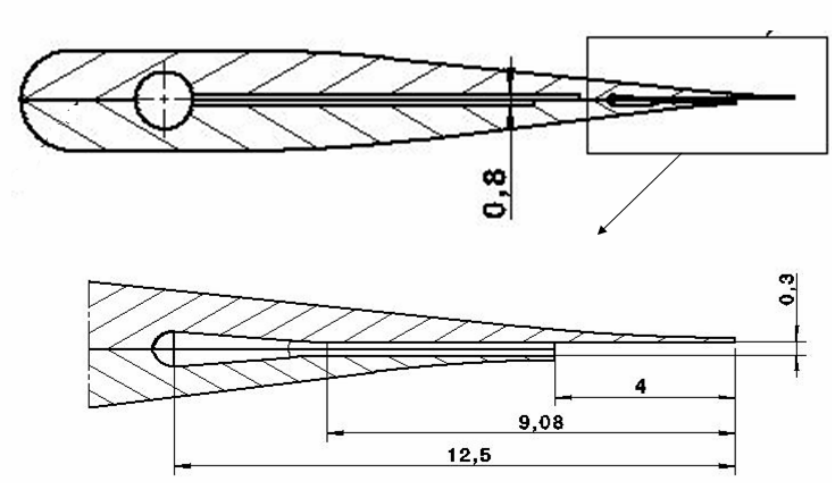

Fig. 2-8 4 mm prefilming airblast atomiser model

The Mie scattering images, Figure 2.9, at different locations for the second set of atomisers show that the 'wing tip vorticity' disappeared and the spray is symmetric along the centre plane of the test section. It can be observed that for the case of the 4 mm prefilming airblast atomiser, there is a slight bulge on one side of the spray due to the presence of prefilming surface. This will be explained in Chapter 3.

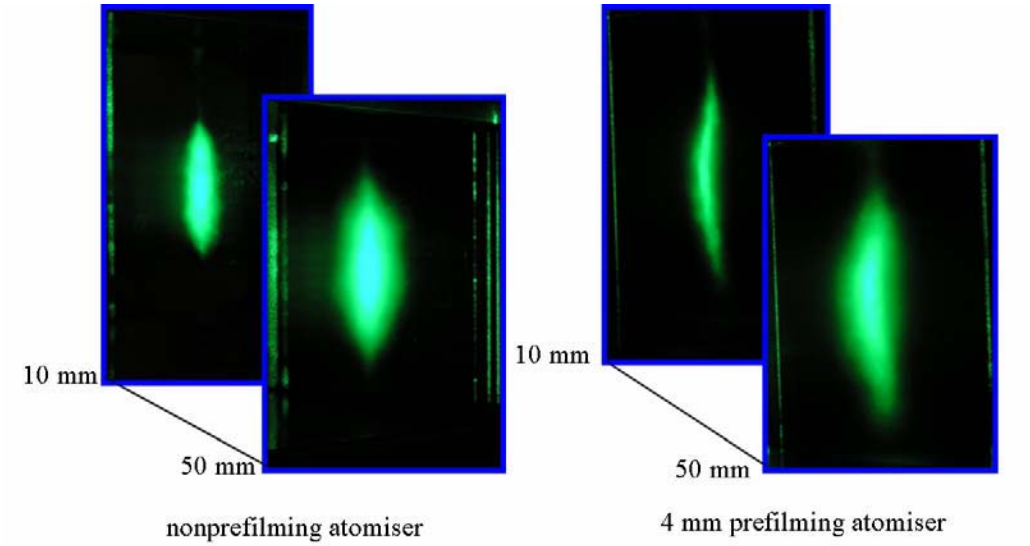

Fig. 2-9 Mie scattering images at P_a = 4 bar V_a = 60 m/s

2.3 OPERATING CONDITIONS

Experiments are conducted at operating conditions where it is feasible to perform flow visualisation measurements and reliable PDA measurements. The static pressure in the test section is varied from 2 bar – 6 bar and the air velocity in the test section is varied from 30 m/s – 90 m/s. For flow visualisation measurements, the mass flux of kerosene is varied from 1 g/s to 8 g/s corresponding to 0.2 m/s – 1.8 m/s. For PDA measurements, the kerosene velocity is kept constant at ~1 m/s. For the operating conditions tested the Weber number[1] in the test section is varied from 32 to 855. At realistic operating conditions the Weber number is a lot higher. The details of the operating conditions and realistic gas turbine conditions are presented in Appendix A. The measurements in the present study are made at ambient temperature. For the maximum mass flow conditions at LPP test rig at ambient temperature, a maximum Weber number of 855 is achieved which is the limitation of test rig.

2.4 EXPERIMENTAL TECHNIQUES

To obtain an insight into the liquid sheet breakup mechanism, background shadowgraphy is adopted. High speed PIV is performed to obtain the velocity field

[1] The Weber number is defined as $We = \frac{\rho_a U_a^2 t_l}{\sigma}$. The thickness and the surface tension of the liquid is mostly kept constant in the present experimental study unless specifically mentioned. Hence, from now on the change in Weber number has to be taken as change in Momentum flux of air.

close to the atomiser. LDA and PDA measurements are performed for characterisation of flow field and spray from atomisers.

2.4.1 Background Shadowgraphy

Background shadowgraphy is a back illumination technique to capture images of liquid flows. In background shadowgraphy experiments, instantaneous imaging and high-speed sequential imaging are performed. The instantaneous imaging is performed to obtain an overall view of the breakup mechanism of the liquid sheet under all operating conditions. For selected operating conditions, high speed sequential imaging is performed. The setups are similar for instantaneous imaging and high-speed sequential imaging. A schematic of the test setup is shown in Figure 2.10 for high-speed imaging.

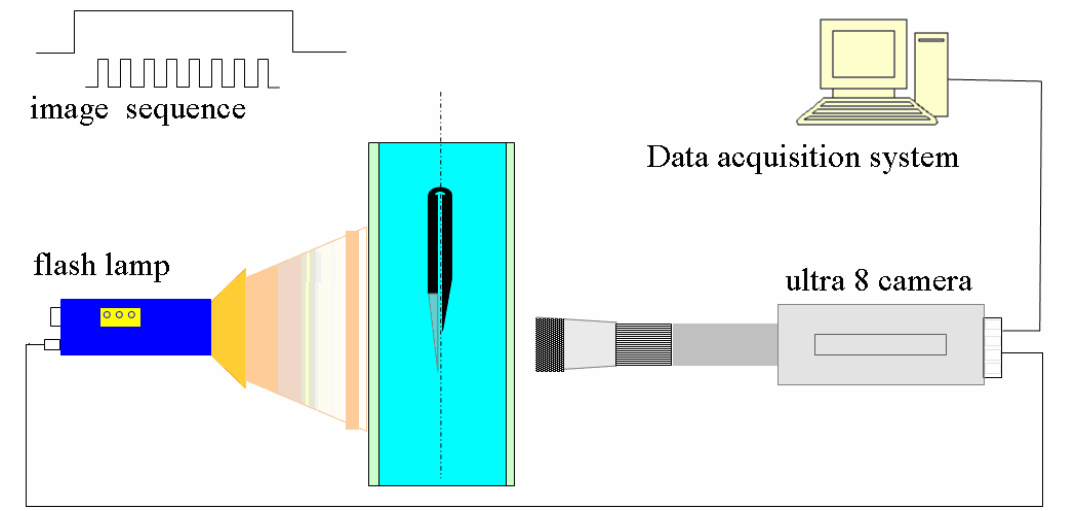

Fig. 2-10 Background imaging setup

A photographic flash lamp, Bowens 1500 model, is used for background illumination. The flash duration of the lamp is approximately 800 milli second. A diffuser sheet is used to make the background uniformly illuminated. A high speed intensified camera, the Ultra 8 model from DRS Hadland Ltd, is used to capture the images. The camera can capture 8 sequential images with a minimum of 1000 frames per second and a maximum of 100,000,000 frames per second. The exposure time can be varied independently from 1 milli second to 10 nano second. The CCD chip has 2048x2048 pixel resolution which is split into 8+1 equal imaging areas giving an effective of 520x520 pixels per frame. When the Camera is triggered, each of the 8 imaging areas is independently triggered based on the shutter speed settings. The 9th image is a time slaved image. The captured sequential images are digitised in 12-bit TIFF format. The imaging area is typically 8 x 8 mm in the visualisation experiments. However, for close up views to observe the sheet oscillations, the imaging area is set at

1.5 mm x 1. 5 mm. The sequential images have interframing time sufficient enough to carry out PIV analysis. So, the same sets of images are also used for High speed PIV analysis.

2.4.2 High Speed PIV Analysis

Consecutive images acquired during high speed imaging, are processed for different operating conditions by PIV software (Particle Image Velocimetry, PIVTEC software developed by Chris Willert). The velocity of the liquid sheet and velocity field of ligaments and droplets are calculated in the near-field of the atomiser. The instantaneous sequential images are acquired at different locations along the flow direction to observe the entire process of liquid sheet breakup, viz, sheet breakup, ligament/large structures breakup, clusters, droplets. The PIVTEC software works on principle of cross-correlation between two sequential images. The velocity field is calculated based on displacements obtained by correlation between the images and the interframing time. For a high correlation between the images, the patterns/particles in the image should have a high spatial frequency with the background. To achieve this, the images have to be processed to remove the background noise.

Processing of Images

The initial purpose of high speed visualisation was to observe the sequential breakup process of the liquid sheet, as discussed earlier. The background was illuminated with the flash lamp. Hence, the liquid structures are in black shade in the images acquired. The cross-correlation algorithm searches for high intensity pixel areas in the images and recognises them as particles. For this reason, the acquired images are preprocessed to be suitable for PIV processing. Figure 2.11 shows the preprocessing methodology. The acquired images are inverted on intensity scale to make the structures appear in high intensity shade. Further processing steps on the images include passing the images through a 3x3 median filter, application of a dynamic threshold to remove CCD chip noise, high pass filter with Gaussian weighting to increase spatial frequency and finally anti-aliasing smoothing to adjust for the background noise. In some cases, binarisation of the images gave good correlation peaks. Figure 2.11(a) shows two sequential raw images, image 001, 002. The movement of the liquid sheet can be seen over the prefilmer surface. The edge of the prefilmer surface can be noticed. Figure 2.11(b) shows the corresponding processed images. As can be observed, most of the structures are clearly represented in the processed images.

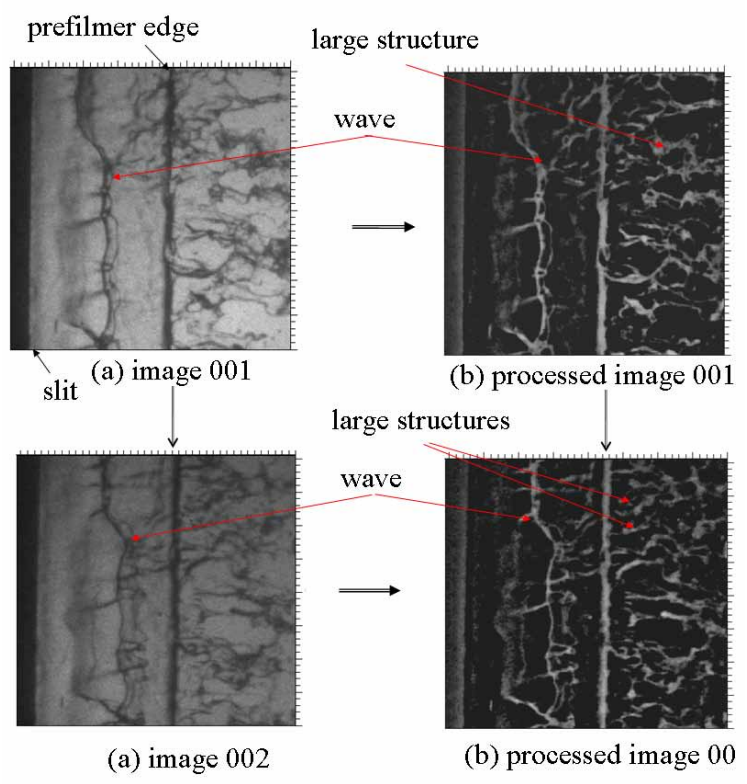

Fig. 2-11 Image preprocessing for PIV

Evaluation

The processed images are evaluated with an interrogation widow size of 32x32 pixels with 50% overlap between adjacent interrogation windows. This gives a resolution of 16x16 pixels for the image plane. In classical PIV images, the flow is seeded with particles of micron size that occupy 1-2 pixels in the images. However, in the images captured close to the atomiser, the liquid sheet and the ligaments/structures are large and occupy several pixels. So, a multigrid cross-correlation algorithm is used with an initial sampling window of 128x128 pixels. The advantage of this algorithm is that the movement of large structures is recognised as the algorithm first interrogates on a bigger window (128x128) and subsequently reducing the window size to the initially set interrogation window (32x32). Also, the peak of the correlation occupies several pixels, the peak detection is carried out by centre of mass, as explained below. Figure 2.12 shows the evaluation methodology.

The rectangular box in the left picture is an interrogation area in one of the two images, also called the interrogation widow. The interrogation window in the two images is shown in picture to the right. The displacement of the wave can be noticed in the windows. These windows are cross-correlated and the correlation between the interrogation windows is plotted in another widow called correlation window. The intensity in the correlation window shown above indicates a good correlation. The peak intensity spot, in the correlation window, gives the displacement and direction when measured from the centre of the crosswire. However, in this case, the high intensity is not at a single spot but a small area. The peak of this high intensity area is recognised by finding the centre of mass.

A vector in the left picture shows the displacement of the wave. This displacement was also measured manually from the two images and matches exactly with the displacement given by the software. Figure 2.13(a) shows the displacement vectors at various positions in the image. For clarification, two consecutive images are shown. As can be seen the software measures the displacement of the structures. In Figure 2.13(a) image 001, the wave and structures are at the tail end of the vector in the interrogation window in blue colour. In image 002, the displacement of the wave and structures reach the head of the vector showing the accuracy levels of the algorithm. However, as can be seen at the prefilmer edge, the displacement vectors are small. This is due to the constant intensity in both of the images at the edge. Hence at this location in the image, information on velocity field is misleading. Also, it can be observed, that at some places in the image the displacement vectors are in opposition to the direction of flow. These are termed as outliers and are discarded during evaluation. Figure 2.13(b) shows a typical velocity contour plot on the prefilmer surface. The velocity of

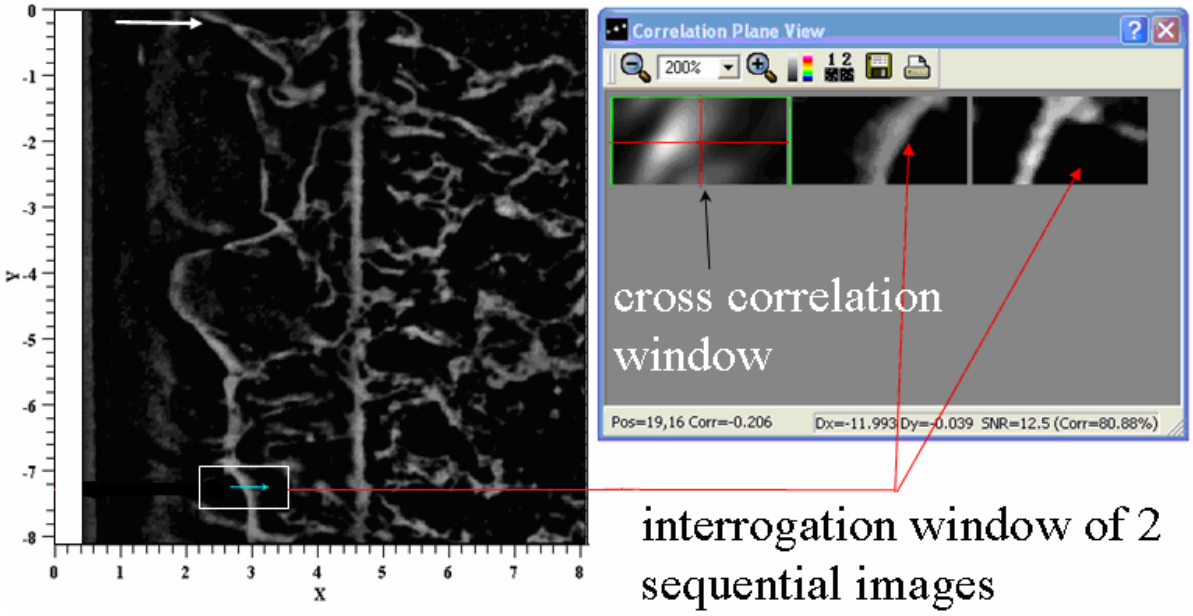

Fig. 2-12 Evaluation of PIV images

propagation of the liquid sheet is around 3-5 m/s at the centre of the prefilmer. The velocity of the liquid is ~1 m/s at the entrance of the atomiser slit for this operating condition (calculated based on metered liquid flow rate). The region in the images covers approximately 8x8 mm; therefore several sets of image sequences are acquired along the flow direction. The depth of field is around 1 mm. Hence the particles in the images line up in a plane of maximum 1 mm thickness. A total of approximately 300 images are processed to obtain the velocity contours of the liquid at each axial location and operating condition.

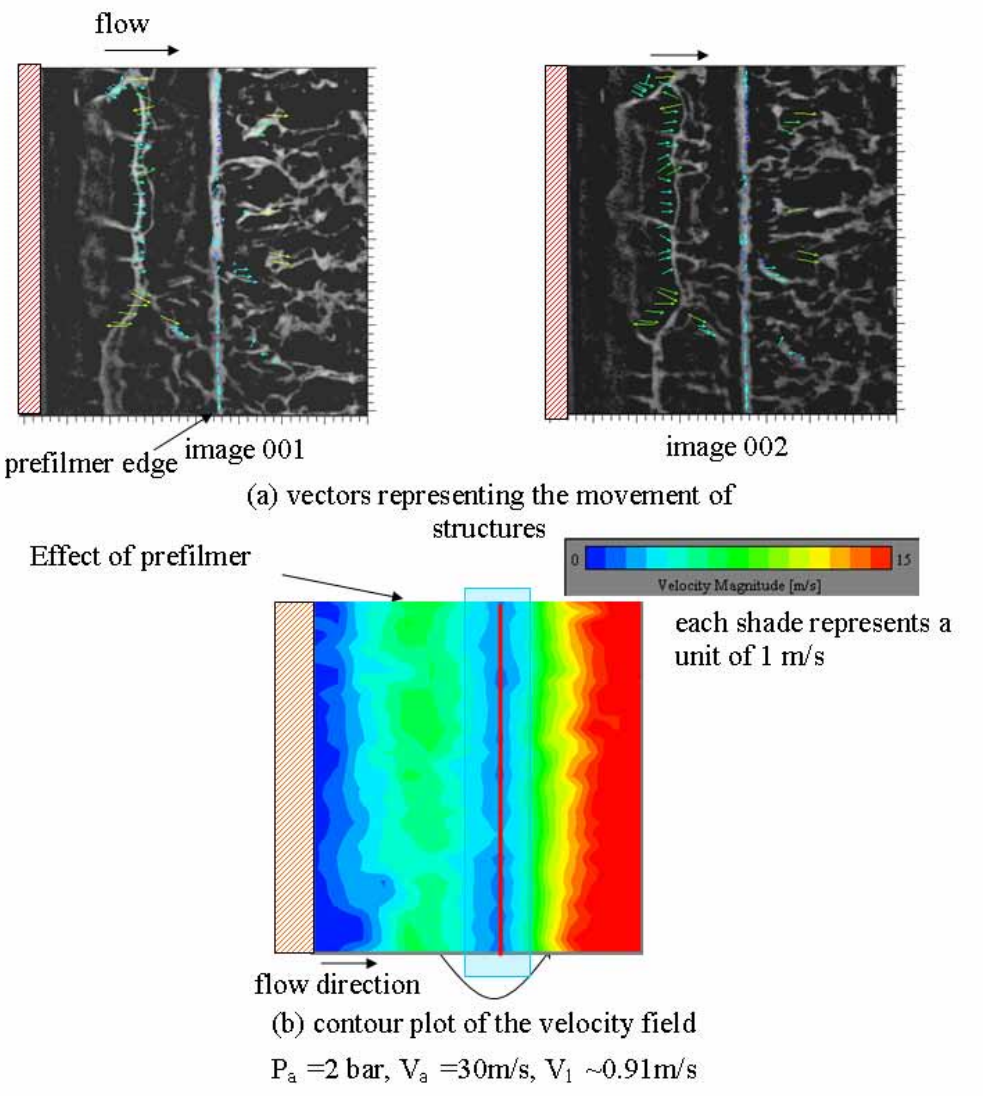

Fig. 2-13 Velocity field of kerosene phase

2.4.3 LDA Measurements

The Laser Doppler Anemometry (LDA) is a non-intrusive point-measurement technique to measure the local velocity of the flow. The velocity is calculated from the

Doppler frequency shift. The operating principle of LDA is explained as follows. A Laser beam from a continuous laser source is split into two beams as shown in Figure 2.14.

The two beams typically have a Gaussian intensity profile. The beams intersect at an angle forming a stationary interference fringe pattern of alternating dark and bright bands with constant spacing. The region of interference fringe patterns is called measurement volume. It is ellipsoidal in shape. The spacing between the fringes is a function of laser wavelength and angle between the two beams. The following equation gives the spacing between the fringes.

$$\delta = \frac{\lambda}{2.\sin(\theta/2)} \qquad \text{Eq.2-1}$$

where δ is fringe spacing, θ angle between the beams, λ wavelength of the laser beams.

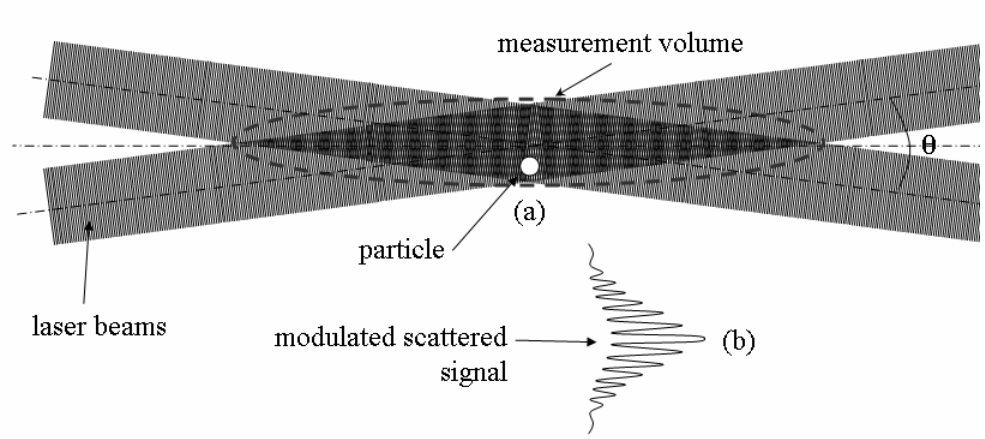

Fig. 2-14 Interference fringe pattern

The flow is seeded with small particles typically around 1 μm in size that follow the flow. As the particles travel through the measurement volume they scatter light which is modulated in intensity, as shown in Figure 2.14(b). The scattered light signal has a definite frequency, called Doppler frequency that is dependent on the velocity of the particle. These particles are few times bigger than the wavelength of light, hence the scattered light can be estimated by Mie scattering principles. The scattered light signal is collected at an angle by photomultiplier detectors and processed to obtain the Doppler frequency shift. The velocity can be easily calculated once the Doppler frequency shift is measured. The velocity of the particle is calculated based on the following equation

$$U_{flow} = f_d.\delta \qquad \text{Eq.2-2}$$

where U_{flow} is the velocity component of the particle, f_d is Doppler frequency shift.

The velocity that is measured perpendicular to the plane of the fringe pattern gives only one component of the velocity vector. However, the measured velocity does not carry any information on the direction of the particle with respect to fringe pattern. A Bragg cell is used to overcome the directional ambiguity of velocity. The Bragg cell shifts the frequency of one of the laser beams. The frequency shift produces a moving fringe pattern. By measuring the phase shift with respect to moving fringe pattern with two photomultipliers, directional ambiguity can be eliminated [17]. To measure two velocity components, additional laser beams of different wavelength are used perpendicular to the plane of the first beams.

In the present study two component LDA measurements are performed to characterise the velocity field of the incoming flow to the atomiser and downstream of the atomiser. A green beam, λ = 514.5 nm, and blue beam, λ = 488 nm, from an Argon ion laser (Coherent Inc. make), are used for measuring two components of velocity. The beams are passed through beam splitter to obtain two additional beams. One green and one blue beam is passed through a Bragg cell which provides an optical frequency shift of 40 MHz to the beams. The four beams are transmitted by an optical fiber arrangement to the transmitting optics. A schematic of the transmitting and receiving optics is shown in Figure 2.15.

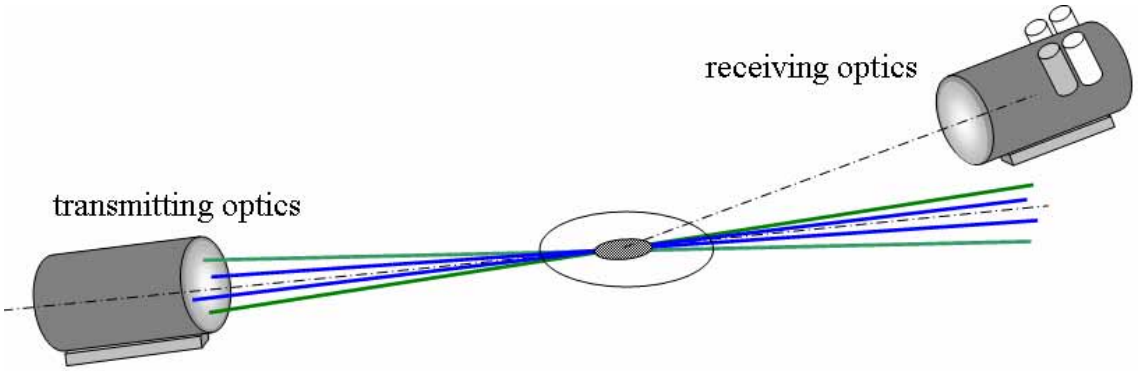

Fig. 2-15 Schematic of LDA setup

The transmitting optic, from Dantec Inc- model 9060x0321, with a converging lens of 310 mm focal length is used to converge the four beams to form interference fringe pattern at the point of focus. The details of the transmitting optics are given in Table 2.1. The receiving optic, from Dantec Inc- PDA 58N10 model, is placed at an angle less than 20º degree to obtain maximum scattering light signal and also to reduce the effect of scattering particle diameter on intensity.

LDA settings	axial velocity component	transverse velocity component
Wavelength (nm)	514.5	488
Fringe spacing (μm)	5.32	5.05
Number of Fringes	13	13
Gaussian diameter (mm)	1.35	1.35
Beam separation (mm)	30	30
Minimum velocity (m/s)	-32	-30
Maximum velocity (m/s)	160	152

Table 2-1 Transmitting optics arrangement

2.4.4 PDA measurements

Phase Doppler Anemometry (PDA) is an extension of the LDA principle to measure the size, velocity and concentration of droplets in sprays. The size of the droplets is calculated based on the phase difference of the Doppler frequencies measured by multiple detectors located at different angles. The operating principle of PDA is explained as follows. Similar to LDA, the laser beams interfere forming interference fringes.

The particles traveling through the fringes scatter light with a Doppler frequency shift. Two photomultiplier detectors, separated by a constant distance, are used to collect the scattered light signal. Both the detectors will observe the same Doppler frequency shift but with a relative phase difference, as shown in Figure 2.16.

The phase shift is proportional to the size of the particle and detector spacing and the mode of scattering, viz. refraction and reflection [74]. Apart from the velocity ambiguity as in LDA, an additional ambiguity occurs in measuring the size of the particle occurs if the phase of the two signals is more than 360º. As shown in Figure 2.16, a large particle cannot be distinguished from a small particle if the large particles produce a phase shift greater than 360º.

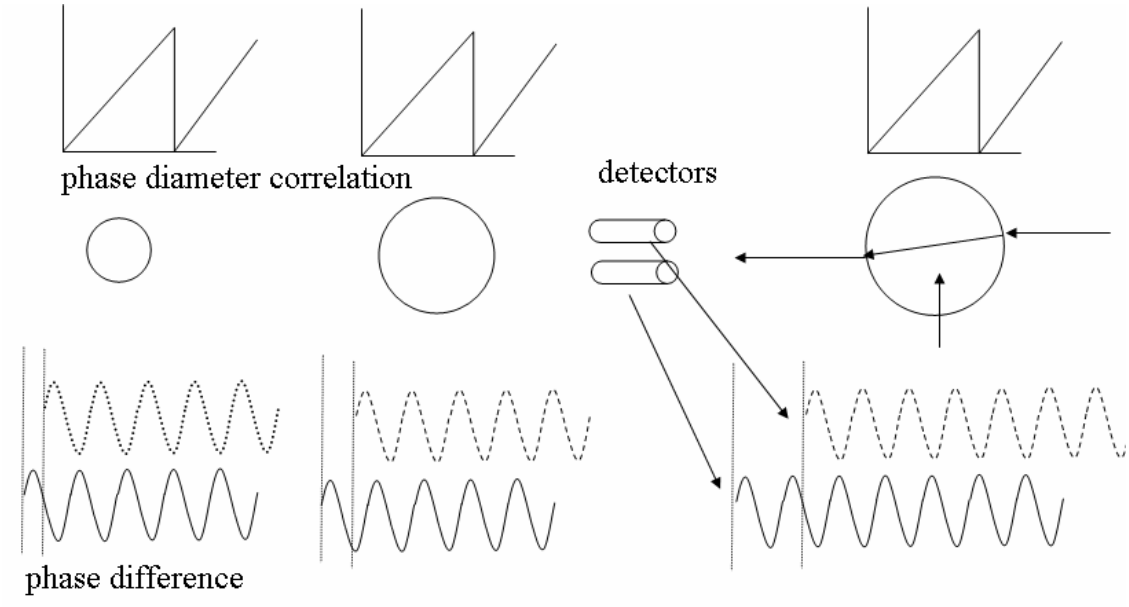

Fig. 2-16 Phase difference of scattering signal from detectors

In order to overcome this problem, an additional photomultiplier detector is placed closely to one of the detectors thus phase variation is slow. It is also used for consistency check of the size calculation measured by the detector pairs. The size of the particle is calculated as

$$D = \frac{phase.\lambda}{\pi.n_1.\beta} \qquad \text{Eq.2-3}$$

where D is the diameter of the particle, λ is wavelength of light, n_1 is index of refraction of the scattering medium and β is called geometric factor which depends on the mode of scattering and optical configuration and is given by

$$\beta = 2\left\{\sqrt{1+n'^2-\sqrt{(2)}.n'\sqrt{f_+}} - \sqrt{1+n'^2-\sqrt{2}.n'\sqrt{f_-}}\right\} \qquad \text{Eq.2-4}$$

for refraction, where $f_{+/-} = 1+/-\sin(\theta/2).\sin\phi.\sin\psi + \cos(\theta/2).\cos\phi$, n' = n_1/n_2, n_1, n_2 is index of refraction of the particle. Figure 2.17 shows the orientation of angles with respect to coordinate system. The details of the above equations are given in Dantec Manual [17].

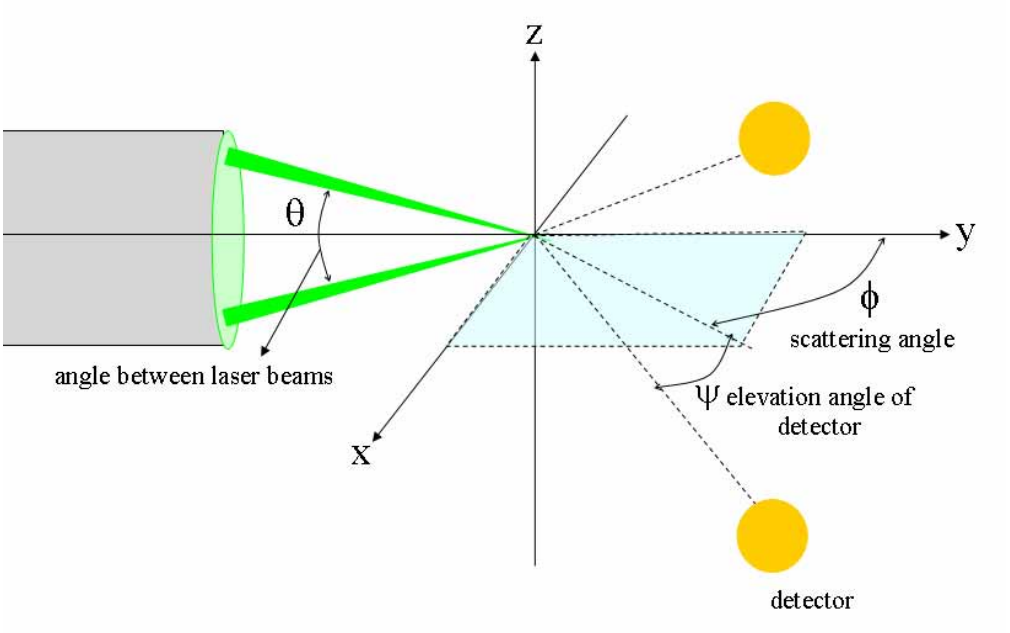

Fig. 2-17 Orientation of PDA system

A 2-D standard PDA setup, Dantec Inc.-PDA 58N10, is used for measurement of droplet diameters and velocity of particles. A green beam, λ = 514.5 nm, and a blue beam, λ = 488 nm, from an Argon ion laser of Coherent make, are used for measuring two components of velocity of the droplets. A schematic of the setup is shown in Figure 2.18. In the current study, the spray is dense with high droplet concentration. Hence, two beam expanders of 1.85 and 1.98, with an effective beam expansion of 3.663, are used to increase the spatial resolution. A converging lens of 310 mm focal length is used on both transmitting optics and receiving optics. The beam separation is 24 mm. The optical settings give the measurement volume diameter of 34.2 μm. The receiving optics is positioned at α = 58° which is close to Brewster angle (ψ = 65° for kerosene). The details of PDA optical settings are given in Table 2.2.

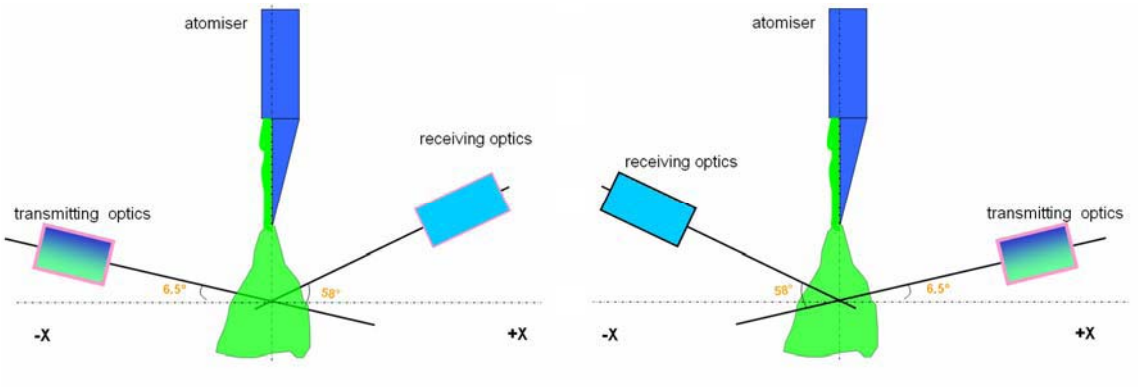

Fig. 2-18 Positioning of transmitting optics

A total of 40000 samples are acquired at each measurement point. The validation levels are set at +2 dB. The liquid volume flux is calculated by a volume flux algorithm developed in-house, which works on burst lengths for the determination of the detection volume [11].

T. Optics (offset)	4.5, 6.5°	f of R. Optics	310 mm
Laser Power	75 mW	Phase Factor (U1-U2)	4.254°/μm
Gaussian Diameter	1.35 mm	Scat. Angle (ψ -68°)	58°
Polarisation angle	parallel	Aperture	2 mm
Beam Expander	3.6663	Slit Width	300 μm
Beam Separation	24 mm	Bandwidth	36 MHz
F of T. optics	310 mm	Gain	High
Fringes spacing	6.65 μm	Diameter (max)	122.2 μm
Meas. Vol. Dia.	34.2 μm	Axial Velocity (V)	- 37.8 m/s
Refractive Index	1.46		-+ 199.5 m/s
		Mode	Refraction

Table 2-2 PDA optical settings

Due to constraints at the test section, the transmitting optics of PDA system is offset by 6.5° to the perpendicular plane of flow direction. In order to observe the effect of the transmitting optics offset, measurements are conducted at two offsets, 4.5° and 6.5° at selected operating conditions. Also, the spray is dense in the present studies. To validate the effect of density of the spray on PDA measurements, the transmitting optics is flipped from negative X direction to positive X direction and measurements are repeated at selected operating conditions. The details of the effect of transmitting optics positioning on measurements are explained in Appendix D.

The PDA measurements are conducted at several locations to characterise the spray. The coordinate system for the PDA measurements is shown in Figure 2.19a. To validate the spray two dimensionality, as shown in Figure 2.19b, measurements were conducted at a X-Y plane (x = -16-16 mm, y = -6-6 mm in 1mm and 2mm intervals) at z = 90 mm from the exit of the atomiser slit. Also, measurements were carried out at x = -16-16 mm, y = 0 mm at z = 10-25 mm and 45-90 mm for characterising the SMD and dispersion of the spray. The measurements could not be performed from z = 25 mm to z = 45 mm due to immovable obstructions around the test section.

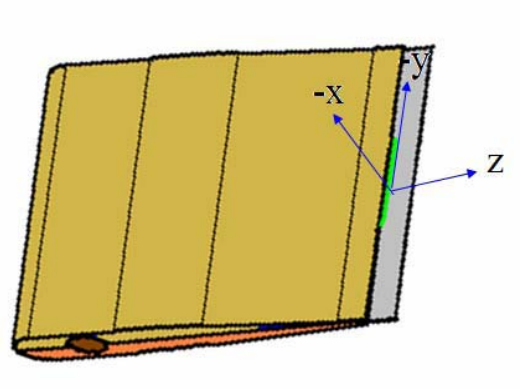

(a)

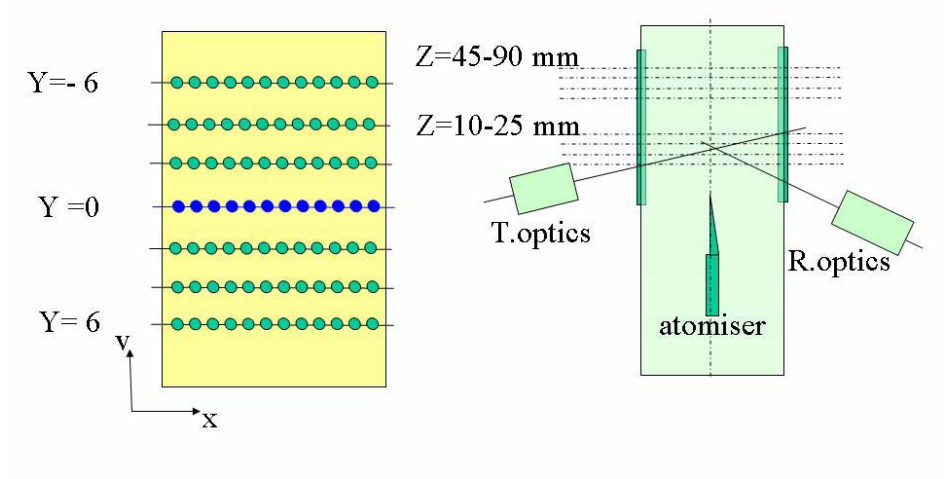

(b)

Fig. 2-19 PDA measurement locations

CHAPTER 3

FLOW VISUALISATION OF LIQUID SHEET BREAKUP

This chapter discusses the flow visualisation studies on nonprefilming and prefilming airblast atomisers. High speed Background Shadowgraphy experiments are performed in the vicinity of the atomisers to observe the liquid sheet breakup mechanism. The air stream that interacts with the surface of the liquid sheet produces different breakup regimes at various operating conditions. The different liquid breakup mechanisms observed for nonprefilming and prefilming atomiser are discussed in detail. The stability of the liquid sheet at the atomiser lip is also discussed. Quantitative analysis of the High speed images is also performed.

3.1 BREAKUP MECHANISM OF A LIQUID SHEET ON A PREFILMING SURFACE

3.1.1 Formation of surface waves

In the present experimental study on prefilming airblast atomisers, liquid emerges from a slit at the atomiser and one of the surfaces is exposed to the surrounding air. When a surface of liquid is exposed to moving air, the surface is perturbed. The perturbations are produced due to the local differential pressure head between the two fluids. These perturbations propagate due to the momentum exchange between the two fluids in the form of differential kinetic head. The growth of these instabilities leads to the formation of small amplitude waves on the surface of the liquid sheet. The growth rate depends on the conditions of the surrounding fluid. A schematic of formation and growth of the small amplitudes waves on the surface of the liquid sheet on a prefilming surface is shown in Figure 3.1 (a). Figure 3.1(b) shows the formation of small amplitude waves on the surface of liquid when it emerges from the slit of the prefilming airblast atomiser.

It is a general perception that the small amplitude waves formed on the liquid surface are due to imperfections inside the atomisers. Even though this is one of the reasons for formation of small amplitude waves, it is not the only reason as explained above. As the air-stream passes over the liquid surface, a crest or a trough is formed on the liquid surface, because of differential pressure, creating a wave with small amplitude (water waves) as explained by Einstein [22], Figure 3.1(a). The small amplitude waves are symmetric and have constant amplitude which can be explained by inviscid potential theory. As can be observed in the Figure 3.1 (b), small amplitude waves appear after a

sufficient length from the atomiser slit. The small amplitude waves in Figure 3.1(b) are 3 dimensional in nature due to the local turbulence effects. These small amplitude waves grow in amplitude depending upon the force balance between the external forces and internal forces acting on the liquid sheet and form asymmetric waves with different sections of the wave traveling at different speeds, the details of which are explained below.

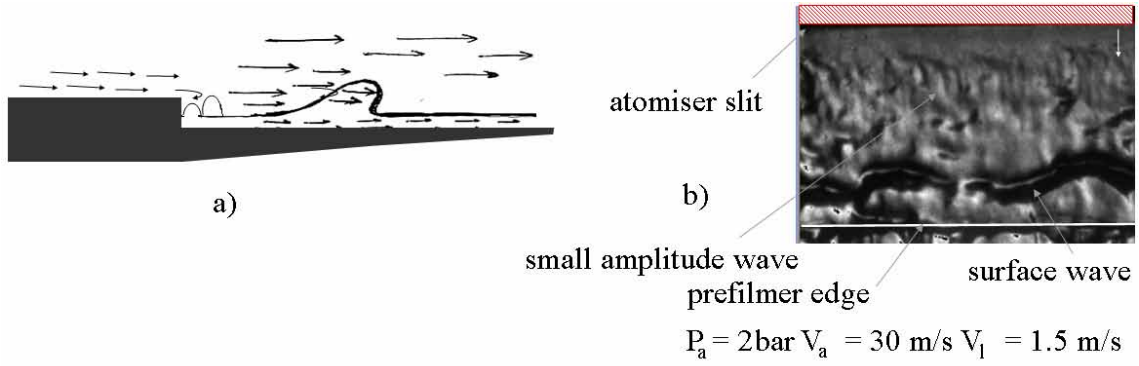

Fig. 3-1 Formation of small amplitude wave

These asymmetric waves when grow in amplitude forms into a surface wave on the liquid sheet. Figure 3.2(a) shows the formation of surface waves. The surface wave propagates in the direction of the resulting forces, similar to gravity waves formed on the water surface in shallow waters. The Gravity waves are mainly formed due to the effect of gravity on the water surface. When the gravity waves approach the sea shore, the speed of the wave is higher at the top of the wave than the speed at the bottom due to gravity. In the present case, the gravity effects are negligible. These surface waves are formed at regular intervals, the wavelength between the waves depends on the local energy balance which will be explained in Section 3.1.2. The wavelength of these waves is around 1-2 mm, as measured from the images. Usually waves with wavelengths less than 1 cm are termed capillary waves. Surface tension forces dominate the propagation of capillary waves. However, the behaviour of the surface waves is similar to the gravity waves. The reason is due to the predominant effect of surface tension forces and viscous forces on the propagation of the surface wave at small length scales (the thickness of the liquid sheet being 300 microns). The wave speed is determined by the balance of internal viscous forces and surface tension forces acting in and on the liquid with the external aerodynamic forces. The external aerodynamic pressure is balanced by the surface tension force acting on a small elemental area of $\Delta x \Delta y$ as shown in the Figure 3.2(b). The force balance shows the effect of surface tension forces and viscous forces

as a function of wave amplitude[2] [26]. The combined effect of these forces at such small length scales is similar to the effect of gravity on waves at the sea shore.

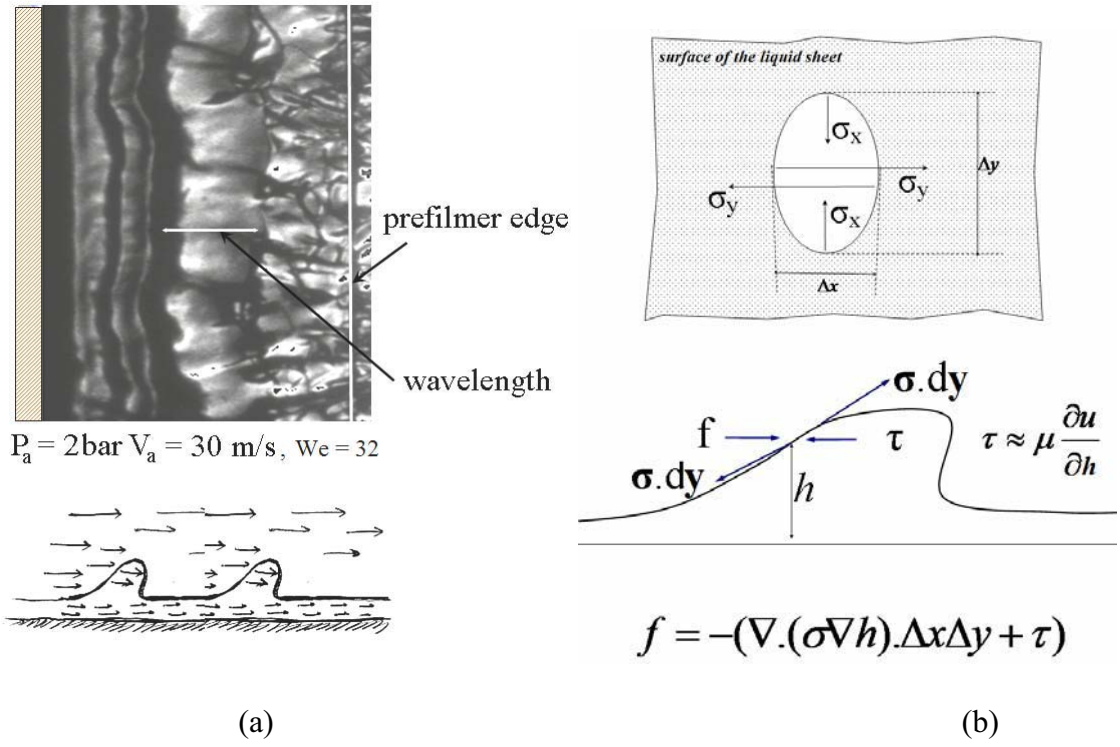

Fig. 3-2 Propagation of surface waves

Figure 3.3 shows the propagation of surface waves at a pressure = 2 bar and air velocity = 30 m/s, We[†] = 32 (P_a = 2 bar, V_a = 30 m/s). Typical sequential images of propagation of surface waves on the prefilming surface are shown from front view and side view. As the surface waves propagate, they gain velocity with the top of the wave moving at higher velocity and increasing amplitude than the lower surface of the wave (as explained above). Depending on the wave speed and the balance between the forces, the amplitude of the wave reaches the limiting value where it cannot sustain the velocity difference inside the wave and plunges ahead as shown in Figure 3.3(a) (image 03). This is termed wave plunging. Figure 3.3(a) (image 01-04) shows a sequence of images of this behaviour. It can be seen that in Image 03, the wave plunges ahead. In Image 04, the plunged wave travels ahead of the surface wave. The typical velocity of the wave is around 3 m/s measured from the sequential images and also by the PIV software,

[2] The external force balance to internal surface tension forces acting on an elemental area as a function of amplitude for small deflections is shown in Feynman lecture series [26]. The viscous force term is added since it is predominant force acting at the length scales under consideration.

[†] As defined in Chapter 2, Weber number is based on the liquid sheet thickness unless explicitly mentioned.

Section 3.7. It is measured from consecutive images that the plunged wave travels at twice the velocity of the surface.

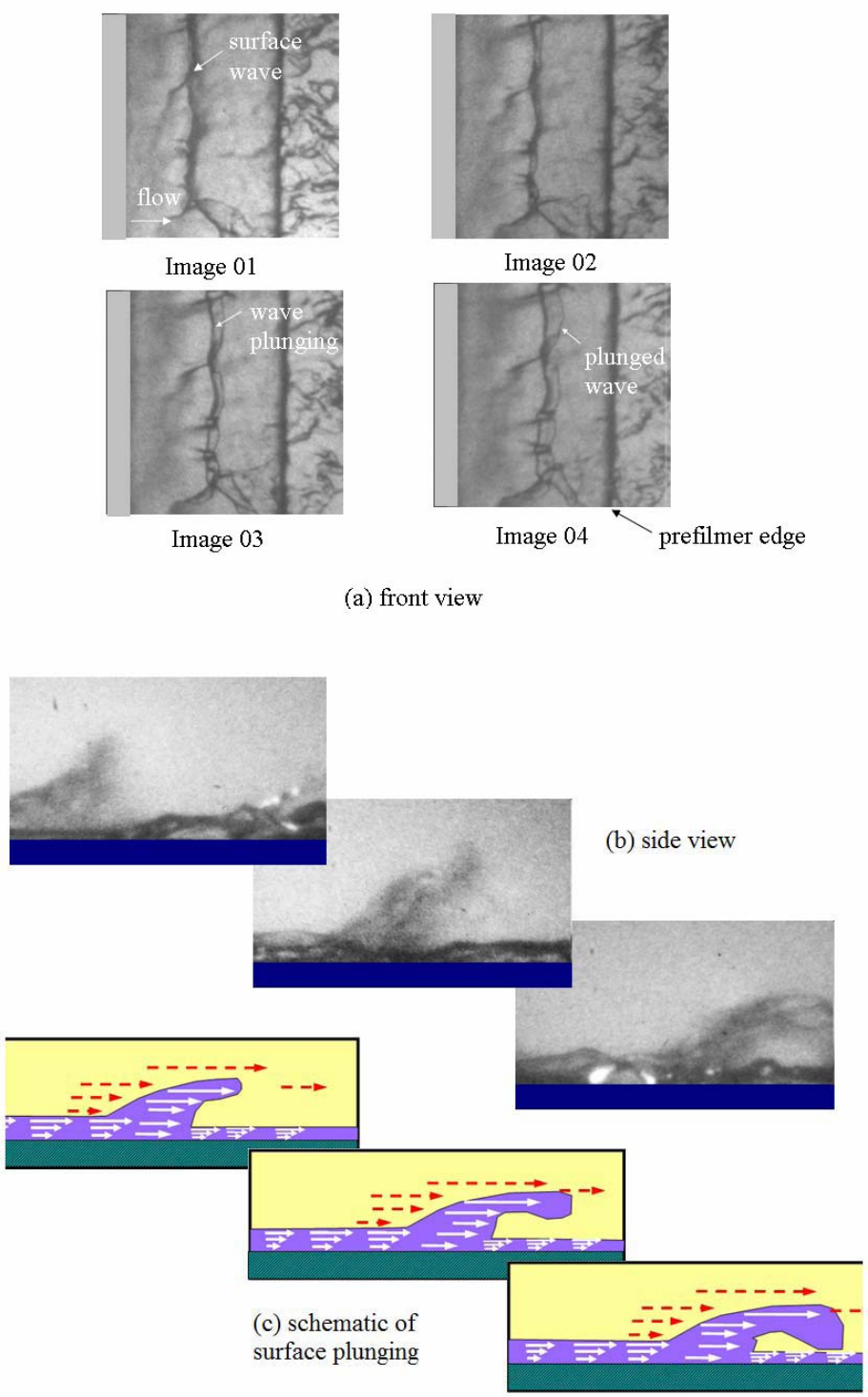

Fig. 3-3 Phenomena of wave plunging at low Weber number
We = 32 (P_a = 2 bar, V_a = 30 m/s), t_l = 300µm

Even though the wave plunges, it does not break from the liquid surface forming layers of different thickness. The liquid sheet is also intact until the edge of the prefilming surface. The disintegration of the liquid sheet is similar to liquid sheet breakup in the nonprefilming atomiser. Figure 3.3(b) shows the wave plunging phenomena in side view. A schematic of wave plunging is shown in Figure 3.3(c).

3.1.2 Surface stretching and Formation of ligaments

As the surface waves propagate as shown in Figure 3.2 and Figure 3.3, the wave ahead propagates at higher velocity than the wave that is following. This causes increase in spacing between the waves and hence induce stresses on the liquid surface. The surface stresses are balanced by the surface tension forces. It is observed that the surface wave (also termed as spanwise waves in literature) propagates along the entire width of the prefilmer surface if the air velocity and the static pressure is low as indicated in Figure 3.3. At limiting conditions, the surface tension forces accumulate liquid mass trying to balance the induced stresses, Figure 3.4(a). This causes the formation of ligament like surface undulations widely known as streamwise waves. As shown in Figure 3.4(b), since the external forces acting per unit area are constant, the surface stresses induced by external forces in axial direction by stretching the liquid surface is balanced by shrinking in spanwise direction. The surface waves now propagate in between these ligaments like undulations. Usually, the spacing between the ligaments is uniform. The small variations in the ligament spacing are due to local turbulence effects. Since the energy balance occurs globally, the ligaments spacing and thickness are considered to be equidistant. The spacing of the ligaments into individual ligaments depends on thickness of the liquid film, surface tension between the fluids, viscous forces in the liquid sheet and aerodynamic forces acting on the liquid surface. If the Weber number is low, as shown in Figure 3.3, the surface wave propagates along the entire width of the prefilming surface. However, if the Weber number is high, the surface wave propagates in between the ligament like undulations. These ligaments like surface undulations formed on the liquid surface do not break into individual ligaments on the prefilming surface.

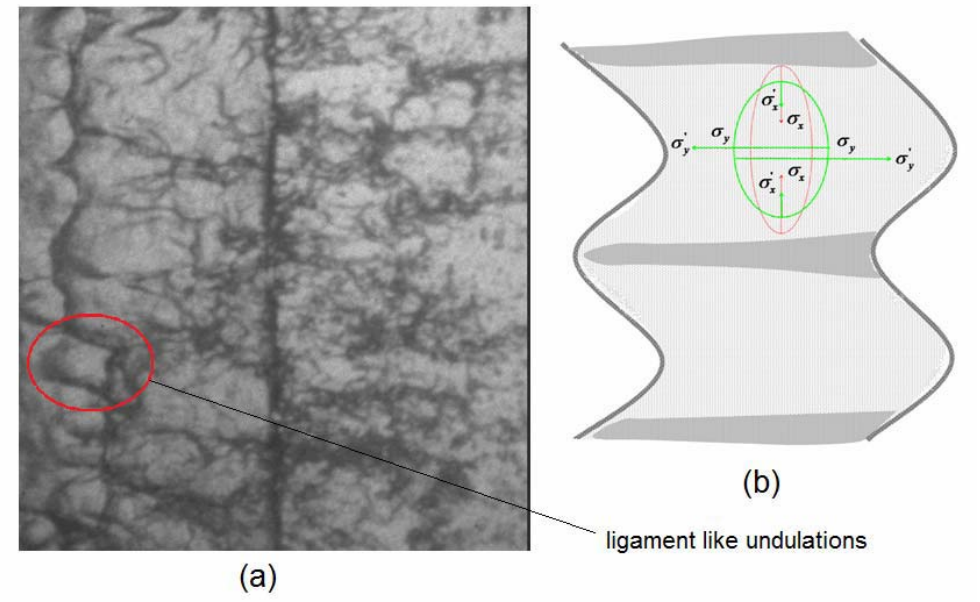

Fig. 3-4 Formation of ligaments

3.1.3 Surface Stripping from the Liquid Surface

However, as the air velocity increases, due to high relative velocity between the liquid surface and air, the wave reaches the limiting amplitude close to the atomiser slit. If the forces acting on the wave are strong enough to overcome internal viscous forces and surface tension forces, the wave breaks from the surface instead of plunging. This phenomenon is termed as surface stripping. Figure 3.5 shows the surface stripping phenomenon at We = 380 (P_a = 6 bar, V_a = 60 m/s). The surface stripping of the liquid surface can be observed in Figure 3.5 (a) in images 02 & 03. It can be seen that the spanwise waves propagate in between the ligament spacing. The reason of formation of these ligaments is already explained. Figure 3.5 (b) shows a sequence of images of surface stripping in side view. As can be clearly observed in the Figure, a lump of liquid mass is stripped off from the liquid surface. As the mass strips off from the surface, the stripped mass accelerates depending on the aerodynamic forces experienced by the lump of the liquid. Typical velocities reached are ~ 20 m/s under the conditions mentioned (measured from the sequence of images). This velocity is normally achieved by droplets/clusters far downstream of the atomiser edge indicating that the stripped mass is above the liquid surface. The details of the velocity-field of the liquid phase are given in Section 3.8. It can also be observed that the thickness of the liquid sheet decreases as the surface stripping occurs due to the loss of mass. As the liquid reaches the prefilmer edge surface stripping increases and the liquid sheet further reduces in thickness.

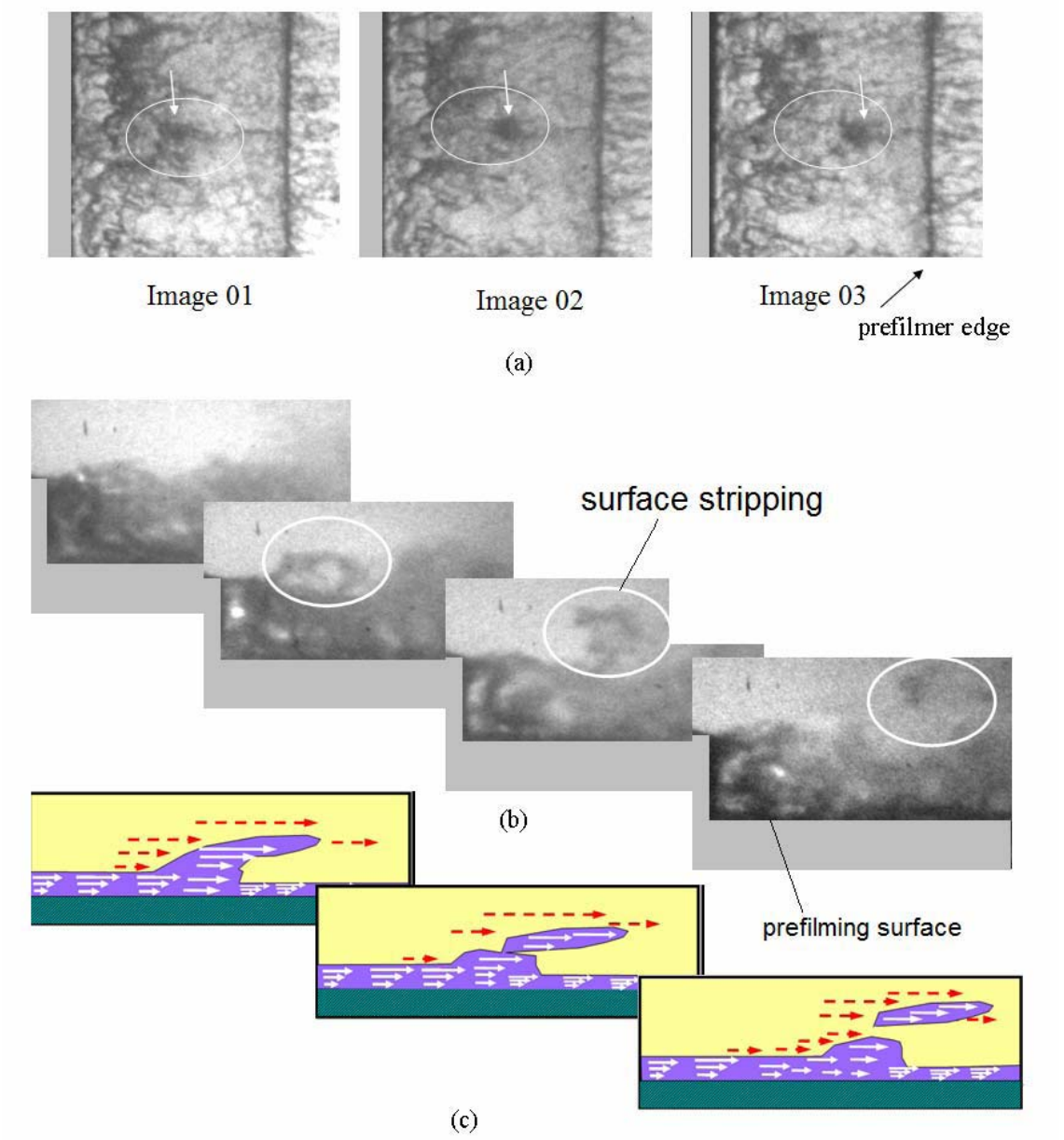

Fig. 3-5 Phenomena of surface stripping at high Weber number
We = 380 (P_a = 2 bar, V_a = 30 m/s)

Figure 3.5 (c) shows the schematic of surface stripping of the liquid surface. It is important to note that at constant velocity, as the ambient pressure increases, the amplitude of the surface waves decrease. This is due to the normal pressure acting on the waves. Since the momentum of air also increases locally, the force induced by air on waves even with small amplitudes is still higher; hence the surface stripping phenomena occurs more predominant at higher pressures.

Also since at high pressures surface stripping occurs on waves with smaller amplitudes than at lower pressures, the clusters carry little mass and hence produce smaller droplets (the effect of surface stripping on the variation of SMD distributions is explained in Appendix C). This is crucial to understand the effect of thickness of the liquid sheet at the prefilmer edge on the atomisation and dispersion characteristics of the spray.

3.2 LIQUID SHEET BREAKUP IN A NONPREFILMING AIRBLAST ATOMISER

It is generally reported in the literature, Stapper et al. [80], that there exist two types of breakup mechanisms, viz. cellular breakup and stretched streamwise breakup in case of nonprefilming airblast atomisers. The cellular breakup mechanism occurs at higher relative velocity between air and liquid. Cellular structures form between the spanwise waves and streamwise waves, and at limiting conditions the spanwise waves separate into individual spanwise ligaments. The stretched streamwise breakup mechanism occurs at low liquid velocities by forming stretched streamwise ligaments which break subsequently. The classification of two breakup mechanisms observed was based on randomly acquired images at specific operating condition. However in the present study it is observed that both mechanisms are limiting cases of a generic breakup of liquid sheets. In the present work, a high speed flow visualisation has been performed to assess the validity of the mechanisms and as a result, the breakup mechanism is now reasonably well understood.

A free liquid surface is prone to instabilities. As explained above, the small amplitude waves formed on the liquid sheet propagate along the flow direction. The small amplitude waves are termed as spanwise waves. These waves accelerate as they propagate. The distance between the spanwise waves increases as they propagate. This causes thinning of the liquid sheet between two wave fronts. The surface tension forces tend to converge (accumulate) the liquid sheet, forming ligament like elements, which are termed here as streamwise structures. The details of formation of spanwise and streamwise waves are explained in the schematic of Figure 3.6.

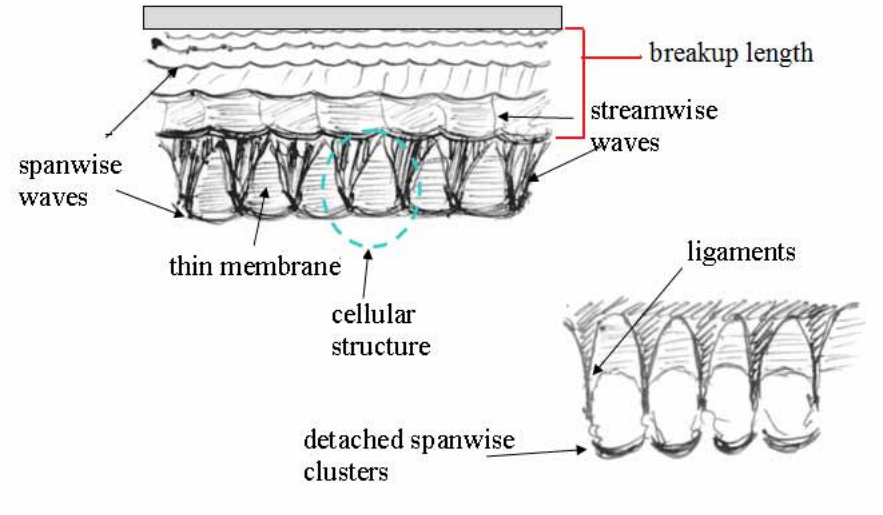

Fig. 3-6 Formation of spanwise and streamwise waves

When the distance between the upstream and the immediate downstream spanwise wave front reaches a critical stage, the distance between the streamwise waves also reaches a limiting value. This produces a cellular structure with a thin membrane between the streamwise waves. Subsequently, the thin membrane breaks up forming individual ligaments. The term ligaments are used here when the membranes between the streamwise waves break. The adjacent ligaments are joined by spanwise waves. These spanwise waves also break between the ligaments forming spanwise clusters. The streamwise ligaments which are attached to the following wave front stretch and also break into clusters. The breakup mechanism explained here applies for all the conditions tested. Figure 3.7 shows the liquid sheet breakup for a nonprefilming atomiser at We = 32 (P_a = 2 bar, V_a = 30 m/s). As can be observed from the images, the spanwise waves propagate forming ligaments and cellular structures. At critical conditions, as it can be observed in image 003, the spanwise waves break, forming clusters at the ends of the ligaments. Also it can be observed that the streamwise ligaments stretch and break (images 006-007) which is a subsequent event as explained above. This process according to Stapper et al. was termed ‘stretched ligament breakup’. However one can also observe the process associated with the cellular breakup mechanism. Hence it can be concluded that the breakup of flat liquid sheet is always similar. At the operating conditions mentioned in Figure 3.7, the spanwise wave speed is ~3-4 m/s. However depending on experimental conditions the length scales vary.

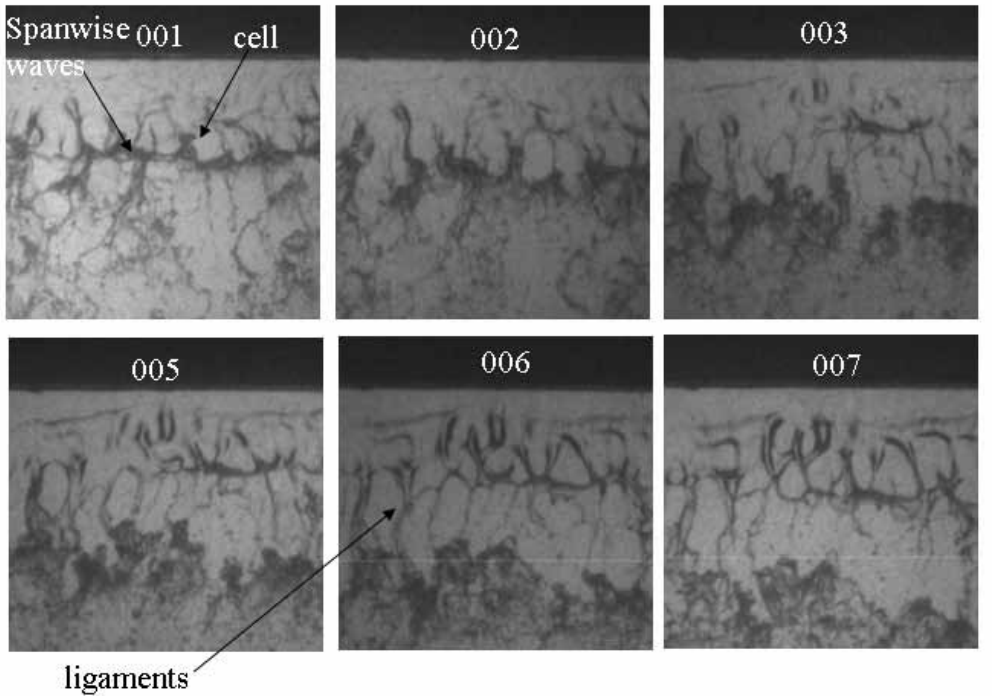

Fig. 3-7 Liquid sheet breakup of a nonprefilming atomiser
P_a = 2 bar V_a = 30 m/s V_l = 1.5 m/s

As shown in Figure 3.8, at higher operating conditions, by increasing the aerodynamic forces, the liquid sheet tends to break in a similar fashion. The circles marked in images 001-004 indicate that the spanwise waves accelerate causing ligaments to stretch and at critical conditions they break up forming clusters. But, the length scales of spanwise waves and ligaments are smaller and near to the atomiser slit. The spacing between the spanwise waves is less and the ligament dimensions are small. At these conditions the breakup is more chaotic. This is due to many factors like the turbulence level in the air flow, the geometric parameters of the atomiser etc.

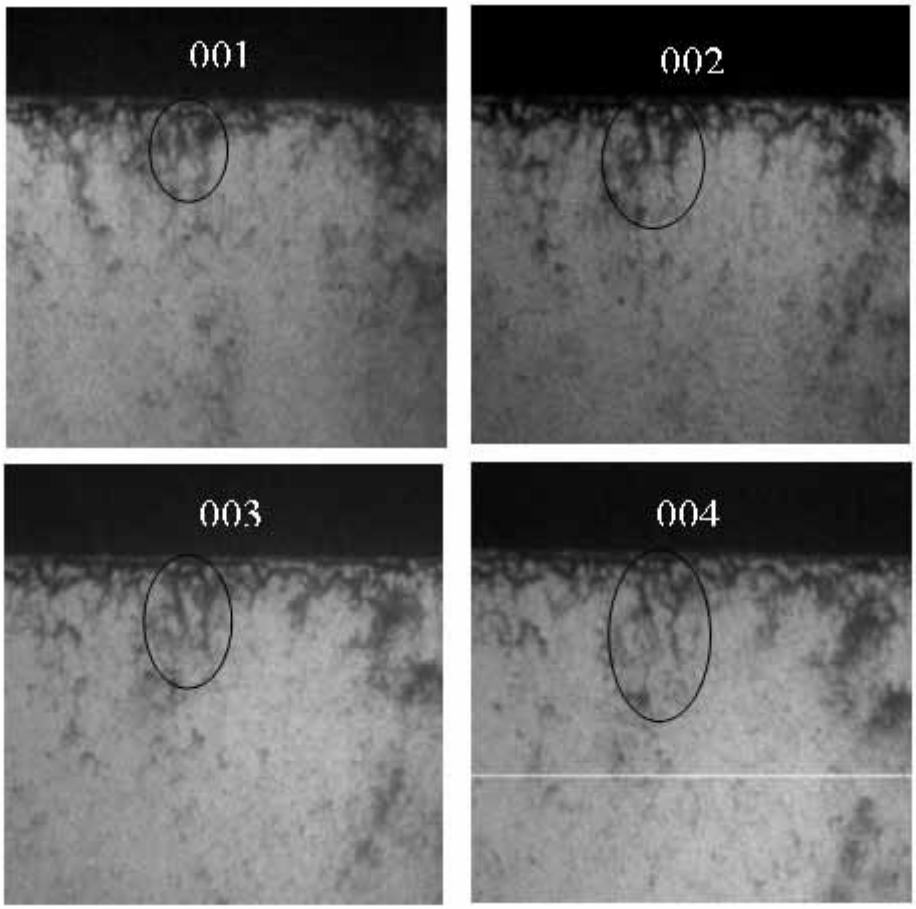

Fig. 3-8 Liquid sheet breakup of a nonprefilming atomiser
P_a = 2 bar V_a = 90 m/s V_l = 1.5 m/s

It is also observed that the small amplitude waves propagate at high speeds and merge with the wave ahead. As can be observed in Figure 3.9, in the circles marked in black, a small trapped bubble like structure between two waves is suppressed due to the preceding wave merging with the wave ahead, images 1-4 top row. As can be seen in the images 5-8, the merged wave propagates ahead and again one can observe formation of another small amplitude wave. However, the images are acquired only from one direction and hence the nature of the waves is not fully clear.

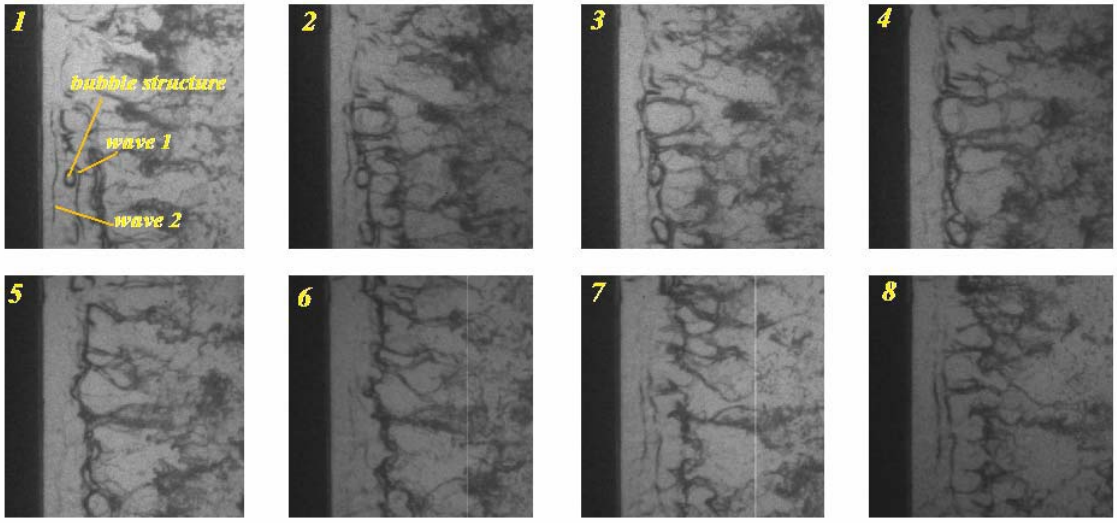

Fig. 3-9 Propagation of small amplitude waves
P_a = 2 bar V_a = 30m/s V_l = 1.5 m/s

3.3 INFLUENCE OF WEBER NUMBER ON PRIMARY BREAKUP

Qualitative comparison of liquid sheet breakup from the instantaneous images is made at constant Weber number by varying static pressure and air velocity to observe whether the Weber number can be considered as a proper nondimensional number for analysing the primary breakup of liquid sheets. Figure 3.10 and 3.11 show the effect of the Weber number for the nonprefilming and prefilming atomiser. As can be observed, at a constant Weber number, by varying the static pressure and air velocity, the breakup behaviour of the liquid sheet is similar for the nonprefilming atomiser, indicating that Weber number can be used for evaluating the primary breakup of liquid sheets. However, it has to be noted that the variation of Weber number in the present experimental studies is obtained by varying the momentum flux of air. Therefore, the breakup length or primary atomisation scales also to momentum flux of air. Prefilming atomiser shows similar trends with respect to variation of static pressure at constant Weber number.

The effect of static pressure, at constant air velocity, on the breakup phenomena can be observed for We = 56 & 167 and at We = 190 & 253 for nonprefilming atomiser. The images show that the static pressure has appreciable influence on the primary atomisation of liquid sheet. This is in-line with results obtained by Lefebvre [47] for similar atomiser design where it was reported that the static pressure has effect on the primary breakup length if the coflowing air stream are parallel to the surface of the liquid sheet. The static pressure has also similar effect in prefilming atomisers, Figure 3.11. The effect of static pressure can be observed for We = 127 & 253 and at We = 285

& 855. The effect of Weber number on ligaments spacing and breakup length is explained in Section 3.6.

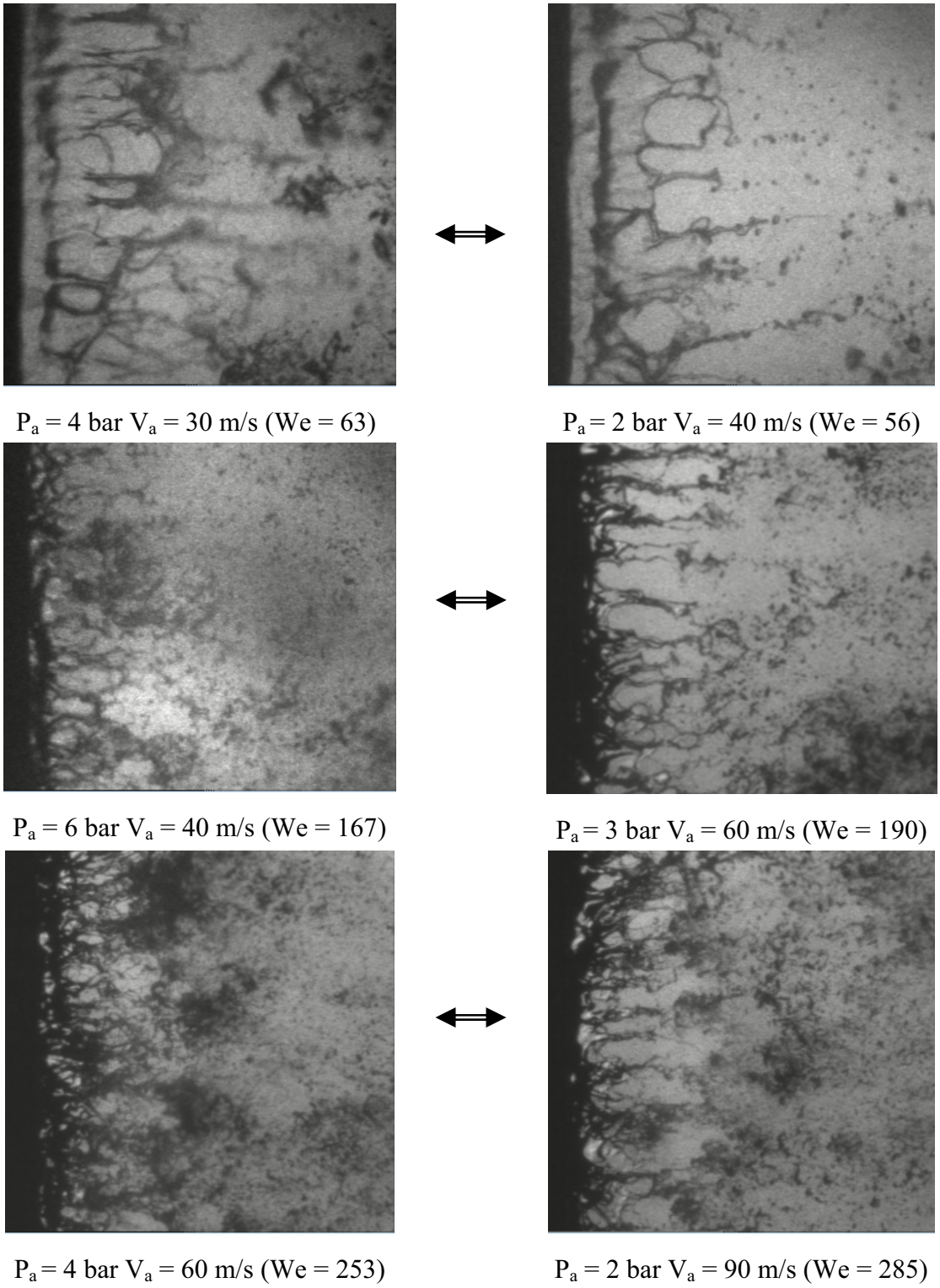

Fig. 3-10 Effect of Weber number on sheet breakup for the nonprefilming atomiser

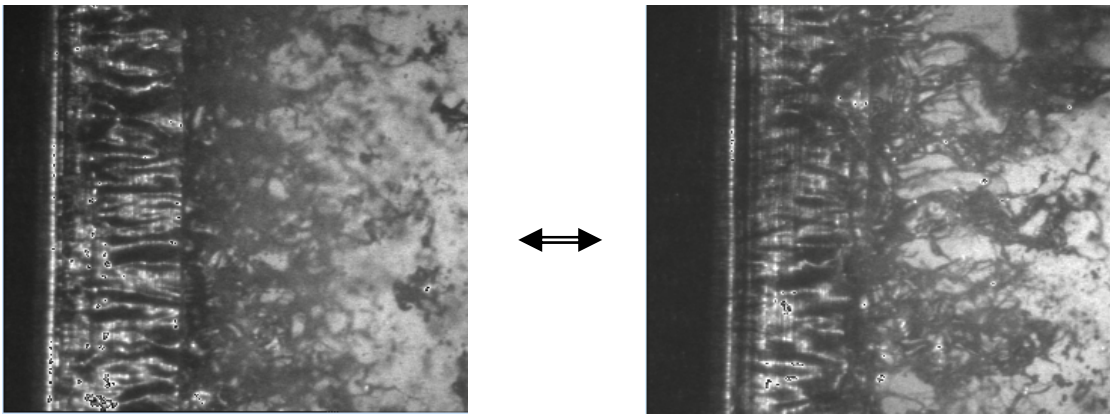

P_a = 6 bar V_a = 30 m/s (We = 95) P_a = 3 bar V_a = 40 m/s (We = 84)

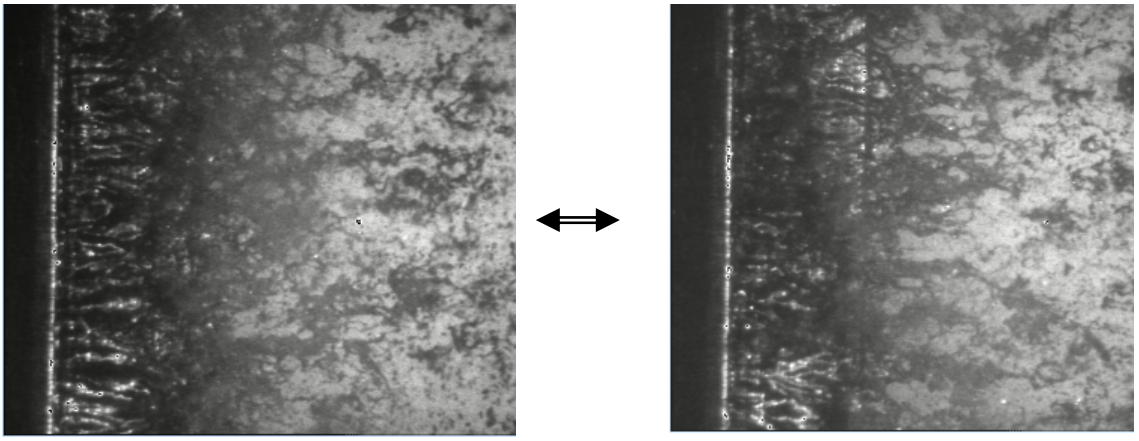

P_a = 4 bar V_a = 60 m/s (We = 253) P_a = 2 bar V_a = 90 m/s (We = 285)

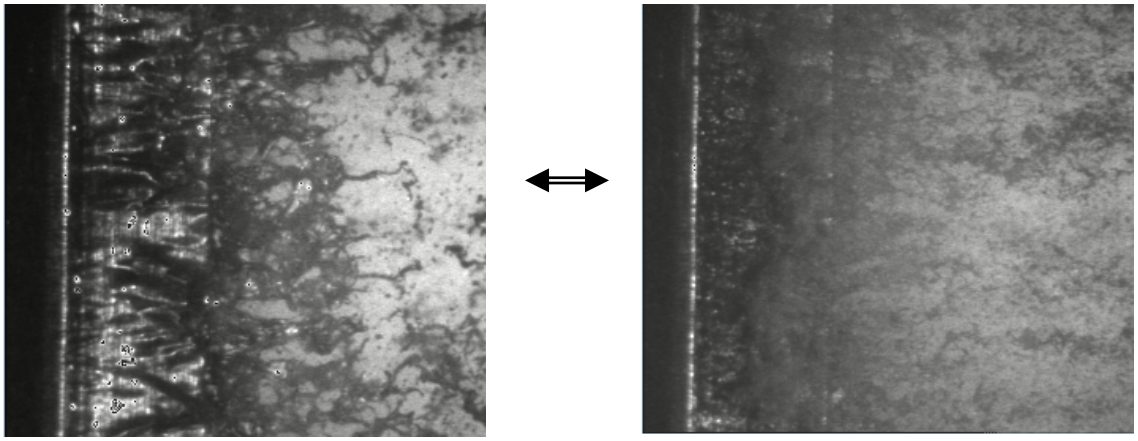

P_a = 2 bar V_a = 60 m/s (We = 127) P_a = 6 bar V_a = 90 m/s (We = 855

Fig. 3-11 Effect of Weber number of sheet breakup for the prefilming atomiser

3.4 REGIMES OF SHEET DISINTEGRATION IN THE PREFILMING ATOMISER

In general, the liquid coming out of the atomiser slit spreads into a thin sheet. For low Weber number and high liquid velocities the liquid sheet moves intact as a thick sheet over the prefilming surface. Figure 3.12, at We = 32 (P_a = 2 bar, V_a = 30 m/s), shows the spread of the liquid sheet. If the liquid sheet is intact till the end of the prefilmer edge, the disintegration of liquid sheet is similar to the liquid sheet disintegration without a prefilmer, except periodic thickening and thinning of the liquid sheet at the prefilmer edge. The effect of it is explained in Section 3.7. As the Weber number is increased, either by increasing the ambient pressure or by increasing the air velocity, waves in the stream wise direction are visible as shown in Figure 3.6, We = 85 (P_a = 3 bar, V_a = 40 m/s). As the Weber number is further increased, beyond 100, the surface of the liquid sheet starts shearing off due to the high aerodynamic pressure acting on the liquid surface. As can be seen in Figure 3.12, We = 253 (P_a = 4 bar, V_a = 60 m/s), the presence of burst of liquid surface indicates stripping of the liquid surface at the prefilmer edge. These kinds of images were observed intermittently in the set of 100 images acquired for a certain operating condition over a range of Weber number from 100-380. This range can be considered as a transition region from the wavy sheet break-up to the surface stripping type of break-up of the liquid sheet on the prefilming surface. As the Weber number increases, the phenomenon of surface stripping increases. However there exists a thin liquid sheet over the prefilming surface, see Section 3.9. This is observed in some of the images acquired with the transparent atomiser. Beyond We = 380 (P_a = 6 bar, V_a = 60 m/s), only surface stripping is observed and it is dominant factor in causing liquid mass to eject from the liquid surface.

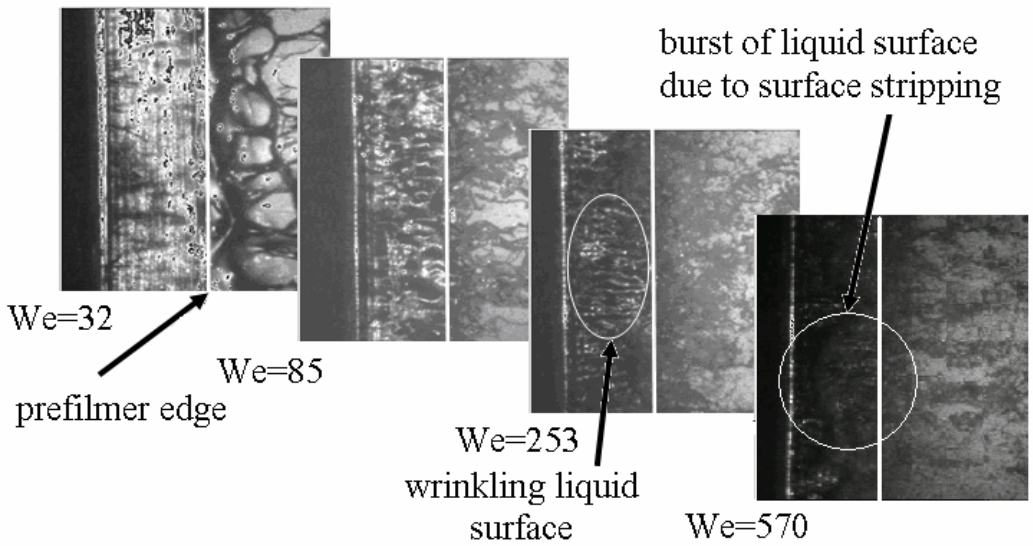

Fig. 3-12 Effect of Weber number on sheet disintegration process

To categorise the regimes of breakup in the present study, the images are classified based on visual observation for all the operating conditions tested and represented as probability of occurrence of surface stripping. Table 3.1 shows for the probability of occurrence at various operating conditions. The table shows that air velocity and pressure have a significant effect on the surface stripping phenomenon. For P_a = 6 bar it is usual to see some degree of surface stripping and for air velocities beyond 60 m/s, the surface stripping is most often visible.

V_l = 0.5 m/s	**2 bar**	**3 bar**	**4 bar**	**6 bar**
30 m/s	0	0	0	0
40 m/s	0	0	0.5	0.75
60 m/s	0	0.5	0.75	0.75
90 m/s	0.5	0.5	0.75	1
V_l = 1 m/s	**2 bar**	**3 bar**	**4 bar**	**6 bar**
30 m/s	0	0	0	0
40 m/s	0	0	0.5	0.75
60 m/s	0	0.5	0.75	1
90 m/s	0.5	0.5	1	1
V_l = 1.5 m/s	**2 bar**	**3 bar**	**4 bar**	**6 bar**
30 m/s	0	0	0	0
40 m/s	0	0	0.5	0.75
60 m/s	0	0.5	0.75	1
90 m/s	0.5	0.75	1	1

Table 3-1 Probability of occurrence of surface stripping

Figure 3.13 shows the effect of Weber number on the liquid sheet break-up mechanism. In the present experimental studies the liquid velocity could not be varied

significantly. As such, for low Weber numbers the momentum flux ratios tested are also very low. Nevertheless, it can be observed from the graph that for Weber numbers beyond 380, the effect of momentum flux ratio between the air and liquid plays little role compared to aerodynamic forces and surface stripping is more dominant.

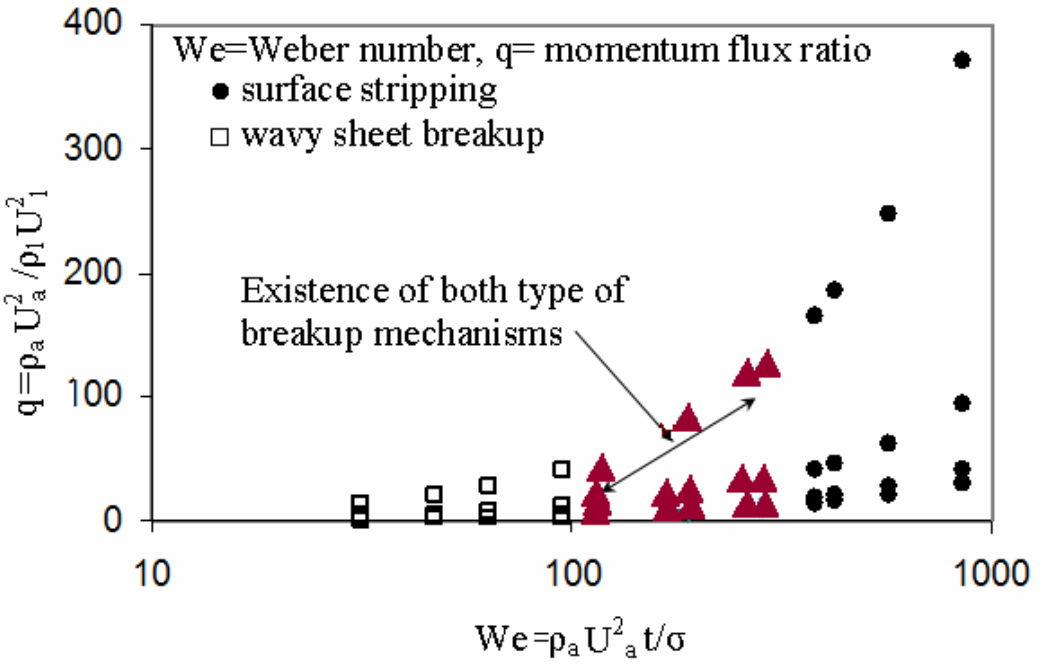

Fig. 3-13 Effect of Weber number on breakup mechanism

3.5 LIQUID SHEET OSCILLATIONS

Nonprefilming atomiser

In case of the nonprefilming atomiser the coflowing air streams act simultaneously on the liquid sheet that is emerging from the atomiser slit. Side view images revealed the oscillatory behaviour of the liquid sheet. Figure 3.14 shows sequential images of liquid sheet oscillations at two typical operating conditions. At low operating conditions at We = 32 (P_a = 2 bar, V_a = 30 m/s), as shown in Figure 3.14(a), the oscillation of the liquid sheet is very clear. It appears the liquid sheet is oscillating in sinusoidal fashion. In the literature, Hagerty and Shea [32], this is attributed to the instabilities of the liquid sheet. It is also observed that the liquid sheet is disintegrating downstream of the atomiser, as can be observed in Figure 3. 14(a) image 2-4. The disintegrated liquid sheet oscillates similar to the liquid sheet that is intact. At higher operating conditions at We = 128 (P_a = 2 bar, V_a = 60 m/s), Figure 3.14(b), the liquid sheet disintegrates much closer to atomiser. But still the liquid phase oscillates in

sinusoidal fashion. The reason is due to the interaction of liquid film with the boundary layers that are formed on both sides of the atomiser. The vorticity on both sides have opposite sign and the strength depends on the local aerodynamic characteristics of air streams as shown in schematic in Figure 3.15. The design of atomiser is similar to an NACA 0014 airfoil. The wake behind the atomiser is similar to the wake behind the airfoil. The presence of coherent structures and vortices behind an airfoil is reported in the literature [87]. The formation of vortices depends on the characteristics of an airfoil, boundary layer, trailing edge, and Reynolds number of the flow. This indicates that the vorticity generated on both sides of the atomiser plays a key role on the oscillations of the liquid sheet.

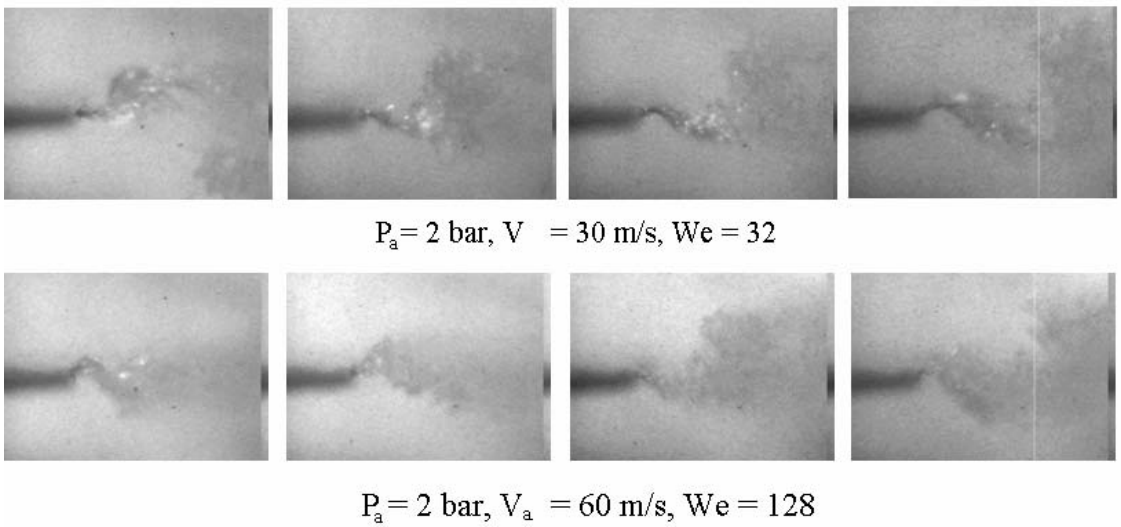

Fig. 3-14 Liquid sheet oscillations in nonprefilming atomiser

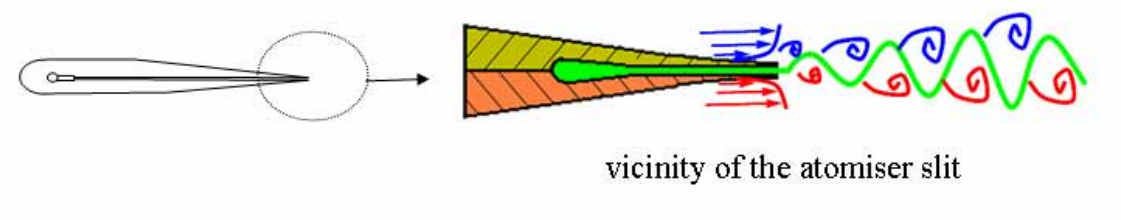

Fig. 3-15 Nonprefilming atomiser

The liquid sheet emerging from the atomiser slit is thin but intact and hence it behaves as a thin flexible membrane. The interaction of the vorticity on both sides of the atomiser in the wake is now through the liquid sheet. Since the liquid sheet is thin and flexible, it starts fluttering like a flag in an air stream. The liquid sheet oscillates according to the fluctuations of the aerodynamic forces. It is known that the vortex shedding behind a cylinder induces unsteady forces in the flow downstream and on the

cylinder. Several methods are used to dampen the vibrations. In typical cases solid splitter plates are used behind the cylinder. It was observed that even far downstream of the splitter plates, the vortices tend to exist indicating that the generated vorticity propagates. This is equivalent to the liquid sheet in between vortices/vorticity on both sides. However the liquid film here is a flexible membrane and reacts to the vortex induced forces/vibrations in a nonlinear fashion. As all practical atomisers have a certain thickness at the edge, the boundary layer detaches at the edge of the atomiser and reattach again on the liquid sheet. This happens in the fashion of a Von Karman vortex street, inducing alternating vorticity on both sides of the liquid sheet similar to the flow behind cylinders [87] producing asymmetric vortex street. In Figure 3.14, the wave nature of the flow during and after liquid sheet breakup gives an indication of the presence of Karman Vortex Street. From the high speed sequential images, the frequency of the liquid sheet is calculated and related to Strouhal number. Strouhal number is calculated based on air velocity and the thickness of the atomiser. Table 3.2 gives the Strouhal number at various operating conditions. The Strouhal number is nearly constant of approximately 0.18. The interframing time between images is quite large and hence the frequency measurements have to be considered as a mere approximation. Nevertheless, a constant Strouhal number indicates the sheet oscillations are due to fluid dynamics of the wake of the atomiser.

Pressure (bar)	**Velocity (m/s)**	**Strouhal number (ST)**
2	30	0.196
2	40	0.176
2	60	0.177

Table 3-2 Strouhal number at various operating conditions

Prefilming atomisation

In case of the prefilming atomiser, the liquid sheet oscillations are observed only at low Weber numbers when there is no surface stripping and the liquid sheet is intact till the edge of the prefilming surface. Figure 3.16(a) shows the oscillation of liquid sheet after the prefilming surface.

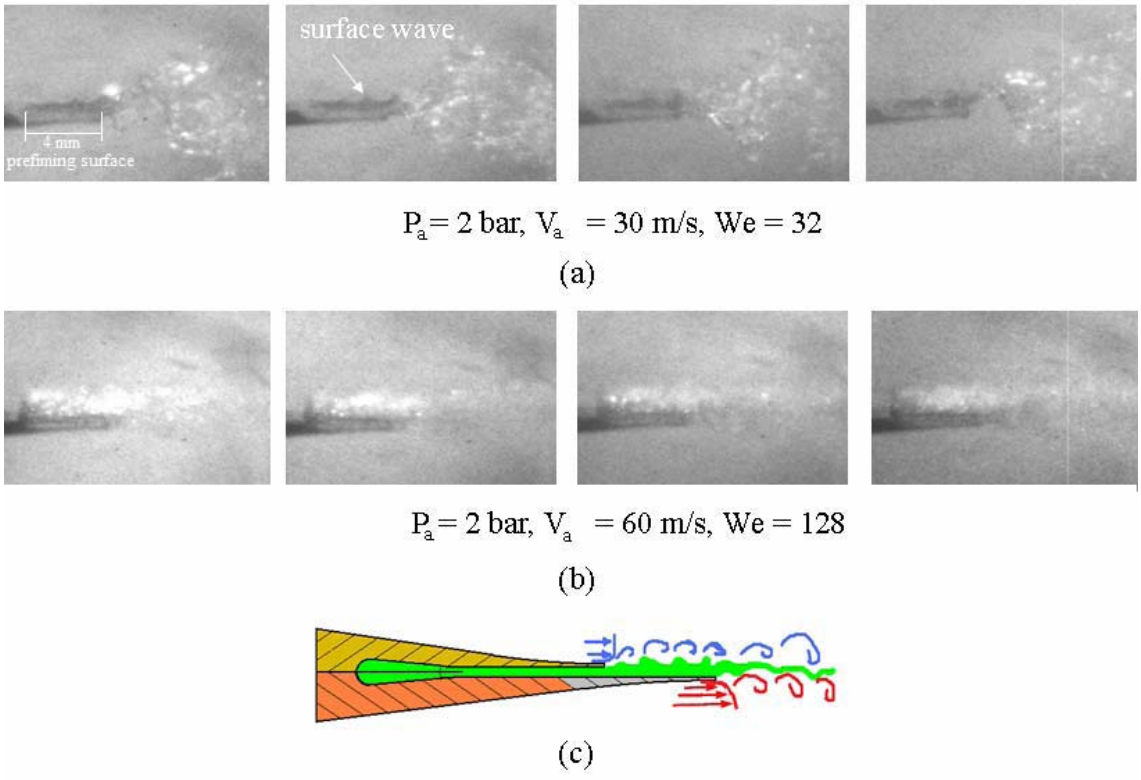

Fig. 3-16 Liquid sheet oscillations in prefilming atomiser

The propagation of surface waves on the surface of the liquid is clearly visible. However, the oscillations are not dominant as in the case of the nonprefilming atomiser. At higher Weber numbers, as shown in Figure 3.16(b), the oscillations of the liquid sheet are suppressed. Also, a bright area on top of the prefilming surface indicates initiation of surface stripping on the surface of the liquid sheet. The propagation of surface waves and surface stripping significantly affect the vorticity generated at the surface of the atomiser. As shown in the schematic, of Figure 3.16(c), the degree of vorticity on both sides of the atomiser is not equally opposite in sign to induce oscillation of the liquid sheet, because of the phase difference between the up-and downside vorticity that is created by the prefilmer length. This phase depends on the scale of the vorticity which in turn depends on the operating conditions, making it unlikely to be either 0° or 180°.

3.6 BREAKUP LENGTH OF LIQUID SHEET AND LIGAMENT SPACING

Several key parameters like breakup length, ligament spacing, and sheet thickness variation during breakup have to be known in order to simulate the breakup of liquid sheets. Often these parameters are difficult to measure. An Effort is made to quantify the effect of operating conditions on the breakup length of the liquid sheet and ligament spacing by image processing.

Breakup length of the liquid sheet

A total of 25 instantaneous images are averaged and breakup length is measured manually from the averaged images. The breakup of the liquid sheet for nonprefilming atomiser is measured as the distance from the atomiser slit to the point of breakup into individual ligaments, as explained in an earlier section. For the prefilming atomiser the breakup length is the length from the atomiser slit to the point where the individual ligaments are formed after the prefilming surface. Figure 3.17 shows the effect of static pressure and Weber number on the primary breakup length for nonprefilming and 2 mm prefilming atomiser. In case of prefilming atomiser, as shown in Figure 3.17(a) the sheet breakup length is nearly constant as the Weber number is increased. This is because the liquid sheet is carried until the edge of the prefilming surface before the liquid sheet breaks into individual ligaments. Since the prefilming surface in this case is 2 mm, the liquid sheet breaks after ~0.5 mm from the prefilming surface. In case of nonprefilming atomiser as shown in Figure 3.17(b, c), the liquid sheet break up has asymptotic behaviour as the Weber number or static pressure is increased. At Weber number > 150, the breakup length reaches ~0.5 mm which is similar to the prefilming atomiser. The effect of air velocity is very significant in terms of the break-up length. As the air velocity increases, the sheet break-up appears just downstream of the slot. Independent quantification of the effect of air velocity is very difficult to perform with accuracy from the images for the operating conditions tested.

Ligament spacing

It is observed from images that there is an effect of operating conditions on spacing between ligaments. Berthoumieu [7] quantified spacing between ligaments by image processing. In the present study, a similar effort has been carried out to measure the spacing between ligaments. Figure 3.18 shows the formation of ligaments for a liquid sheet emerging from nonprefilming airblast atomiser with sheet thickness of 300μm. The image processing is performed by counting the number of ligaments in one image area and dividing by the width of the image to obtain ligament spacing. This gives average ligament spacing in one image in the pixels. Image Processing is performed on approximately 20 images for one operating condition and the average spacing between ligaments is used for further analysis. Typically, ligament spacing between approximately 300 ligaments is counted for obtaining an average ligament spacing for one operating condition. It is observed that spacing between ligaments decreases as air velocity and pressure are increased. Figure 3.19 shows the effect of momentum flux ratio on ligament spacing. Momentum flux is defined as the ratio of momentum flux of air to fuel. It is given by $q = \frac{\rho_a U_a^2}{\rho_l U_l^2}$, where q is the momentum flux ratio.

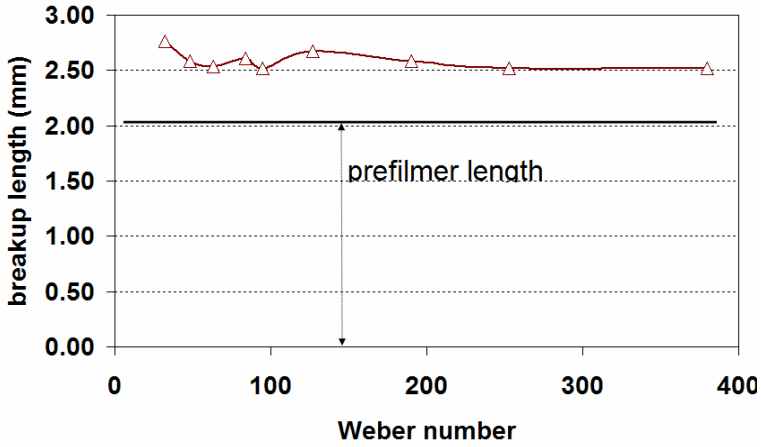

(a) 2 mm prefilming atomiser

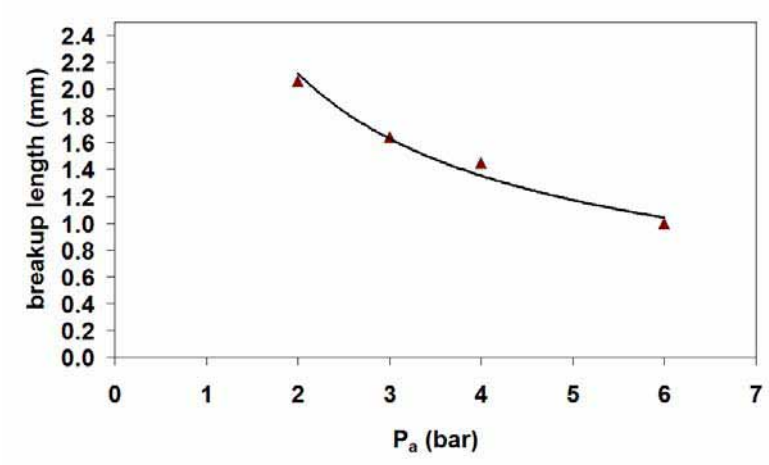

(b) effect of pressure in nonprefilming atomiser

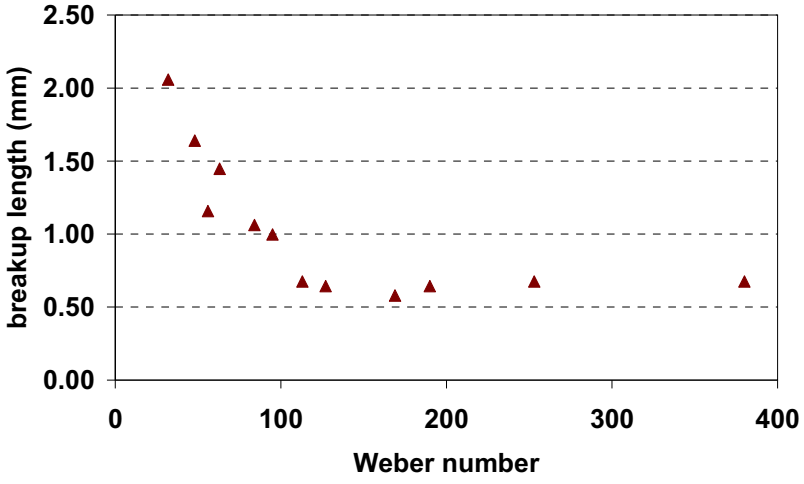

(c) nonprefilming atomiser

Fig. 3-17 Effect of pressure and Weber number on the primary breakup length

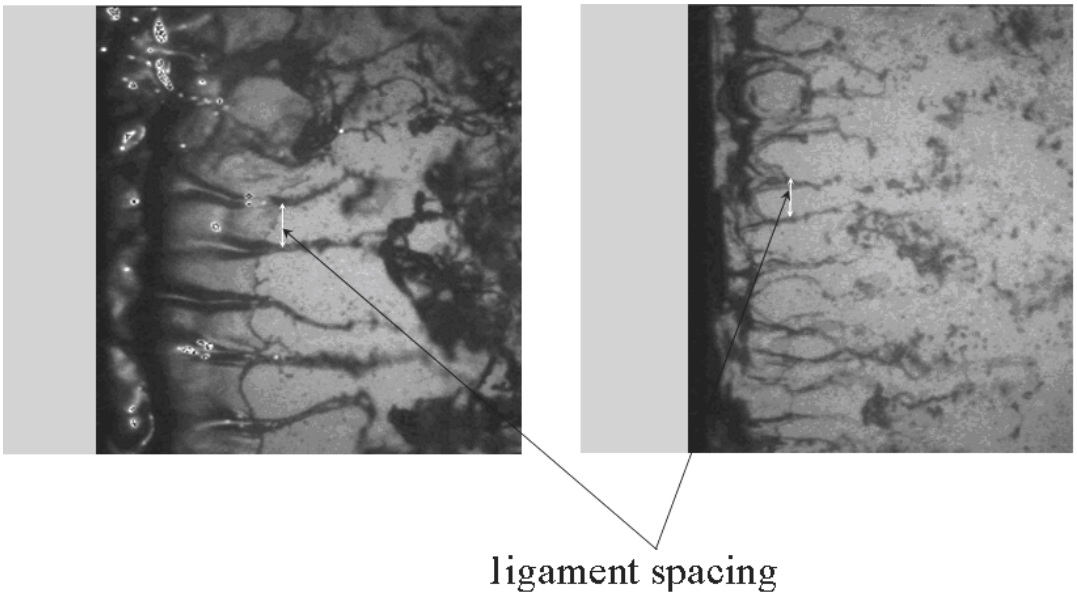

Fig. 3-18 Spacing between ligaments (nonprefilming atomiser, t_l = 300 μm)

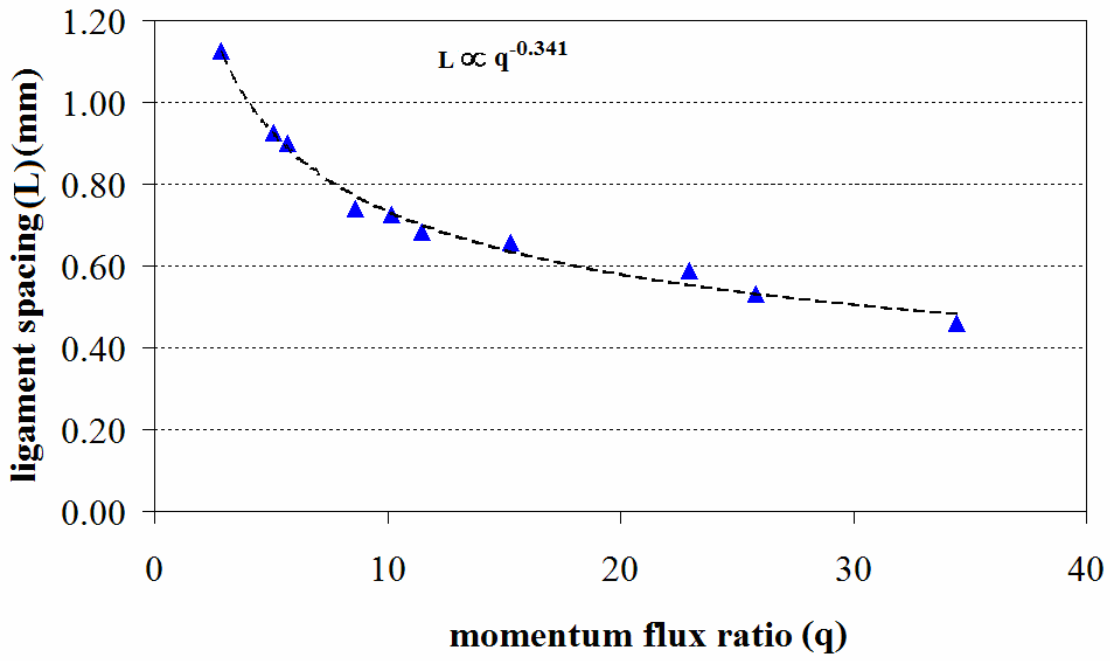

Fig. 3-19 Effect of momentum flux ratio on ligament spacing

It is clear that the spacing between ligaments decreases as the ratio of momentum flux increases. It has to be noted that the momentum flux of liquid is kept constant during all operating conditions unless explicitly stated. Hence, the graph actually gives the effect of momentum flux of air on ligament spacing. The graph indicates that the spacing between ligaments and momentum flux variation follows a power law by a factor of -0.341. The results seem to be in conformity with Berthoumieu [7] & Lozano [51], in that the ligament spacing decreases with an increase in air

velocity. An extrapolation of a result from an operating condition and comparison with Berthoumieu show that momentum flux ratio is indeed the governing factor for spacing between ligaments.

3.7 SHEET THICKNESS MEASUREMENTS

For atomisation models dealing with prefilming atomisers, it is essential to know the temporal thickness and waviness of the liquid sheet and the amount of mass stripped from the liquid surface. These parameters are dominant factors for evaporation of the liquid fuel.

Measurement of film thickness at realistic conditions is a difficult task mainly due to the small thickness of the liquid film. Most measurements techniques available in the literature [38], for measuring liquid film thickness expect the liquid surface to have minimum curvature and the thickness of the liquid sheet >1000 μm. In the present case the surface of the liquid film is corrugated as explained in earlier sections. The thickness of the liquid sheet is 300 μm at the entrance of the atomiser slit. Also, the liquid sheet thickness has to be measured in the middle of the span of the liquid sheet for accurate measurements. The span of the liquid sheet is 12 mm and hence creates difficulties for optical access for the lack of depth-of-field with the required magnification when measuring from the side view. In the present measurements, the liquid sheet thickness is measured at the edge of the liquid sheet. Since there is always spillover at the edge of the liquid sheet, the sheet thickness measured at the side is always underestimated.

The side view images acquired during background shadowgraphy imaging are used to measure the liquid sheet thickness. As the liquid sheet is wavy and propagating, the amplitude of the wave reaches a maximum. Also it is observed that a minimum thickness of the liquid sheet formed on the prefilming surface is unaffected by the aerodynamic forces. Hence, the liquid sheet thickness is characterised by the maximum and minimum thickness it can achieve for an operating condition, as shown in Fig. 3.20. The maximum and minimum is obtained by manually measuring the length of the maximum and minimum from an image. The maximum attained in each 8 images are averaged to obtain an average maximum a liquid film can achieve at an operating condition. A similar procedure is used to measure the average minimum a liquid film can achieve at an operating condition.

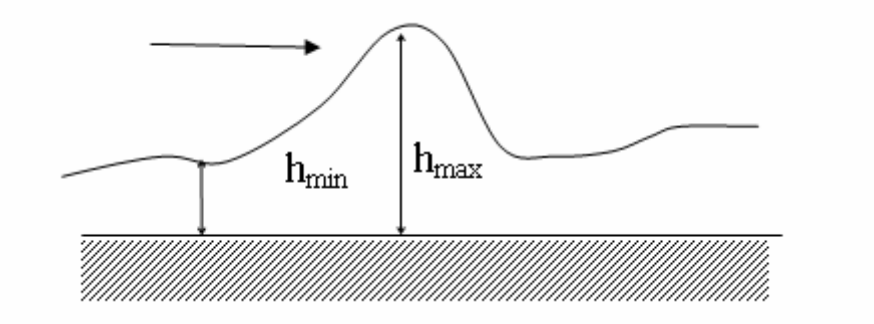

Fig. 3-20 Maximum and minimum of liquid sheet

Figure 3.21(a) shows a typical propagation of a liquid sheet on the prefilming surface at We = 32 (P_a = 2 bar, V_a = 30 m/s). It can be observed that the liquid sheet has maximum and minimum amplitudes. The measured average maximum amplitude is ~ 600 µm which is almost twice the actual film thickness at the atomiser slit. The minimum amplitude is ~ 100 µm. Since the liquid sheet behaves like a surface wave, the increase in amplitude has to be balanced by a decrease in amplitude to preserve mass balance.

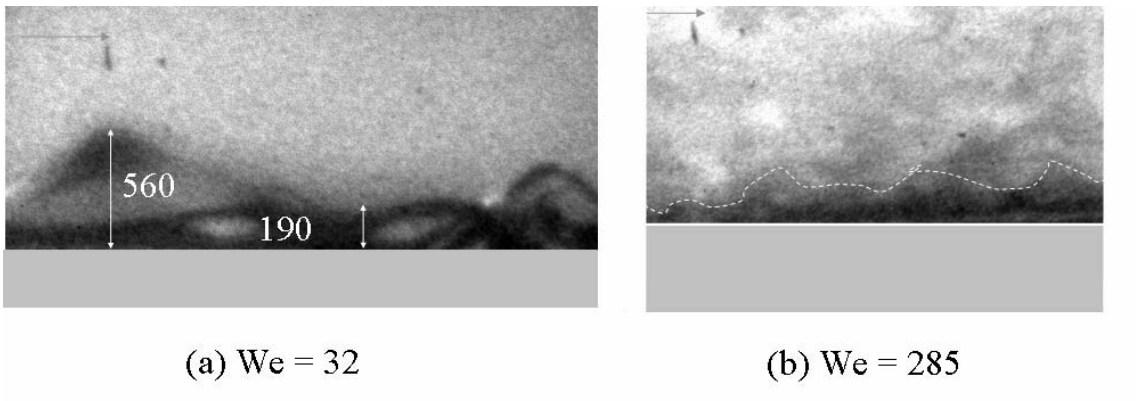

Fig. 3-21 Maximum and minimum amplitude of the liquid sheet

As the Weber number increases, due to surface stripping, a defined amount of mass is lost and the thickness of the liquid sheet decreases. Hence, the maximum amplitude the liquid sheet can attain also decreases. Fig 3.21(b) shows the typical wavy nature of the liquid sheet at We = 285 (P_a = 2 bar, V_a = 90 m/s). The dotted line indicates the liquid film. The dark regions above the dotted line indicate the mass ejected due to surface stripping. The average maximum amplitude at this operating condition is ~ 378 µm and the average minimum amplitude is ~ 90 µm. Also at this operating condition calculated from images, liquid lumps stripped from the surface are in the order of ~ 300 µm in diameter. The amount of mass that is stripped from the surface can be approximated accordingly. Figure 3.22 shows the variation of sheet thickness on prefilming surface at various operating conditions. The propagation of

surface waves on the prefilming surface can be observed at We=32. The interaction of the surface wave with the prefilmer edge can also be observed. As the Weber number increases the surface stripping becomes more predominant and the liquid sheet thickness decreases along the prefilming surface.

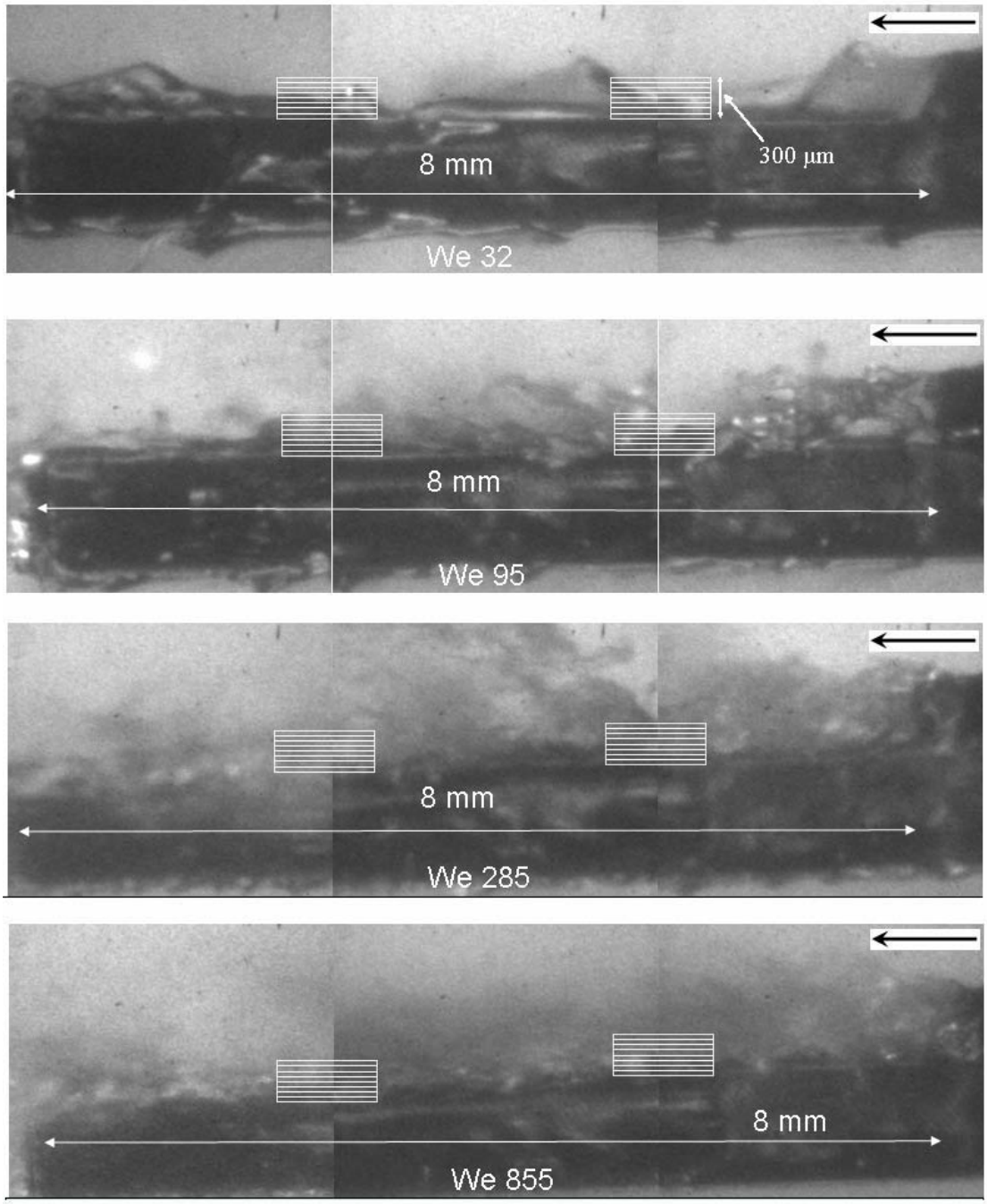

Fig. 3-22 Variation of film thickness along the prefilming

The thickness of the prefilming edge can also have an impact on breakup of the liquid sheet and the fluctuations at which the liquid phase is moving in the air stream. If

the thickness of the prefilmer edge is comparable to or thicker as the thickness of the film, then the liquid turns at the prefilmer edge as shown in Figure 3.23. This is called Coanda effect which occurs mainly due to the adhesive properties of the liquid to attach itself to the solid surface. For a considerable thickness of the prefilmer edge, the liquid actually can become stagnant at the edge till a fixed amount of mass is accumulated before the liquid breaks from the edge of the prefilmer. This can create a storage mechanism due to Coanda effect at the prefilmer edge. The storage mechanism is a function of the operating conditions. For example: it is known now that more mass is stripped from the surface of the liquid sheet at higher operating conditions and hence effectively the liquid thickness at the edge is much smaller and hence this mechanism can be more predominant at higher operating conditions. Also, if there is modulation of the air streams which in realistic operating conditions can occur due to the compressor, the fluctuations of liquid mass that is stored at the prefilmer edge can actually deliver liquid at a different frequency than the modulation frequency.

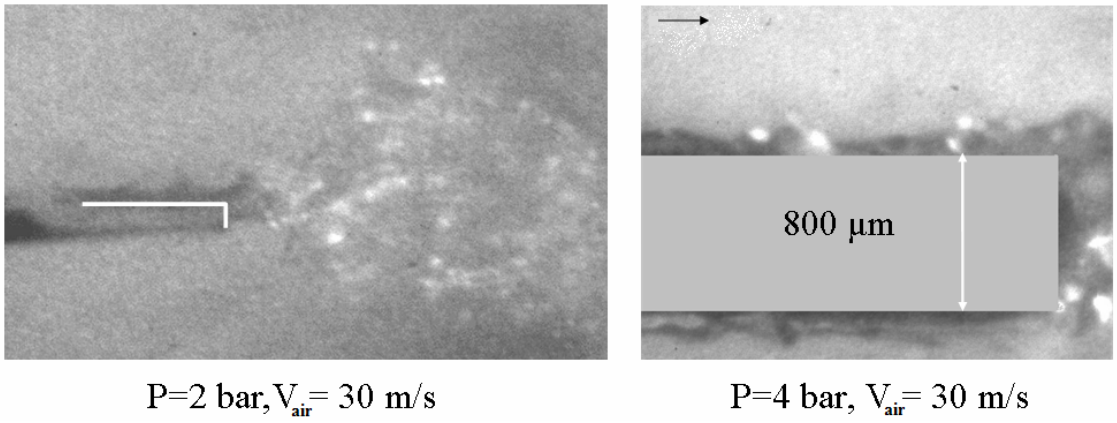

Fig. 3-23 Coanda effect at the edge of the prefilmer surface

3.8 PIV MEASUREMENTS IN THE NEAR-FIELD OF THE ATOMISER

Typically the atomisation of the liquid is complete around 10 mm downstream of the atomiser. However the spray is very dense in this region and non-spherical particles exist in this region. Attempts to obtain quantitative measurements of particle size and velocity in this region with PDA are prone to errors at realistic operating conditions. Often times the flame front in the combustor is anchored in about the same distance to the atomiser or even closer. The information on size and velocity of the particles in this near-field of the atomiser is important for the characterisation of the spray with respect to combustion. It is also important for validation of combustion codes to have information in the near-field of the atomiser.

The velocity of the particles and structures is measured by PIV for both prefilming and nonprefilming atomisers up to 25 mm downstream of the atomiser at 4 operating conditions at P_a = 2 bar, 6 bar for V_a = 30 m/s, 60 m/s. The PIV results are compared with PDA results in the same region to examine the efficacy of application of PIV technique in the near-field of the atomiser.

Figure 3.24(a) shows the propagation of the liquid sheet and breakup of the liquid sheet into ligaments and droplets for a prefilming airblast atomiser at We = 128 (P_a = 2 bar, V_a = 60 m/s). It can be observed that the liquid sheet emerges from the slit at X= 0 mm and surface waves are formed on the liquid sheet as discussed in earlier sections. The liquid sheet breaks downstream of the atomiser into ligaments until z = 5-7 mm. These ligaments break into large irregular structures which last until 15 mm downstream of the atomiser. Beyond 15 mm, the structures break into large droplets. Further downstream, secondary breakup of large droplets occurs producing smaller droplets and beyond 20 mm atomisation is considered to be complete.

A schematic of several stages of a typical breakup of liquid sheet atomisation is given in Figure 3.25. The PIV analysis on the sequential images is able to measure the velocities accurately until the formation and displacement of large droplets, Figure 3.25(d). Figure 3.24 (b) shows the velocity contours of the liquid phase obtained by averaging of 300 PIV recordings. The velocity of the surface of the liquid sheet is 3-5 m/s at this operating condition. The calculated velocity of the liquid is 1 m/s at the entrance of the atomiser slit. The calculated velocity is based on the metered flow rate. This shows that the surface of the liquid is traveling at higher velocity due to the interaction of the liquid surface with the surrounding air. This induces strong velocity gradients inside the liquid sheet at higher operating conditions. The ligaments formed due to the liquid sheet breakup travel at 5-10 m/s. The change in the colour of the contour from blue to green can be considered to be representative of the regime. The breakup of irregular structures and further breakup into large droplets leads to acceleration of the large droplets. This is represented by shift in contour colour form green to red. The large droplet attains a velocity of 20 m/s at axial distance of 20 mm from the atomiser. Beyond axial distance of 25 mm, the droplets reach the velocity of the surrounding air and attain the maximum velocity. The different shades in the contour above represent different stages of breakup mechanism. Figure 3.24 (c) shows the RMS velocity of the liquid phase. The RMS velocity is ~3 m/s until axial distance of 7 mm where there is formation of ligaments and irregular structures. Beyond axial distance of 20 mm, the RMS Velocity increases to ~ 7 m/s due large and small droplets having formed are now traveling at different velocities due to their different accelerations. In this region, the apparent turbulence is due to the different droplet size classes being unevenly accelerated as said above. Figure 3.24 (d) shows the velocity

vectors of the liquid phase. It can be observed the flow-field of the liquid phase is two dimensional.

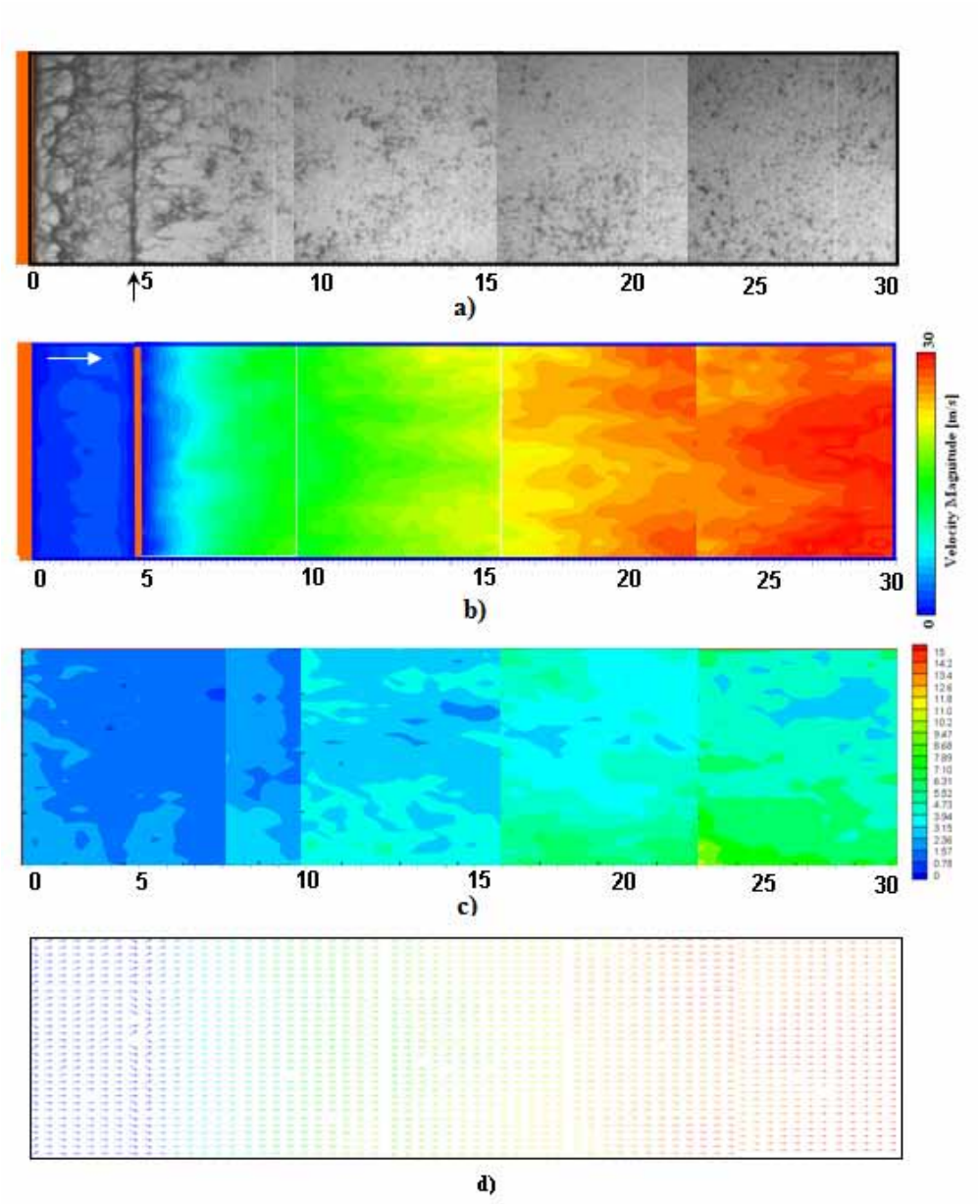

Fig. 3-24 Breakup of liquid sheet and Velocity contour plot of liquid phase at P_a = 6 bar, V_a = 30 m/s (We =128)

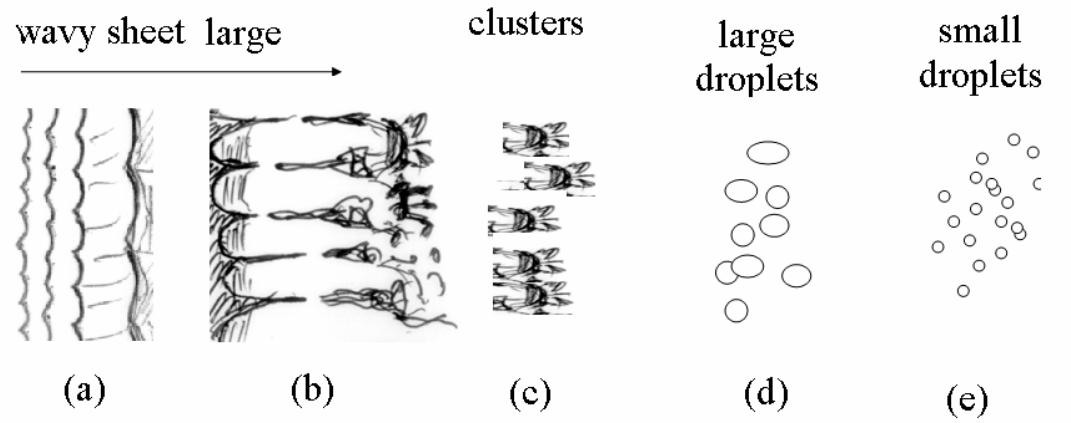

Fig. 3-25 Regimes of Liquid sheet breakup

Figure 3.26 and Figure 3.27 show the velocity of the liquid phase at various operating conditions for the 4 mm prefilming and nonprefilming airblast atomisers. For comparison, the magnitude of the velocity contours is set at 30 m/s even though at higher velocities of surrounding air, the particles accelerate and disintegrate and reach the velocity of surrounding air at much smaller length scales. As it can be observed, the velocity flow-fields for both prefilming and nonprefilming atomisers at the operating conditions with 30m/s air velocity are similar. However, it can be observed that for 60 m/s at a given axial location (z = 8–15 mm) from the atomiser, the velocity contours for the prefilming atomiser show higher magnitudes in comparison with nonprefilming atomisers indicating that the acceleration rates for the particles for both atomisers is different.

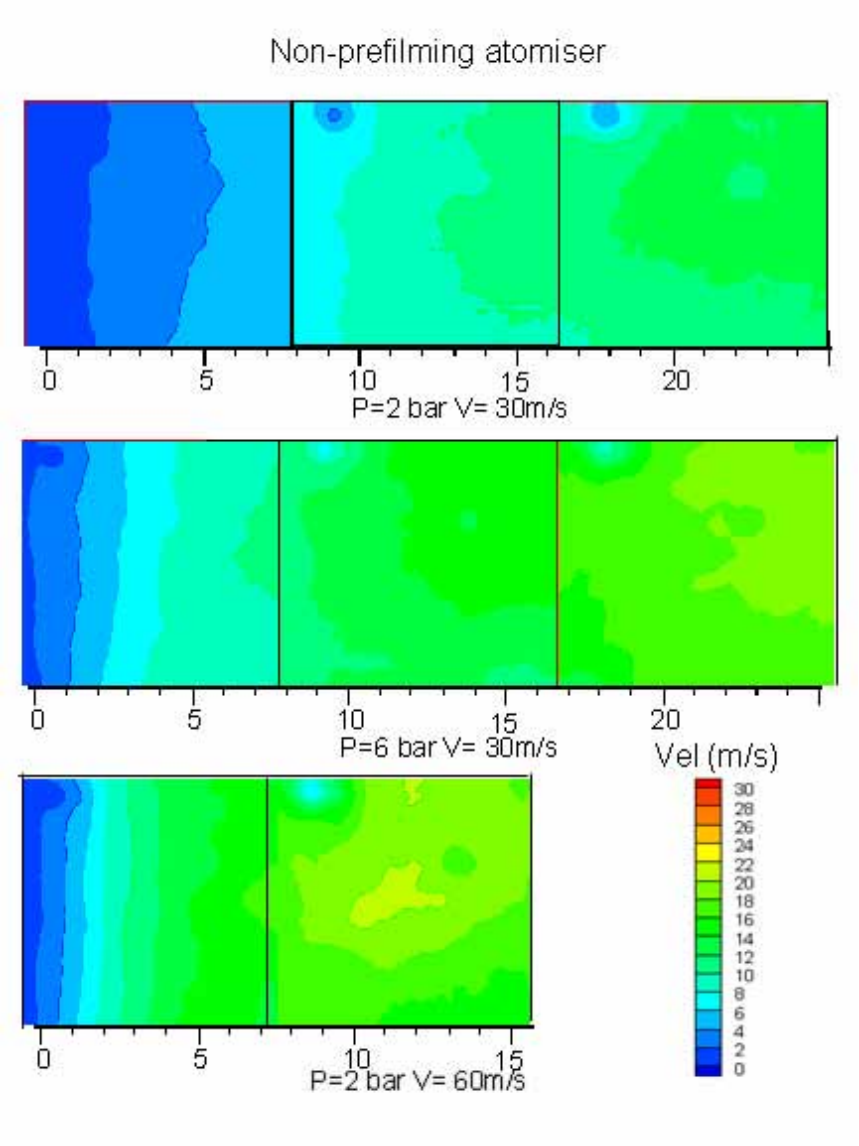

Fig. 3-26 Velocity contours of liquid phase for nonprefilming atomiser

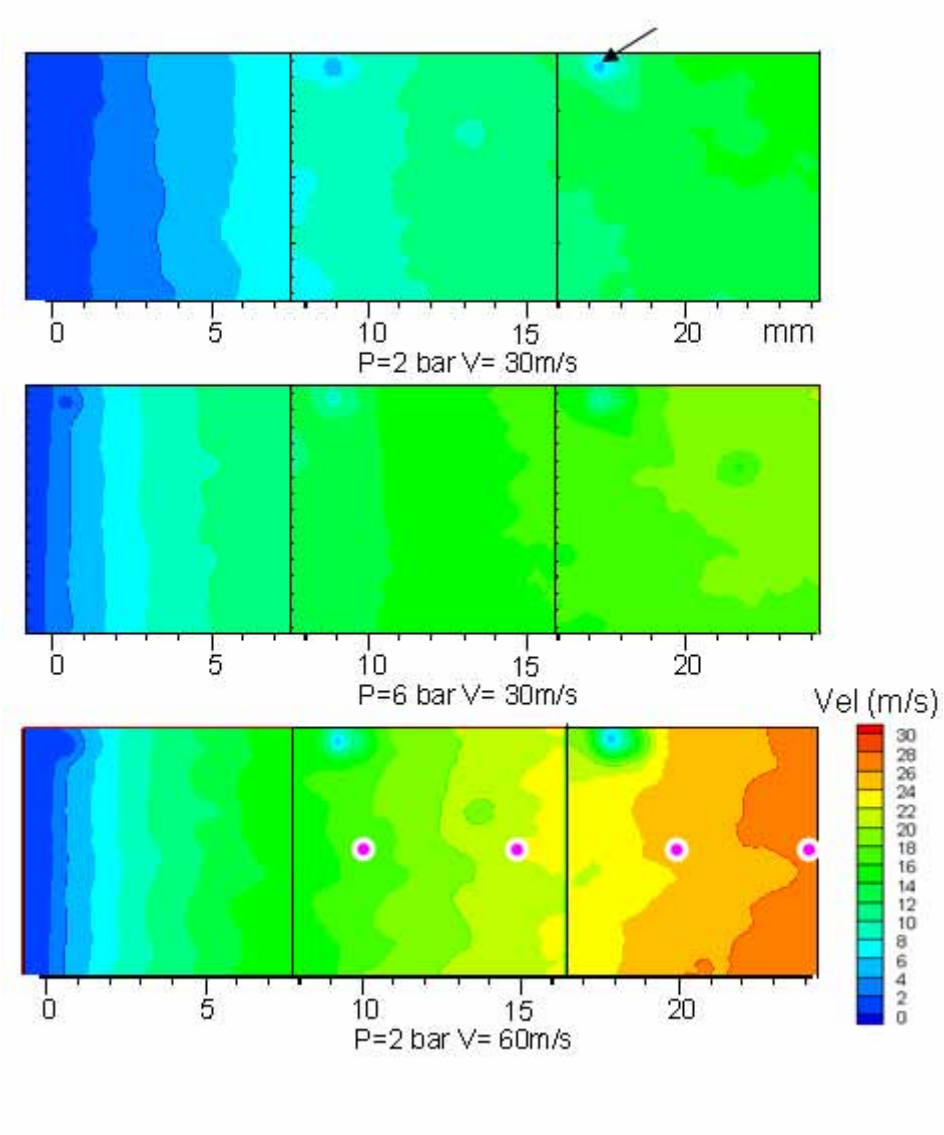

Fig. 3-27 Velocity contours of liquid phase for 4 mm prefilming atomiser

Comparison of PIV and PDA Measurements

The local velocity of the liquid phase obtained from PIV recordings is compared with the PDA measurements to evaluate the short comings of both PDA measurements in the near-field of the atomiser where the droplets are still accelerating and non-spherical. Most of the PDA measurements in the present experimental program are performed in the X-Z plane. The details of the PDA measurements will be dealt in the Chapter 4 on PDA measurements. The PDA measurements are point measurements and are measured at several axial locations. PIV measurements are obtained at different axial locations in the Y-Z plane. Hence there are only few points along the axial direction where the data from both the PIV and PDA measurement technique can be

comparable. These points are at the intersection of the PDA and PIV plane. The measurement points where the comparison is made are marked in pink in Figure 3.27.

As explained in Chapter 2, the PIV algorithm works on cross-correlation of an interrogation window between two sequential images. The shift of the pattern in the interrogation window provides information on the velocity field. However, the algorithm used in the present study does not track individual particles in the interrogation. This implies if the interrogation windows have particles of various sizes, the displacement shift is the net effect of movement of all particles. Since the particles have a definite area in the interrogation window, the velocity-field obtained by the PIV algorithm is surface-weighted mean velocity of the size distribution. Hence surface-weighted mean velocity is used for comparison between two measurement techniques. Surface-weighted mean velocity of the spray distribution at a given location is also calculated for PDA measurements. The comparison between PDA and PIV measurements are shown in Table 3.3. The difference in surface-weighted velocity between PDA and PIV measurements are as high as 15% for axial distances less than z = 15 mm. The PDA measurements show relatively higher velocities compared to PIV. This is expected for two reasons. Firstly, the PDA instrument has lower threshold on the size of the particles. The smaller particles are measured, which in acceleration phase are faster than the bigger particles. Secondly, PDA measures only spherical particles and the velocity is only based the validated spherical particles. At axial distances z =10, 15 mm the validation rates are as low as 40 % in the dense region of the spray. The non-validated particles contain mostly non-spherical particles. In case of PIV measurements, the measurement of velocity is independent of the particle shape. Since the non-spherical particles are relatively larger in size and have not undergone further breakup, the local momentum exchange between surrounding air and the liquid phase tend to produce lower velocities for non-spherical particles compared to the spherical particles. Hence, the PIV measurements show lower velocities compared to PDA measurements. The error is as low as 3%. Beyond z = 15 mm the larger droplets tend to undergo secondary atomisation and PDA measures more droplets. Also, the validation rates are around 60% in dense region of the spray. Hence, the difference between the two measurement techniques gets minimised. At axial distances beyond z = 20 mm, in some cases PIV measurements show higher velocities compared to PDA measurements, for example at P_a = 6 bar and V_a = 30 m/s. This is due to several factors involved in PIV imaging and pre-and post processing.

The images in the PIV recording have a resolution of 8 mm x 8 mm. Hence in order to observe the flow-field, PIV recordings are taken in 8 mm intervals in the axial direction. The minimum particle size that can be measured is 16 μm. Due to the noise in the images mainly due to the CCD chip and partly due to the illumination technique (background) and depth of focus, accurate estimation of the velocities was possible for

particles with diameters ~50 µm. The diameter is calculated from the images based on the area of the particle in the image. Since, in the near-field, a greater quantity of mass flux is expected to be in the particle range greater than 50 µm, estimating the velocity of the particles is expected to give a first approximation of the flow field in the near-field. A low velocity region on top left of the image can be observed in all sections of velocity contour plots in Figure 3.26, 3.27. This is due to the chip defect in that region and a dark fixed region is formed in that area. The PIV algorithm locks to the pixel where the defect and shows low velocity. This is called peak-locking.

The images can be further processed by pattern recognition algorithms to acquire the area distribution of the particles (and hence a first approximation of mass distribution). The PIV algorithm can be further improved to seek structures/particles thus providing velocity information of individual structures/particles. PIV technique is demonstrated in the present case as a promising methodology by which one can measure the velocity of particles.

		z= 10 mm	z= 15 mm	z= 20 mm	z= 25 mm
V= 60 m/s					
P= 2bar	PIV	16.3	22	25.3	27.2
P= 2bar	PDA	20.5(20.6%)	24.2(9.1%)	27.3(7.1%)	30.3(10.4%)
P= 6bar	PIV	29.7	31.7		
P= 6bar	PDA	32.4(8.3%)	39.2(19.%)	42	46.3
V= 30 m/s					
P= 2bar	PIV	9.6	11.4	13.4	13.8
P= 3bar	PDA	11.4(16.1%)		15.6(14.0%)	
P= 6bar	PIV	14.2	16.1	18	18.8
P= 6bar	PDA	13.7(-3.8%)		18.6(3.2%)	

Table 3-3 Comparison of PDA and PIV velocity data

3.9 LIQUID SHEET STABILITY AT THE ATOMISER SLIT

In the flow visualisation experiments, it is observed that under certain operating conditions for nonprefilming atomisers, the liquid sheet does not exist along the entire width of the atomiser slit. Figure 3.28 shows typical images of liquid sheet at the atomiser slit for the same operating condition for a nonprefilming atomiser. At the liquid velocity of 0.45 m/s, the liquid sheet does not exist along the entire span of the atomiser slit. As the liquid velocity is increased to 1m/s, the liquid sheet fills up the entire slit of the atomiser. It is also observed in the experiments that for an operating

condition a minimum liquid velocity is needed to fill the atomiser slit, and it is a function of ambient pressure and air velocity. Higher liquid velocity is required to fill the entire atomiser slit as ambient pressure is increased. Also, an increase of air velocity has a similar effect on liquid sheet. The effect of static pressure in the test section on the liquid sheet stability is more predominant than the air velocity. The acquired images are used to determine the operating limits of the atomisers at which the liquid sheet exist along the entire atomiser slit. This is performed for 300 μm and 500 μm nonprefilming atomisers from earlier designs.

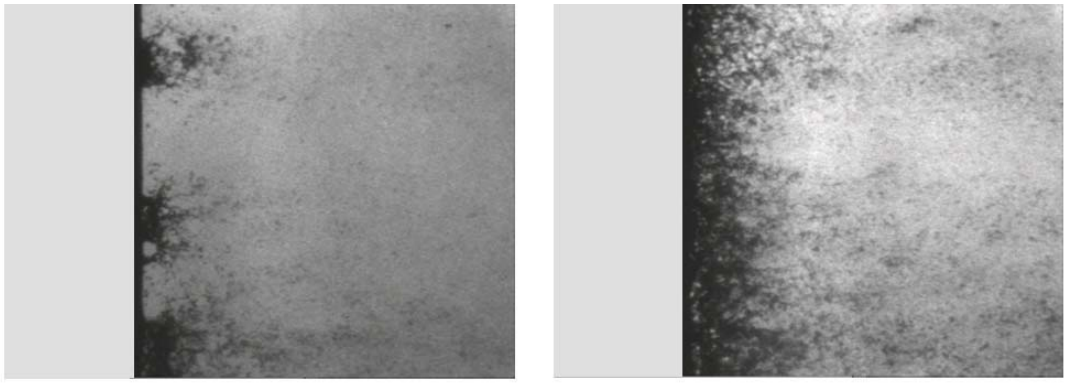

V_{air}=90 m/sec, P_{air}=6 bar, V_{liq}=0.45 m/sec
(a) absence of liquid sheet along the injector slit

V_{air} =90 m/sec, P_{air} = 6bar, V_{liq} =1 m/sec
(b) presence of liquid sheet along the injector slit

Fig. 3-28 Existence of liquid sheet

Figure 3.29(a) shows the limiting conditions below which the liquid sheet break at the atomiser slit. The measurement point on the graph shows the required minimum velocity of the liquid at the atomiser slit for various operating conditions. For simplicity, the required velocity of liquid is plotted for two operating pressures. The curves show the influence of pressure relative to the air velocity. A minimum liquid velocity of 1 m/s is required to have a stable liquid sheet in the slit at ambient static pressures of 6 bar and air velocity of 90 m/s. This is independent of the liquid sheet thickness. This indicates that there is a balance of the pressure drop in the atomiser and the pressure head of the flow. Figure 3.29 (b) shows a logarithmic plot of the limiting conditions for the presence of liquid sheet along the atomiser slit as a function of pressure drop in the atomiser and pressure head of the flow. The linear relationship between the two parameters show that the stability of the liquid sheet at the atomiser slit is determined by these two key parameters. For prefilming atomisers, the liquid film always exists along the atomiser slit for all the operating conditions. Figure 3.30 shows the presence of liquid sheet for a prefilming atomiser at the same operating condition as for

nonprefilming atomiser in Figure 3.28. The presence of liquid sheet at the slit for the prefilming atomiser is clearly visible at the liquid velocity of 0.45 m/s.

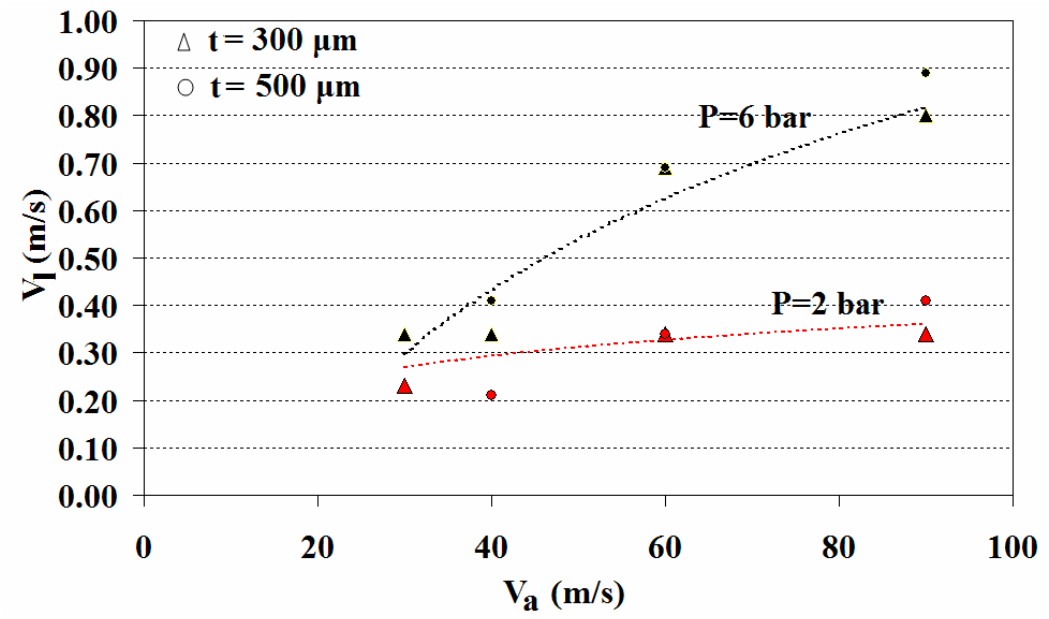

(a)

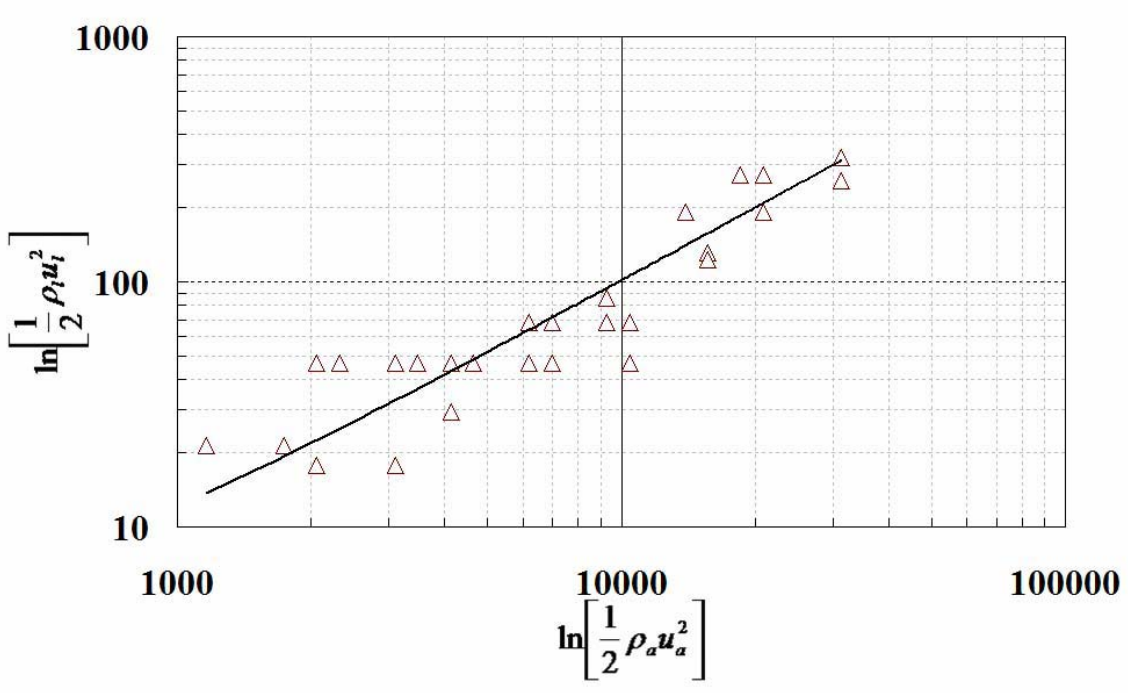

(b)

Fig. 3-29 Limiting conditions of the atomisers

As explained earlier, the absence of a continuous liquid sheet along the entire width of the atomiser slit is observed only for nonprefilming atomisers. In case of the nonprefilming atomiser, when a liquid sheet emerges from the atomiser slit both surfaces of the liquid sheet are exposed to the surrounding air, whereas in case of prefilming atomiser only one of the surfaces of the liquid sheet is exposed to the surrounding air.

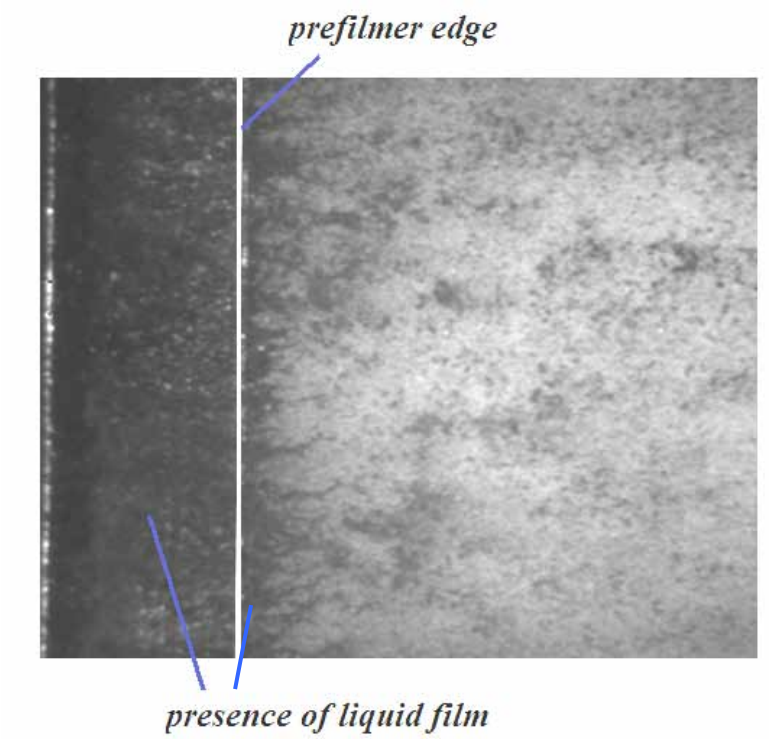

Fig. 3-30 Presence of liquid sheet at the atomiser slit for prefilming atomiser

As explained earlier, the liquid sheet behaves like a thin flexible membrane responding to the vorticity fluctuations in the wake of the atomiser. The presence of airstreams on both sides of the liquid sheet in case of nonprefilming atomiser, make it very susceptible to differential pressure across the liquid sheet. The differential pressure occurs due to vorticity fluctuations. For a liquid sheet to emerge from the atomiser slit, for either of the atomisers, a minimum positive pressure drop is required in the atomiser depending upon the exit conditions. In case of nonprefilming atomisers, the pressure drop has to take into account the differential pressure across the liquid sheet and hence for nonprefilming atomisers higher liquid velocities are required. As shown in Figure 3.31, if a small differential pressure occurs on both sides, the differential pressure is balanced by internal pressure and shear forces. So if the internal pressure (which is a direct function of pressure drop in the atomiser and hence the mass flow rate of the liquid) is less than a critical value, the liquid sheet breaks at the atomiser lip. In case of prefilming atomiser, due to adhesive (wetting) property of the liquid, at this minimum

pressure drop the liquid fills the atomiser slit. When the liquid emerges out of the atomiser slit, the surface tension forces on the free liquid surface tend to balance the external forces. Hence the liquid sheet starts thinning (since the liquid sheet starts accelerating). The aerodynamic forces can be increased either by increasing the air velocity or by increasing the static pressure. However, the static pressure produces a force normal to the thickness of the liquid sheet. These forces are balanced by the internal pressure of the liquid and the shear force of the liquid acting in the normal direction to the thickness of the liquid sheet. Since prefilmer surfaces exists on one side of liquid sheet, the pressure load on the liquid sheet is born by the prefilmer surface and so it is more resistant to liquid sheet breakup. Also, due to the adhesive properties of the liquid, the liquid tend to wet the prefilmer surface and hence spreads more on the prefilmer plate.

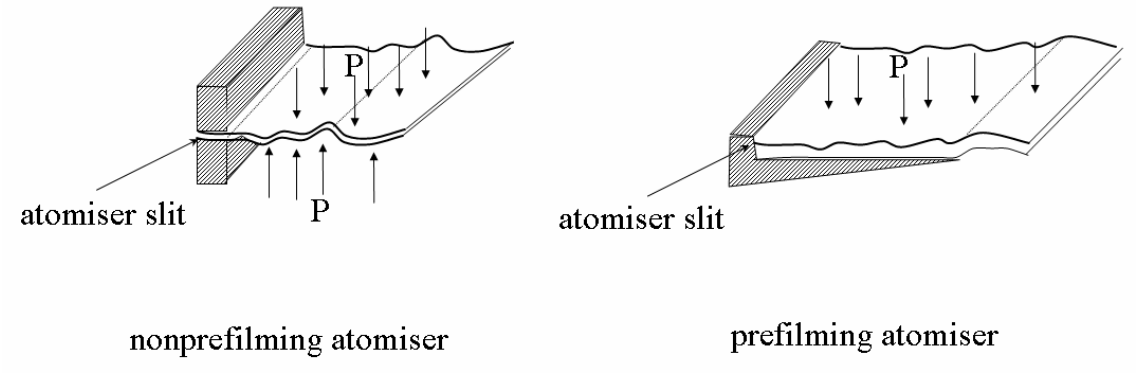

Fig. 3-31 Stability of liquid sheet at the atomiser slit

CHAPTER 4

SPRAY CHARACTERISATION OF ATOMISERS

This chapter discusses the PDA measurements performed on the 4mm prefilming and nonprefilming atomiser of the new atomiser design. The thickness of the liquid sheet in both cases is 300 μm. The static pressure and air velocity are varied in the test section at constant kerosene mass flow rate. PDA measurements are performed to analyse whether the differences observed in primary atomisation behaviour for the atomisers is reflected in the final droplet size distribution and spray characteristics. The measurement locations and the operating conditions are described in Chapter 2. The two dimensionality of the spray from the atomisers and the effect of operating conditions on spray characteristics are discussed in detail. Correlations for the Sauter Mean Diameter (SMD) are also discussed in the present chapter.

4.1 TWO DIMENSIONALITY OF THE SPRAY

In order to assure the significance of the measured spray characteristics, it is essential to conduct experiments to validate the two dimensionality of the spray emerging from the atomisers. As described in Chapter 2, most of the measurements are performed in the central plane (y = 0 mm) perpendicular to the span of the atomisers for comparative studies on the atomisers. The two dimensionality is verified at an axial location of z = 90 mm. It is necessary to observe the volume flux distribution of kerosene along the span of the atomisers to confirm the 2 dimensionality. This has to be supported by the SMD profiles and mean and RMS velocity profiles along the span of the atomiser. If SMD profiles, velocity profiles and volume flux profiles are similar for an atomiser, then measurements can be performed in the y = 0 mm plane.

4.1.1 Spanwise distribution of volume flux

Figure 4.1 shows the variation of volume flux for both prefilming and nonprefilming airblast atomisers. As shown in Figure 4.1(a) for the nonprefilming airblast atomiser, the volume flux distribution is symmetric across the X-axis. The X-axis profiles along the span from y = -4 mm to 4 mm indicate that the volume flux is uniformly distributed along the span of the atomiser. However, it can be observed that at y = 4 mm, the volume flux is lesser compared to other profiles. The mean velocities in the lower half of the test section are relatively lower compared to the velocity in the centre of the test section and hence the spray bends towards the lower half of the test section. It has to be noted that +Y is towards the bottom of the test section. As explained

in Appendix (B) the velocities in the lower half of the test section are smaller due to a thicker boundary layer. The symmetric nature of the spray i.e., X-axis profiles across Y-axis is observed for all operating conditions. Also the width of the spray along the X-axis is symmetric from y = -4 mm to y = 4 mm. The width of the spray is from y = -12 mm to 12 mm. The details of the calculation of spray width are explained in section 4.1.3.

Figure 4.1(b) shows the volume flux distribution for the 4 mm prefilming airblast atomiser. As can be observed, there is a shift of ~1 mm in the X-axis profiles in the +X direction. For this particular operating condition the shift is due to the positioning error. Measurements for evaluating the spanwise uniformity of the spray are made during a separate experimental campaign and the error in positioning could not be traced. In fact, for all the operating conditions including the operating condition presented in this section, a systematic shift of the peak of the volume flux profile towards the –X direction by ~ 0.5 mm is observed. Mie scattering images in Figure 2.9, Chapter 2, also reveal a shift of the spray in the –X direction. As explained in Figure 2.17, Chapter 2, the –X direction corresponds to surface of the liquid sheet being exposed to the free stream air when the liquid sheet is propagating on the prefilming surface. So, this is due to the aerodynamic effects caused by the presence of prefilming surface. This is explained in section 4.2.6. It can also be observed that the width of the spray is rather smaller than the one of the nonprefilming airblast atomiser. In comparison with the nonprefilming atomiser the volume flux is relatively higher in the centre of the spray, as the spray is narrower. Also, the width of the spray is symmetric from y = -4 mm to 4 mm. The spanwise variation of SMD distribution and mean velocity distribution play an important role in evaluating the two dimensionality of the spray. The SMD distribution indicates whether there exist any differences between both atomisers. For brevity in presentation of results, these are discussed in Appendix C.

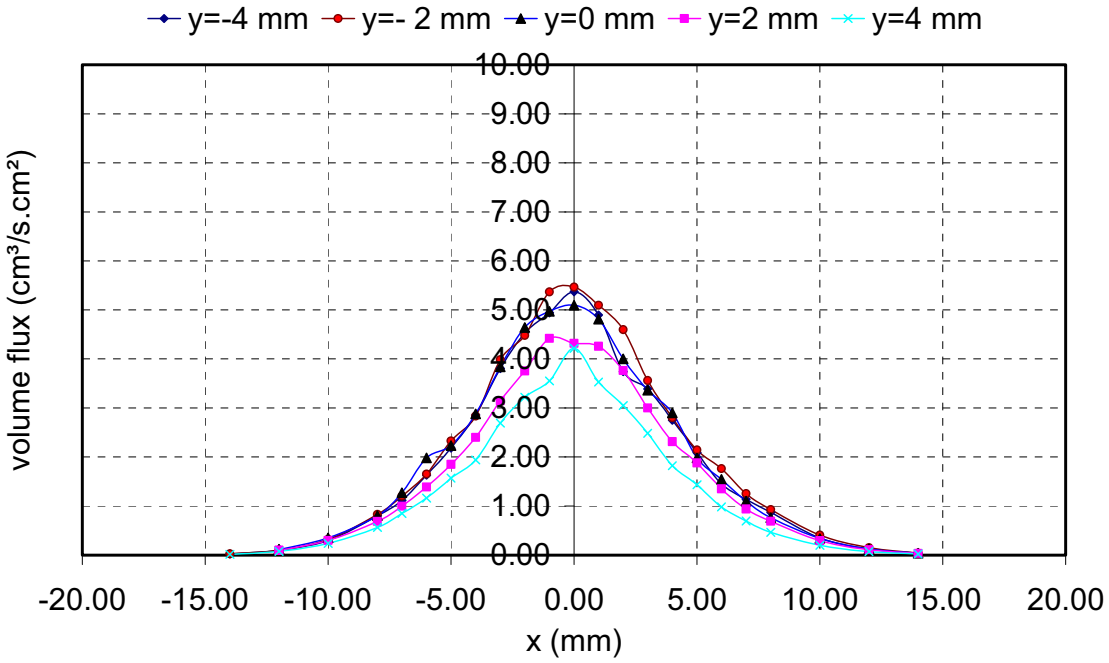

(a) nonprefilming airblast atomiser

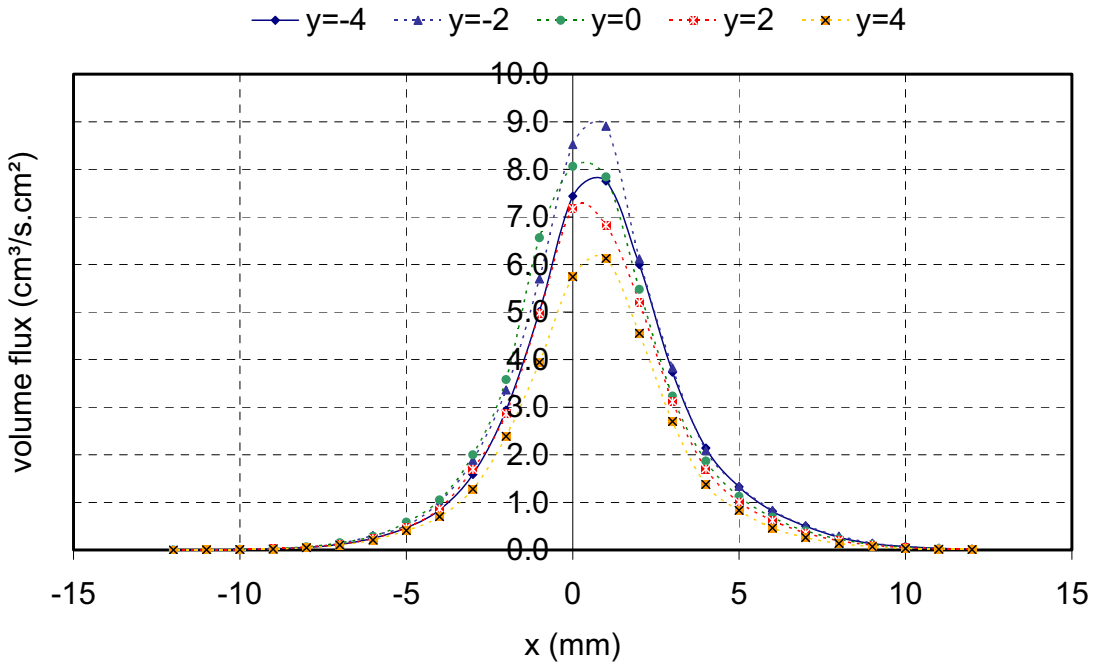

(b) 4mm prefilming airblast atomiser

Fig. 4-1 Volume flux distribution along the span of atomisers at P_a = 2 bar and V_a = 60 m/s (z = 90mm)

4.1.2 Spanwise distribution of Global SMD (GSMD)

To quantify the concrete effect of local volume flux distribution and the variation of local SMD on the spanwise distribution of the spray, a term called 'Global

SMD' is defined. Global SMD (GSMD) is 'local volume flux' weighted average of local SMD along one X-axis profile.

$$GSMD = \frac{\sum_{x=i}^{x'=n} V_i . SMD_i}{\sum_{x=i}^{x=n} V_i} \text{ at y = c} \qquad \text{Eq. 4-1}$$

This gives a unique SMD along an X-axis profile for an operating condition. For comparison between atomisers usually the global SMD is used. The global SMD of the spray is calculated along various X-axis profiles at y = -6 mm to y = 6 mm. Figure 4.2 shows the variation of GSMD for both prefilming and nonprefilming airblast atomisers. As can be observed, the GSMD variation along the span is minimal for nonprefilming airblast atomiser. The variation of the global SMD is marginally higher along the span for the 4 mm prefilming airblast atomiser. This is due to the new design of the prefilming atomiser. In the new atomiser design, the span of the prefilming surface is 38 mm, as shown in Figure 2.4, Chapter 2. However, the span of the liquid sheet emerging from the atomiser slit is 12 mm. The liquid sheet spreads on the prefilming surface due to adhesive properties of the liquid and hence produces tail effects. It can be observed in the Mie scattering images in Figure 2.9, Chapter 2 that the spread is minimal. As the comparison is made far downstream of the atomiser, these effects are more visible in the profiles. The variation of GSMD between planes y = 0 mm and y = 6 mm is less than 5% for the prefilming atomiser.

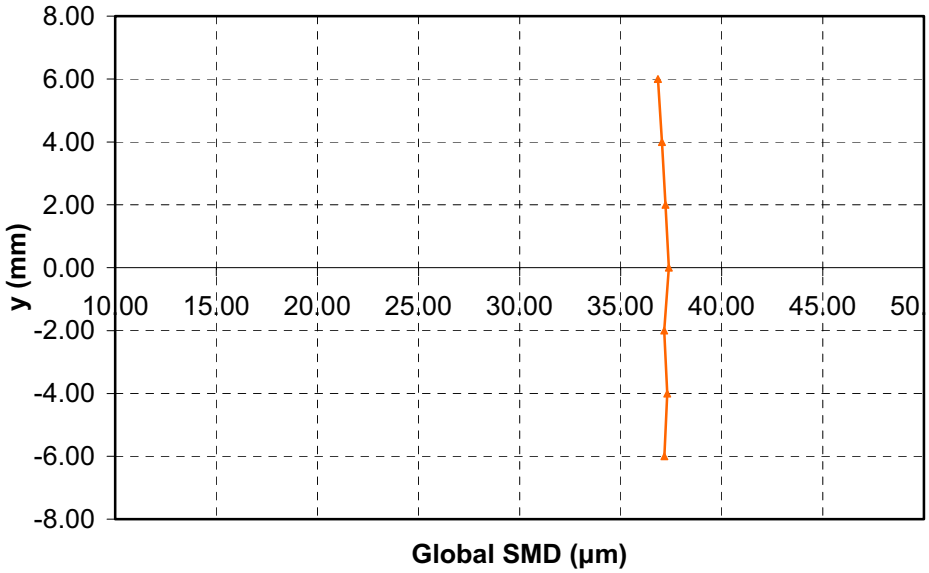

(a) nonprefilming airblast atomiser

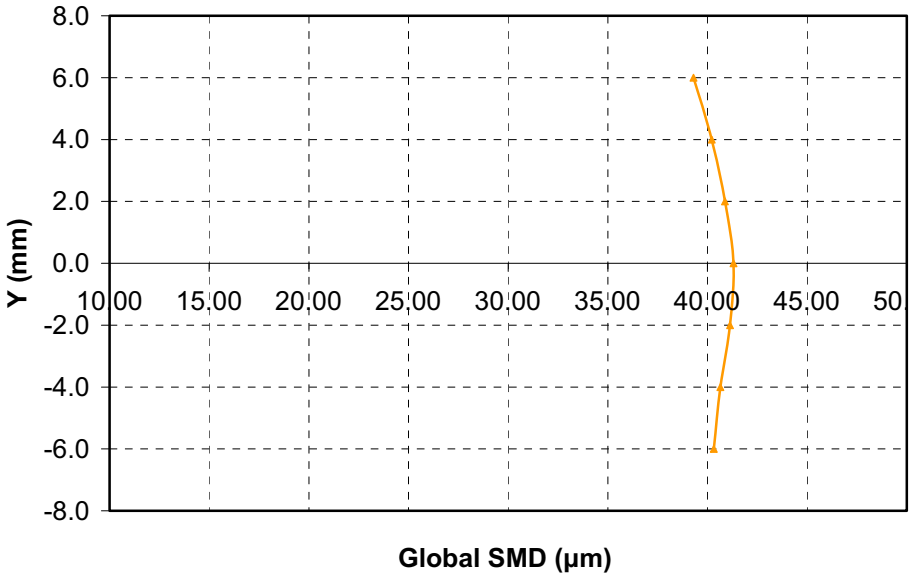

(b) 4mm prefilming airblast atomiser

Fig. 4-2 GSMD along the span of atomisers at P_a = 4 bar and V_a = 60 m/s (z = 90mm)

The minimal variation of GSMD and volume flux profiles indicates that the spray of both the atomisers is highly two dimensional. The liquid sheet behaviour along the entire span of both prefilming and nonprefilming atomisers is similar and hence the comparison between the atomisers can be performed along the centre plane y = 0 mm.

Before discussing the effect of operating conditions on spray characteristics, it is important to know the errors involved in PDA measurements in dense sprays. There are several parameters that govern the quality of PDA measurements like orientation of transmitting optics, scattering angle, measurement volume diameter, beam spacing, aperture, beam diameter etc. The optimization of these parameters is described in Chapter 2. The detailed effects of the positioning of the transmitting optics on PDA measurements on droplet size in the present case are described in Appendix D. Also the quality of measurements in the near-field of the atomiser is discussed in Appendix D.

4.2 COMPARISON OF THE SPRAY CHARACTERISTICS OF THE ATOMISERS

4.2.1 Choice of axial position on droplet size measurements

There are several factors that have to be taken into account for the comparison of both atomisers and to quantify the effect of operating conditions on spray characteristics. The essential information required is the evolution of the spray just from the atomiser to the flame-front inside the combustor. Typically the flame-front is 25 mm away from the atomiser in gas turbine combustors. At these lengths scales, the atomisation is complete. But, the reliability of PDA measurements is affected by factors

discussed in Appendix D. The comparison of atomisers is performed at an axial distance of z = 90 mm from the atomiser. Several key issues have to be addressed and justified for comparison in the far-field at 90 mm from the atomiser. Firstly, it has to be known whether there is any secondary atomisation beyond z = 25 mm. Secondly, it has to be known whether the droplets are accelerating, as this will affect the spherical nature of large droplets and will effect the PDA measurements. Thirdly, the spray dispersion along the axial direction has to be known, as this will affect the volume flux distribution in a plane perpendicular to the flow direction and affects the global properties of the spray. As discussed earlier, the measurements are performed in the y = 0 mm plane. Hence, dispersion effects have to be considered. Lastly, the volume flux distributions have to be checked for consistency along the axial direction.

Secondary Atomisation

The secondary atomisation occurs if the Weber number (We_p) > 22 for a droplet in accelerating flows and We_p > 13 if the droplet is suddenly exposed to an air stream. The Weber number is calculated based on the relative velocity between the droplet and the air stream and diameter of the droplet. In the present experimental study at z = 25 mm, the characteristic diameter $D_{0.9}$ has a maximum of 100 μm at a static pressure of 6 bar and air velocity of 30 m/s. The maximum relative velocity between a droplet of size 100 μm and the air stream, measured from the droplet size distribution data, is ~ 15 m/s. Typically, the We_p is ~ 7.88 for a particle of 100 μm particle with a relative velocity of 15 m/s which is well below the secondary droplet breakup regime. Hence, there is no existence of secondary atomisation beyond axial location of z = 25 mm.

Sphericity of Large Droplets

As explained in the beginning of Section 4.2.1, it is necessary to know whether the droplets have reached the sphericity. The standard PDA used in the present experiments cannot validate non-spherical particles. The measurements are made at axial location z = 90 mm. Further downstream could not be made due to the obstructions to the receiving optics at the test rig. So, at the axial location where the comparison of SMDs between the atomisers is made, it is necessary to have an estimate the level of sphericity of droplets and the invalidated particles. Usually, as explained in Chapter 1, the elliptical nature of the droplets is represented by the Bond number (Bo). The large droplets formed after secondary atomisation experience acceleration due to increased exchange of momentum with the surrounding air. This leads to large droplets turning elliptical and, depending on the differential velocity, they can take various shapes [14]. Higher Bond numbers indicate that the droplet is experiencing acceleration and the shape of the droplet is more elliptical. The sphericity depends on the droplet Reynolds number (Re_p), relative velocity between the droplet and the air stream, diameter of the particle, viscosity of air and surface tension. For the operating

conditions tested, the maximum Re_p ~ 500. Usually, the droplet deforms for Bo ~ 0.4-0.6 for the particle Re_p range of 500-1000 [14]. Table 4.1 shows the Bond number for various characteristic droplet sizes at various operating conditions experiencing relative velocity from z = 25 mm to 90 mm at x = 0 mm and y = 0 mm. The Bond number decreases along the axial direction for all the characteristic diameters. Droplets of size greater than the $D_{0.5}$ have Bond number > 0.4 at z = 45 mm indicating that they deform and contribute to the rejection of burst by PDA processor. As the droplets accelerate reach the terminal velocity. At z = 90 mm, $D_{0.9}$ have Bond number ~ 0.6 which is not high and since standard PDA is adopted which calculates the phase from only green beams and spherical check is not stringent as in Dual PDA, the rejection rate is mainly due to beam steering effect. The validation rates are also higher at z = 90 mm, as will discussed in later section. It can be also observed that the Bond number is relatively higher for 4 mm prefilming atomiser. As explained in earlier sections, the spray width is narrow for the prefilming atomiser. The volume flux in the centre region of the spray is higher compared to nonprefilming atomiser. The droplets accelerate slower due to less interaction of the free stream air and the spray and hence the Bond number is higher for the prefilming atomiser.

4mm prefilming atomiser				**Bond Number**			
z (mm)	**We**	**P_a(bar)**	**V_a (m/s)**	**SMD**	**$D_{0.1}$**	**$D_{0.5}$**	**$D_{0.9}$**
25.0	169.0	6.0	40.0	0.567	0.226	0.756	1.842
45.0	169.0	6.0	40.0	0.452	0.162	0.654	1.179
90.0	169.0	6.0	40.0	0.356	0.161	0.496	0.664
25.0	380.0	6.0	60.0	0.617	0.142	0.629	2.034
45.0	380.0	6.0	60.0	0.451	0.179	0.616	1.384
90.0	380.0	6.0	60.0	0.452	0.173	0.612	0.629
25.0	855.0	6.0	90.0	0.511	0.095	0.532	1.579
45.0	855.0	6.0	90.0	0.363	0.081	0.382	1.073
90.0	855.0	6.0	90.0	0.347	0.162	0.393	0.687
nonprefilming atomiser				**Bond Number**			
z (mm)	**We**	**P_a(bar)**	**V_a (m/s)**	**SMD**	**$D_{0.1}$**	**$D_{0.5}$**	**$D_{0.9}$**
25.0	169.0	6.0	40.0	0.207	0.067	0.284	0.918
45.0	169.0	6.0	40.0	0.189	0.056	0.292	0.628
90.0	169.0	6.0	40.0	0.152	0.057	0.238	0.479
25.0	380.0	6.0	60.0	0.328	0.143	0.442	1.058
45.0	380.0	6.0	60.0	0.187	0.053	0.281	0.777
90.0	380.0	6.0	60.0	0.198	0.103	0.228	0.582
25.0	855.0	6.0	90.0	0.251	0.065	0.373	1.048
45.0	855.0	6.0	90.0	0.148	0.042	0.293	0.720
90.0	855.0	6.0	90.0	0.211	0.081	0.257	0.650

Table 4-1 Variation of Bond number for characteristics diameter along axial direction

The size-velocity correlation graph between droplet size class and velocity is also a good indicator of droplet acceleration. Figure 4.11 shows the size-velocity correlation for two operating conditions for the 4 mm prefilming airblast atomiser. The curves show the axial locations from the atomiser where size-velocity correlation is plotted. The particles of size class < 2.5 µm usually represent gas velocity. Usually, the small particles reach the gas velocity close to the atomiser. As can be observed, as the axial distance increases the slope of the curves decreases. At z = 75 mm and beyond, the difference in slopes of the curves is small indicating that the particles are reaching the gas velocity. The difference in velocity between the bigger particles > 40 µm and smaller particles is due to the different relaxation times required for the droplets to reach the gas velocity.

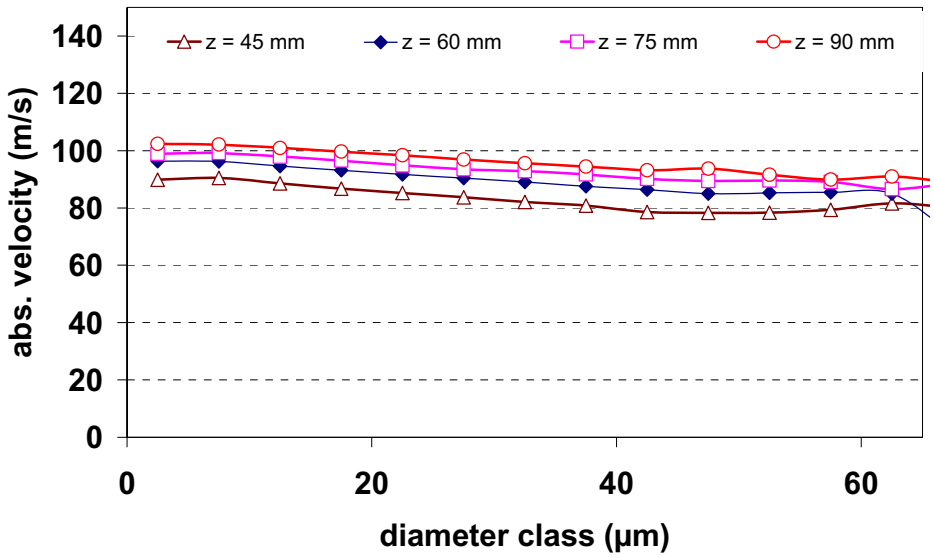

Fig. 4-3 Size-velocity correlation for 4 mm prefilming atomiser
P_a = 4 bar, V_a = 90 m/s

Spray Dispersion

Another aspect that has to be taken into account is the dispersion of spray into the free stream. The measurements performed for comparison of atomisers are made only in one plane (Y= 0 mm). The atomisers used in the present measurements are two dimensional. Hence, it is important to know spray dispersion that occurs in the cross-sectional plane perpendicular to the flow direction. The study of dispersion is undertaken here only to observe the selective dispersion of droplet size classes due to mean characteristics of the flow. The dispersion of the spray depends on the relative velocity between the droplet and air, droplet size class, local droplet concentration and local turbulence characteristics of the flow. The interaction between these parameters is quite complicated. For example, an increase in droplet concentration reduces turbulence levels and hence reduces droplet dispersion; presence of bigger particles increase

turbulence levels where as smaller droplets suppresses turbulence levels. The details of which are explained by Hetsroni [35]. The droplet Reynolds number (Re_p) which is a measure of relative velocity between droplet & air stream and droplet size, if it is high increases the turbulence level. Usually, $Re_p > 400$ generates vortex shedding behind the droplet. In the present experimental study, at z = 25 mm, P_a = 6 bar, U_{rel} = 15 m/s, D_p = 65 μm has $Re_p \sim 413$ which is an extreme condition. In realistic operating conditions, the effect of swirl and high turbulence levels play an important role in local droplet concentration, which directly affects the combustion characteristics of two phase flow and production of NO_x. However, in the present study, the flow does not have swirl and the spray dispersion is rather small.

The size classes selected for spray dispersion analysis are the characteristic diameters $D_{0.1}$, SMD, $D_{0.5}$ and $D_{0.9}$. The Particle/droplet relaxation time and characteristic time is calculated for these diameters. Stokes number is calculated as the ratio of particle relaxation time to characteristic time. The characteristic time (τ) is calculated the ratio of characteristic length to spatial change in velocity of mean flow field.

$$\tau = \Delta l/U, \qquad \text{Eq. 4-2}$$

where Δl is the characteristic length of the test section which is taken as ($\Delta l = \sqrt{40^2 + 40^2}$ = 56.56 mm) & U is the bulk air velocity in the test section. It has to be noted that the actual local air velocity is less compared to the bulk air velocity due to the initial exchange of momentum during the sheet breakup phase.

The particle relaxation time is calculated as

$$\tau_{rel} = \frac{1}{18} \frac{\rho_p d_p^2}{\mu_a (1 + 0.15.\mathrm{Re}_p^{0.687})} \qquad \text{Eq. 4-3}$$

where ρ_p is the density of particle, d_p is the diameter of the particle, μ_a is the dynamic viscosity of the air and Re_p is the Reynolds number of particle.

Table 4.2 gives the relative velocities, characteristic time scales and Stoke numbers for characteristic diameters at different operating conditions at x = 0 mm and y = 0 mm axis along the axial direction. The combined effect of the operating conditions on spray dispersion is represented by the Stokes number. As can be observed from the table, the Stokes number varies depending on the diameter class. As expected, $D_{0.1}$ tends to have a Stokes number smaller than other characteristic diameters. The Stokes number increases as the diameter of the particle increases. $D_{0.1}$ has a Stokes number of ~ 0.3 indicating particles of a size class of the $D_{0.1}$ follow the flow. Particles of size up to

$D_{0.5}$ have a Stokes number range from 0.3 - 0.5 at all operating conditions indicating they closely follow the flow. Larger droplets indicated by $D_{0.9}$ have Stoke numbers of order ~1. This shows that there is a selective dispersion of droplets based on the particle size class. This is because the relaxation times are different for different droplet size classes as smaller particles tend to reach the gas velocity more quickly and follow the flow than bigger particles, as explained in the earlier section. However, the relative variation Stokes number between characteristic diameters is less and the dispersion is due to the high droplet concentration. The Stokes numbers also reveal that there is not much significant size based selective dispersion of droplets that will be observed usually in swirl based or vortex based flows. This can also be confirmed with the variation of global SMD along the axial direction.

4mm Prefilming atomiser				**Stokes number**			
z (mm)	**We**	**P_a (bar)**	**V_a (m/s)**	**SMD**	**$D_{0.1}$**	**$D_{0.5}$**	**$D_{0.9}$**
25.0	169.0	6.0	40.0	0.59	0.33	0.70	1.33
45.0	169.0	6.0	40.0	0.82	0.49	0.96	1.73
90.0	169.0	6.0	40.0	1.05	0.61	1.25	2.07
25.0	380.0	6.0	60.0	0.50	0.33	0.60	1.05
45.0	380.0	6.0	60.0	0.62	0.35	0.70	1.33
90.0	380.0	6.0	60.0	0.79	0.47	0.92	1.79
25.0	855.0	6.0	90.0	0.45	0.33	0.51	0.86
45.0	855.0	6.0	90.0	0.51	0.35	0.60	0.93
90.0	855.0	6.0	90.0	0.63	0.35	0.72	1.18
Nonprefilming atomiser				**Stokes number**			
z (mm)	**We**	**P_a (bar)**	**V_a (m/s)**	**SMD**	**$D_{0.1}$**	**$D_{0.5}$**	**$D_{0.9}$**
25.0	169.0	6.0	40.0	0.72	0.40	0.85	1.45
45.0	169.0	6.0	40.0	1.09	0.68	1.21	2.00
90.0	169.0	6.0	40.0	1.22	0.70	1.39	2.34
25.0	380.0	6.0	60.0	0.59	0.33	0.65	1.21
45.0	380.0	6.0	60.0	0.90	0.57	0.96	1.47
90.0	380.0	6.0	60.0	1.02	0.56	1.21	1.82
25.0	855.0	6.0	90.0	0.60	0.39	0.58	1.07
45.0	855.0	6.0	90.0	0.82	0.54	0.76	1.18
90.0	855.0	6.0	90.0	0.84	0.53	0.91	1.34

Table 4-2 Stokes number for various characteristic diameters

Figure 4.4 shows the variation of global SMD along the axial direction for both prefilming and nonprefilming atomisers. The increase in SMD from z = 25 mm to z = 90 mm is due to two reasons. Firstly, the increase is attributed to increase in validation

rates as more spherical larger droplets are validated beyond z = 45 mm. Secondly, smaller droplets disperse in the cross sectional plane perpendicular to the axial direction leading to the presence of larger droplets in the centre of the spray.

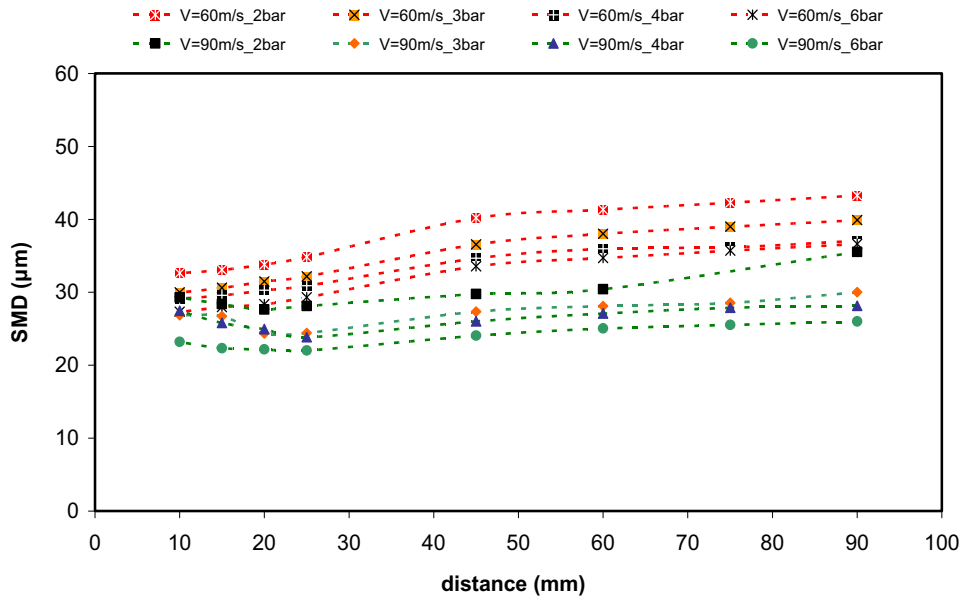

(a) nonprefilming airblast atomsier

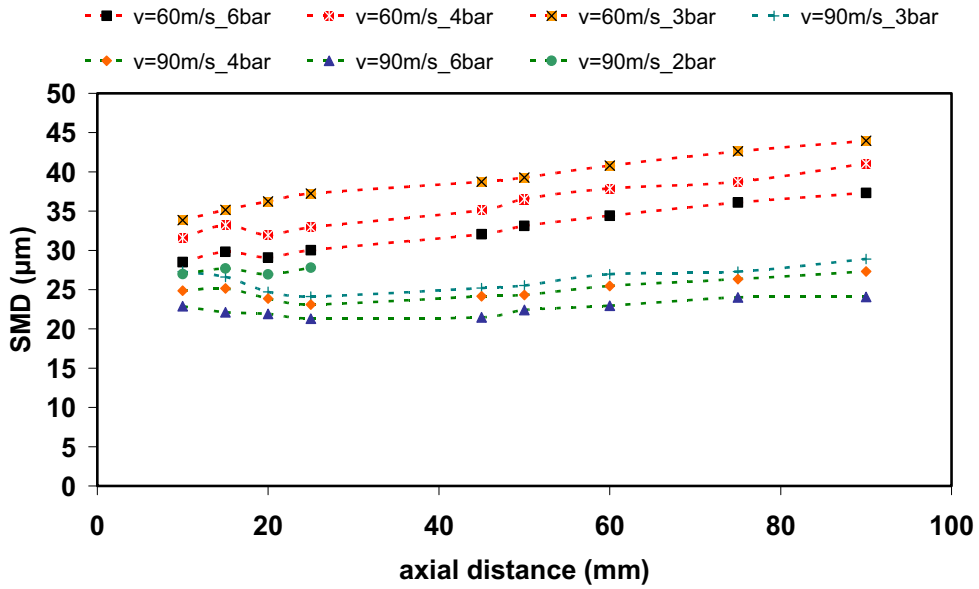

(b) 4mm prefilming airblast atomiser

Fig. 4-4 Variation of GSMD along axial direction

Volume Flux Measurements

The comparison of atomisers is performed where volume flux measurements from PDA measurements are consistent along the axial direction. In the near field of the atomiser, the rejection of burst signals is due to presence of nonspherical droplets and due to high spray density. Usually the large nonspherical particles contribute to errors in

volume flux measurements. As measurements are made further downstream, the nonspherical droplets may undergo secondary breakup or attain sphericity depending on the aerodynamic forces acting on the droplet. The consistency in volume flux measurements also depends on the spray density as the rejection rate by PDA depends also on the presence of more than one particle in measurement volume and on beam steering effect caused due to dense spray. The volume flux measurements along the axial direction when the spray density is low; validation rates are high, droplets are spherical and the effects of beam steering are small. Figure 4.5 shows that volume flux distributions from z = 45 to 90 mm for the prefilming and nonprefilming atomisers.

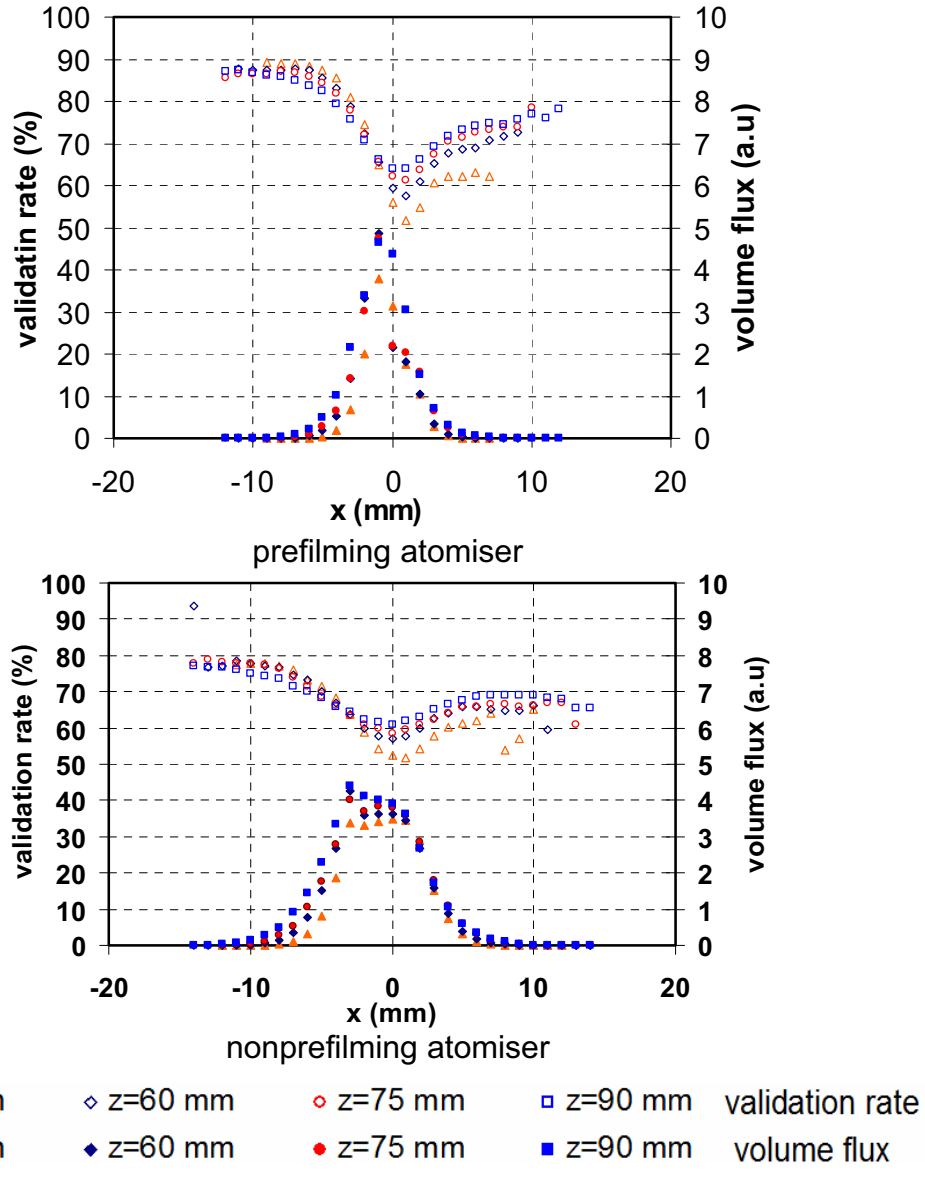

Fig. 4-5 Volume flux distribution at various axial locations P_a = 6 bar, V_a = 60 m/s

As can be observed, the validation rates increase along the axial direction. This is because the spray density decreases along the axial direction. As discussed in earlier

sections, the secondary atomisation is complete beyond axial distance of 25 mm. The increase in validation rates is due to the nonspherical particles attaining sphericity as the droplets reach gas velocity. The increase in validation rates is also reflected in higher volume flux measurements as shown in the Figure. The volume flux profiles are consistent along the axial direction beyond z = 75 mm. So, the volume flux of the liquid in sufficiently captured by the PDA measurements and the minor variations in volume flux profiles are due to the dispersion of the spray as discussed in the previous section. The narrowness of the volume flux profiles for the prefilming atomiser in comparison with nonprefilming atomiser indicates that the volume distribution in a cross sectional plane is less for the prefilming atomiser compared to the nonprefilming atomiser.

4.2.2 Width of Spray

The width of the spray is obtained from the PDA measurements at y= 0 plane. The width is calculated considering the 2σ limits of the Volume flux distribution along the X-axis. The absolute width of the spray is then defined by

$$width(4\sigma) = 4.\sqrt{\frac{\sum_{x=i}^{x=n} V_i . x_i^2}{\sum_{x=i}^{x=n} V_i} - \left(\frac{\sum_{x=i}^{x=n} V_i . x_i}{\sum_{x=i}^{x=n} V_i} \right)^2} \qquad \text{Eq. 4-4}$$

where σ is the standard deviation, V_i is the volume flux, x_i is the location of the volume flux measurement.

The width of the spray is calculated at various operating conditions for both atomisers at various axial locations. Figure 4.6(a) shows the effect of static pressure on the width of the spray. The closed symbols correspond to the nonprefilming atomiser and the open symbols correspond to 4 mm prefilming atomiser. As the static pressure increases at constant velocity, the width of the spray decreases for both the atomisers. However, the effect of pressure is higher for the nonprefilming atomiser compared to prefilming atomiser. The width of the spray is wider for the nonprefilming atomiser compared to the prefilming atomiser. Since for the nonprefilming atomiser the liquid sheet and the structures oscillate after the sheet breakup, the width of the spray tends to be wider. It can be recollected that the liquid sheet oscillations are suppressed in the prefilming atomiser due to shear stripping and uneven vorticity on both sides of the atomiser. Figure 4.6(b) shows the effect of air velocity on the width of the spray at a constant static pressure. The effect of velocity is more evident for the nonprefilming atomiser than for prefilming atomiser. Similarly, the effect of velocity on spray width is higher for nonprefilming atomiser than for prefilming atomiser. Basically, an increase in static pressure or air velocity tends to reduce the spray width.

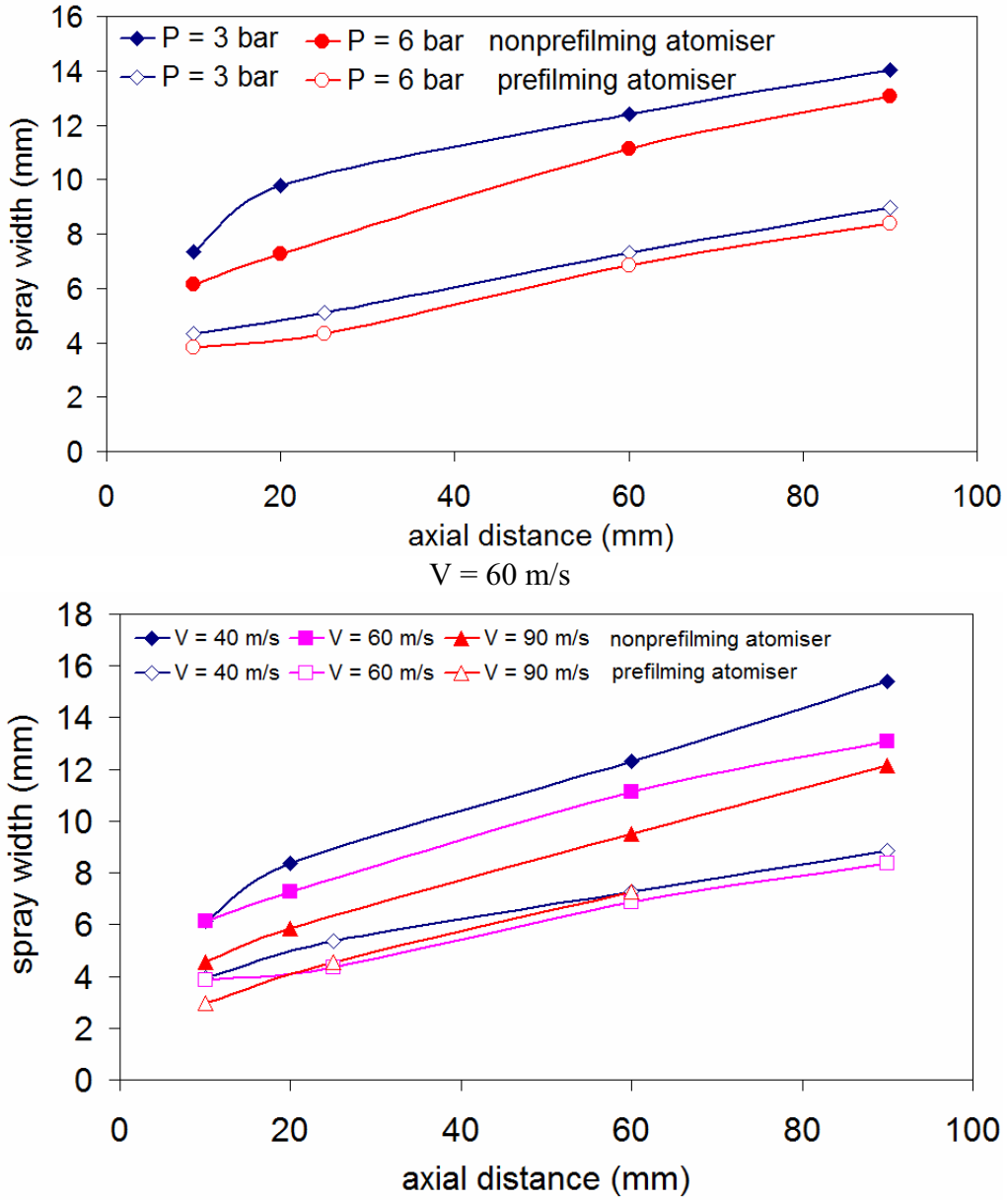

Fig. 4-6 Effect of pressure and air velocity on width of the spray

4.2.3 Evolution of $D_{0.9}$, $D_{0.5}$, $D_{0.1}$ along the axial direction

Figure 4.7 and Figure 4.8 show the effect of the operating conditions on the evolution of 90% volume undersize diameter ($D_{0.9}$), 50% volume undersize diameter ($D_{0.5}$), 10% volume undersize diameter ($D_{0.1}$) and span along the axial direction for both atomisers. In the near-field of the atomiser between z = 10 - 25 mm, the $D_{0.9}$ shows a downward trend for the operating conditions plotted in the graph. Further downstream of the atomiser the $D_{0.9}$ attains a nearly constant value. This is because the droplets formed very close to the atomiser are large and accelerating. As the larger droplets travel downstream, they undergo secondary atomisation and hence the $D_{0.9}$ decreases.

The secondary atomisation is complete and hence the $D_{0.9}$ reaches a nearly constant value. In comparison the $D_{0.1}$ increases along the axial direction. This is due to the dispersion of smaller droplets along the axial direction. As the smaller droplets disperse quicker into the free stream, the relative smaller droplets along X-axis profile increases and hence the $D_{0.1}$ increases. $D_{0.5}$ follows similar to $D_{0.1}$. As discussed in earlier paragraphs, the $D_{0.5}$ has higher dispersion relatively to $D_{0.9}$ and hence $D_{0.5}$ increases. The span of a spray represents the range of droplets in a distribution, as discussed in Chapter 1. Initially, the span decreases along the axial direction due to the simultaneous decrease of $D_{0.9}$ and increase of $D_{0.1}$ & $D_{0.5}$. Further downstream of the atomiser, since the effect of spray dispersion is marginal, the span attains a constant value. The Figures show that the span of the spray for both atomisers is similar. At higher Weber numbers the span is smaller indicating a narrow spray distribution. Also, the $D_{0.1}$, $D_{0.5}$, $D_{0.9}$ all decrease as the Weber number increases.

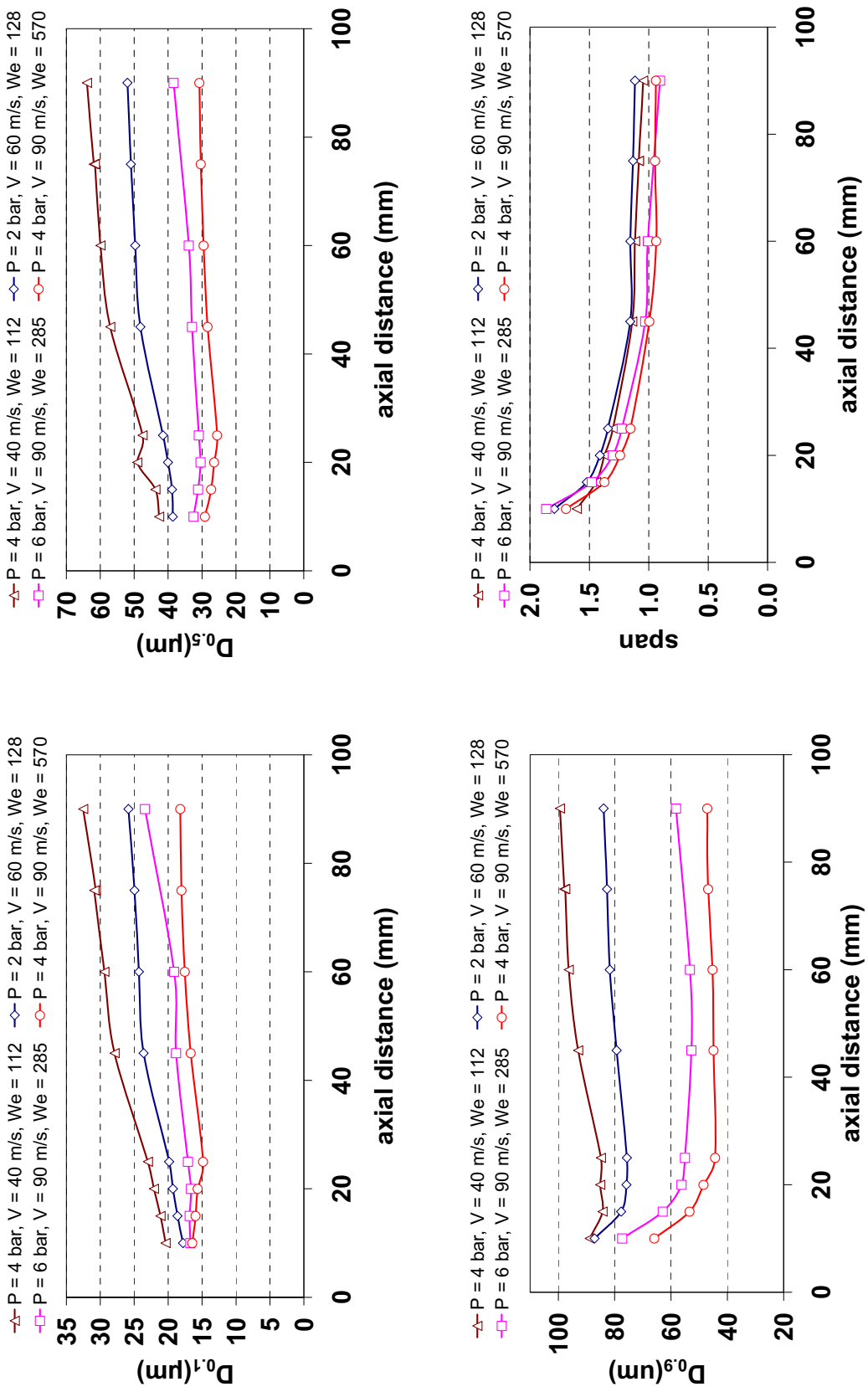

Fig. 4-7 Effect of operating conditions on $D_{0.1}$, $D_{0.5}$, $D_{0.9}$, span for nonprefilming atomiser

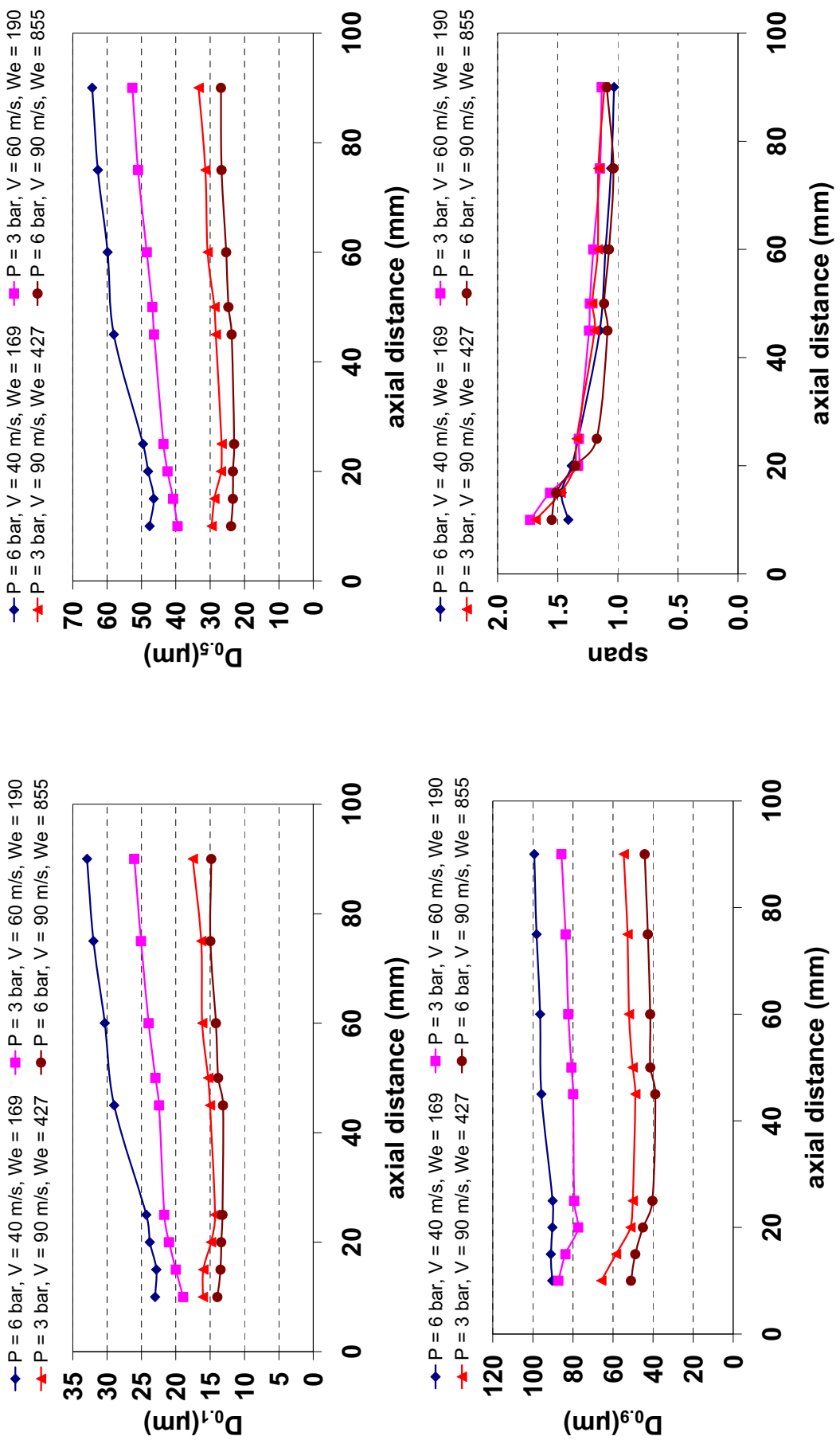

Fig. 4-8 Effect of operating conditions on $D_{0.1}$, $D_{0.5}$, $D_{0.9}$, span for 4mm prefilming atomiser

4.2.4 Effect of liquid flow rate

Measurements are performed to observe the effect of liquid mass flux (liquid loading) on global SMD for the 4 mm prefilming atomiser. Figure 4.9 shows the effect of liquid flow rate on SMD. For most of the measurements discussed in this present chapter the liquid flow rate is 2.91 g/s which corresponds to a liquid velocity of 1m/s at the entrance of the atomiser slit at liquid loading of 242 g/s/m. As can be observed, as the liquid flow rate increases the SMD increases and reaches a peak value at 2 g/s. Further increase in liquid flow rate decreases the SMD. At low liquid flow rates, the liquid sheet formed on the prefilming surface is thin. The liquid sheet reaches the prefilmer edge and produces finer droplets. As the liquid flow rate is increased thicker sheet is formed on the prefilming surface and produces bigger droplets. At high liquid flow rates, the interaction of liquid sheet and surrounding air stream increases due to the increase in differential pressure across the atomiser. The differential pressure produces surface waves causing high level of surface stripping. Surface stripping usually corresponds to smaller SMD's. The amount of liquid mass that strips off from the surface of the liquid sheet increases as the liquid flow rate increases beyond 2 g/s.

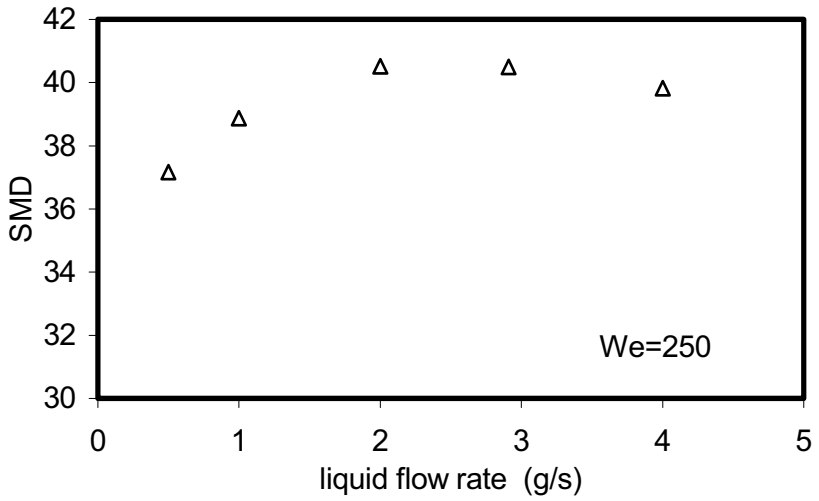

Fig. 4-9 Effect of liquid flow rate on GSMD

4.2.5 Effect of static pressure and air velocity on SMD

Figure 4.10 shows the effect of static pressure and air velocity on the global SMD characteristics of the spray for both atomisers at various operating conditions at an axial location of z = 90 mm and constant liquid velocity of 1 m/s. As can be observed, an increase in static pressure of air decreases the SMD of the spray for both atomisers. The slope of the curves indicates that the effect of static pressure on SMD is more dominant for the nonprefilming atomiser at lower pressures than for the prefilming atomiser. At higher static pressures, the effect of static pressure is more dominant for

the prefilming atomiser than for the nonprefilming atomiser. This is because the static pressure influences the formation of ligaments and surface waves on the liquid sheet. At higher static pressures, as explained in Chapter 3, ligaments are finer and hence produce finer droplets. In case of prefilming atomiser at higher static pressures, there is a combined effect of finer ligaments and surface stripping. The air velocity has a similar effect as static pressure. A rise in air velocity decreases the SMD. The effect of air velocity is more dominant than the static pressure. This indicates that the momentum of air plays a crucial role in the atomisation in airblast atomisers as also reported in the literature [47]. The slopes of the curves again indicate that the effect of air velocity is higher for the prefilming atomiser than for the nonprefilming atomiser. As discussed in Chapter 3, the air velocity has a predominant influence on liquid sheet breakup due to the increased momentum exchange at higher velocities. From the earlier discussions it is evident that the operating conditions have a similar effect for both atomisers which are to be expected. However, the magnitude of influence of these parameters varies in proportion for both the atomisers. The independent effect of these parameters on global SMD is discussed in next section.

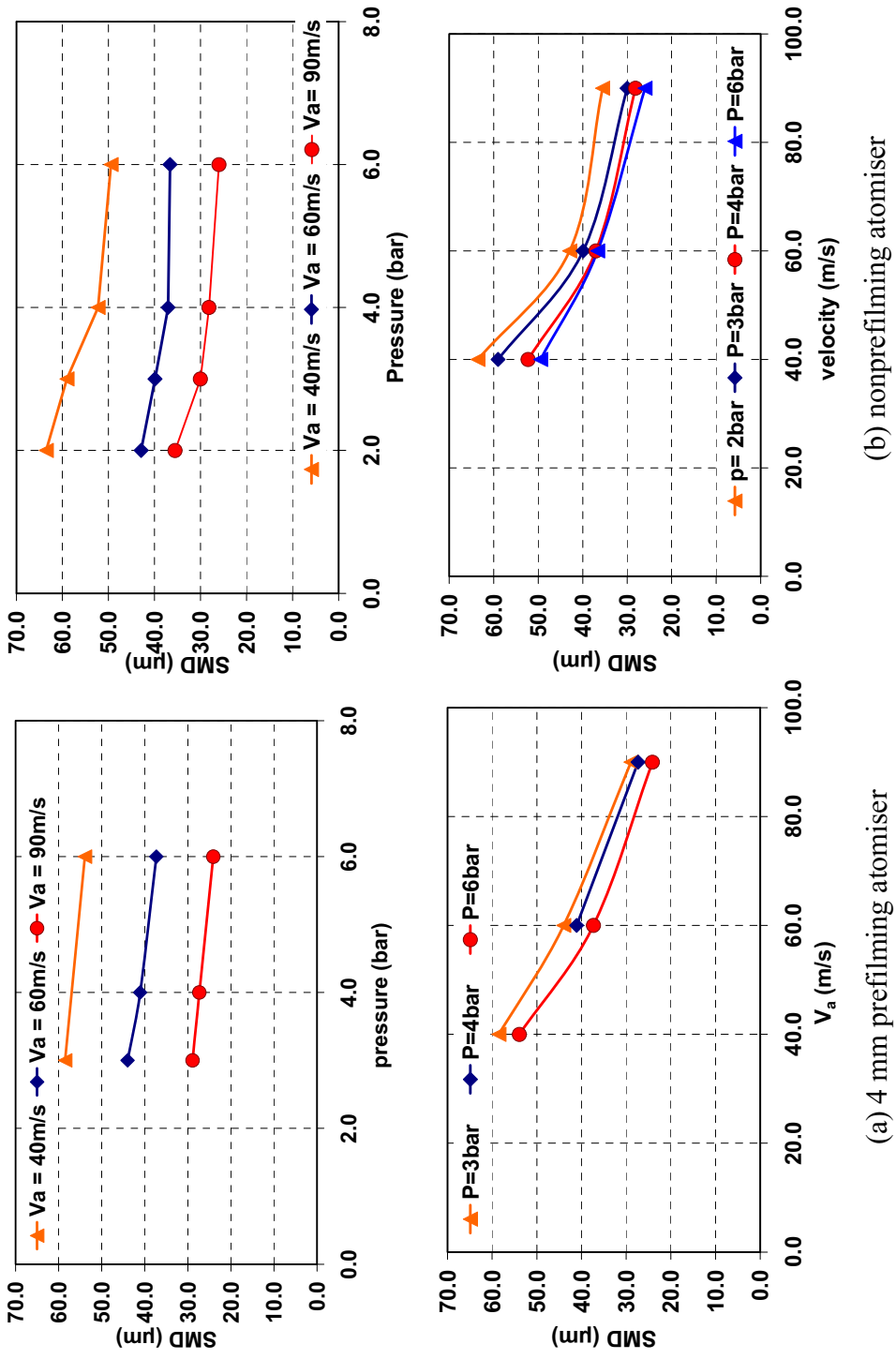

(a) 4 mm prefilming atomiser (b) nonprefilming atomiser

Fig. 4-10 Effect of static pressure and air velocity on GSMD

4.2.6 Effect of Weber number on SMD

Figure 4.11 shows the combined effect of both pressure and velocity on SMD as a function of Weber number. During the experiments, the surface tension σ of the liquid is constant as the measurements are performed at ambient temperature. The parameters that are varied are only pressure and air velocity as explained before. Hence the Weber number defined here is basically the change of momentum flux of air. The nonprefilming atomiser performs better at low Weber number (We < 450) conditions in comparison with the prefilming atomiser. At lower Weber numbers, in prefilming atomisers, the surface waves produce a thicker liquid sheet at the prefilmer edge. The lack of sheet oscillations tends to reduce the momentum exchange between the liquid and air and hence produces larger droplets compared to nonprefilming atomiser. As the Weber number increases, the surface stripping becomes dominant in the case of prefilming atomiser with the liquid stripping off from the surface waves. The thickness of the liquid sheet reduces on the prefilming atomiser before it reaches the prefilmer edge. Beyond We > 450, the surface stripping is dominant and the prefilming atomiser performs better than the nonprefilming atomiser. It can be recollected that the dominance of surface stripping phenomena at higher Weber number is also identified in visualisation experiments (Chapter 3).

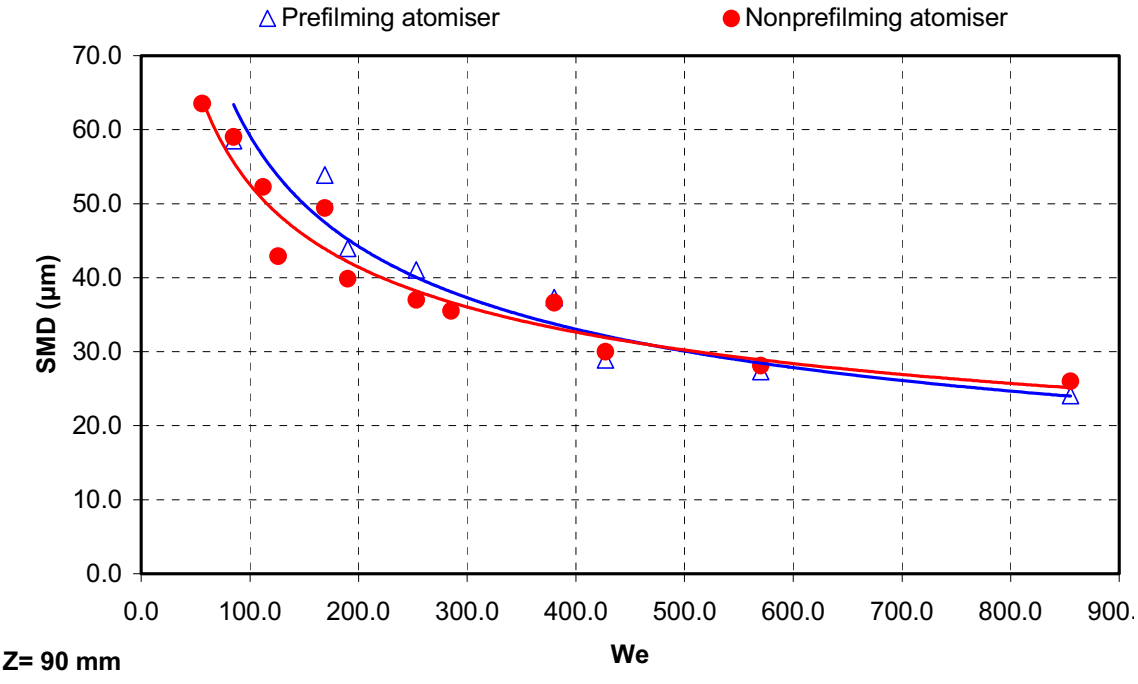

Fig. 4-11 Effect of Weber number on GSMD

The improved performance of the prefilming atomiser compared to nonprefilming atomiser at higher Weber numbers is also evident from the local SMD profiles in Figure 4.12 measured at an axial location of z = 90 mm. At lower Weber

number = 190 (P_a = 3 bar, V_a = 60 m/s), the X-profiles for nonprefilming atomiser show smaller droplets at the centre of the spray where the liquid volume flux is concentrated in comparison with prefilming atomiser. At the edges of the spray the droplets are bigger compared to prefilming atomiser. However, at the edges of the spray, the liquid volume flux is relatively less. At higher Weber number, We = 855 (P_a = 6 bar, V_a = 90 m/s), the surface stripping and thinning of the liquid sheet dominates in prefilming atomisers. Here also the edges of the spray have smaller droplets for the prefilming atomiser compared to the nonprefilming atomiser. (The width of the spray for these operating conditions is ~ x= -5 mm to x= 5 mm based on Fig. 4.6)

The edges on both sides of the spray have droplets almost of equal size. The smaller droplets tend to spread out to the edges of the spray leaving bigger droplets in the centre of the spray. Hence, the individual effect of surface stripping on formation of smaller droplets could not be made. Even in the near-field, at closer axial locations of z= 10 mm not shown in the figure, the profiles are similar to Figure 4.12 on the side of the prefilming surface (on the –x direction). It has to be noted that the transmitting optics is positioned on the side of the prefilming surface. The reliability of PDA measurements in questionable on the (+x direction) as the beam have to pass through the dense spray and beams have to pass through the dense spray and the measurements are biased towards bigger droplets.

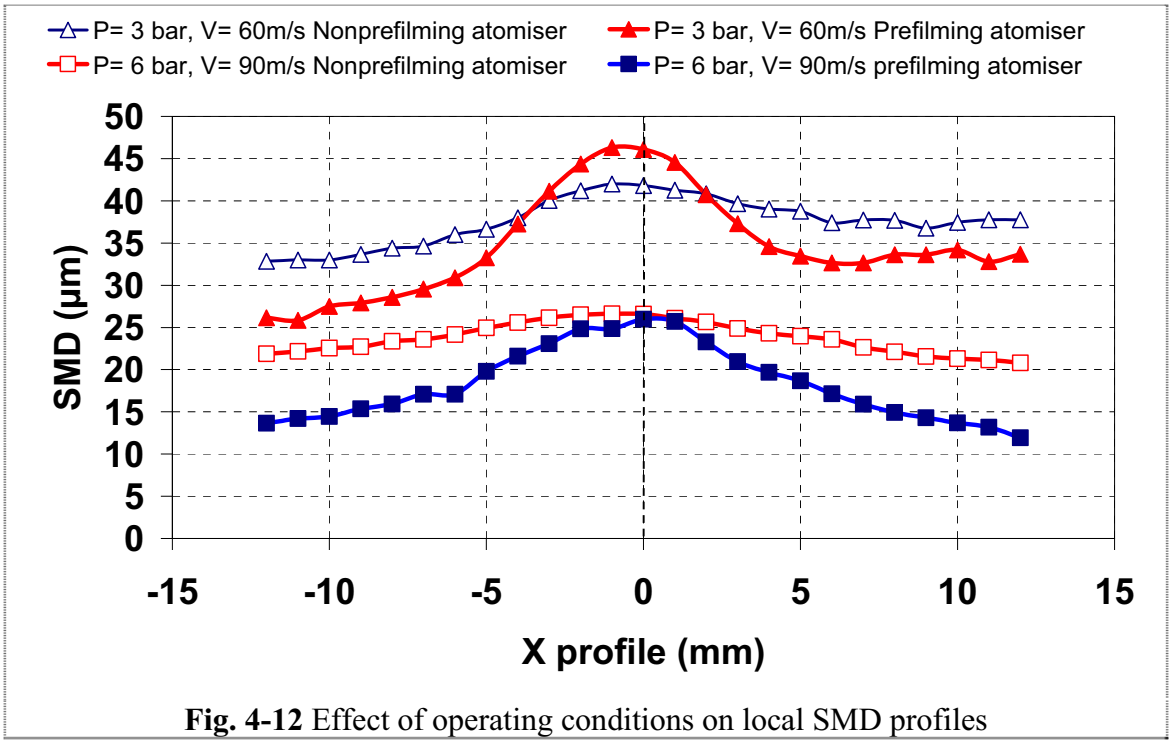

Fig. 4-12 Effect of operating conditions on local SMD profiles

4.2.7 Correlations for SMD

As discussed in Chapter 1, there are several correlations for SMD available in the literature as a function of operating parameters. Most of the correlations are specific to an atomiser design and do not follow similarity laws. The reason is due to the complexity of two-phase flow problem where the interaction of several parameters is interdependent on each other.

From the dependence of SMD over Weber number in the present study, it is evident that there is a strong influence of momentum flux of air, $\rho_a u_a^2$, and both density of air and air velocity should have a similar power law influence on SMD. In Lefebvre [48], the power of the momentum flux is given as -0.5. The regression analysis from our experimental data shows that the momentum flux term has a functional dependence of -0.42 for the 4mm prefilming atomiser and -0.3 for the nonprefilming atomiser. As can be recalled, the primary breakup of liquid sheets has shown the influence of momentum flux of air. The difference in power of momentum flux of air for both atomisers can be attributed to the role of secondary atomisation. The Brandt's equation considers the effect of density and air velocity on SMD independently. Independent regression analysis of density and air velocity show the effect of density of air to be -0.15 & -0.26 for nonprefilming and 4 mm prefilming atomiser respectively. The effect of air velocity has more influence and the dependency is -0.75 & -1.0 for nonprefilming and 4 mm prefilming atomiser respectively.

The equation can be rewritten as

$$SMD \propto (\rho_l . V_l . t_l^*)^{0.3} \frac{\sigma^{0.5}}{(\rho_a^{0.15} u_a^{0.75})} \qquad \text{Eq. 4-5}$$

for nonprefilming atomiser,

$$SMD \propto (\rho_l . V_l . t_l^*)^{0.3} \frac{\sigma^{0.5}}{(\rho_a^{0.26} u_a)} \qquad \text{Eq. 4-6}$$

for 4 mm prefilming atomiser,

where *SMD* is the Sauter mean diameter (μm), ρ_l is the density of liquid (kg/m³), V_l is velocity of liquid (m/s) calculated from mass flow rate of liquid, t_l^* is the effective thickness of the liquid sheet (μm), σ is the surface tension between liquid and air (N/m), ρ_a is the density of air (kg/m³) and u_a is the velocity of air (m/s). Liquid loading is kept constant in the present experiments and in obtaining these correlations. The

thickness of the liquid sheet is 300 μm. For the nonprefilming atomiser t_l^* can be taken as a constant value of 300 μm. For the prefilming atomiser t_l^* is the effective thickness of the liquid film at the prefilmer edge. This seems to be dependent on Weber number and the prefilmer length. However, this has to be verified experimentally. The effect of variation of prefilmer length on SMD is beyond the scope of this thesis. The following table shows that experimental data match with the correlations by considering a constant value of t_l^* = 300 μm. Table 4.3 shows GSMD from experimental data with the calculated GSMD from the above correlations. The comparison shows a good match between experimental and correlations.

4 mm prefilming atomiser

ρ_a	V_a	measured SMD	calculated SMD
3.87	60.0	38.74	37.82
5.16	60.0	35.14	35.10
7.74	60.0	32.07	31.58
3.87	90.0	25.20	25.21
5.16	90.0	24.17	23.40
7.74	90.0	21.48	21.06

nonprefilming atomiser

ρ_a	V_a	measured SMD	calculated SMD
3.87	40.0	49.66	51.15
5.16	40.0	47.31	48.99
7.74	40.0	48.15	46.10
2.6	60.0	40.18	40.06
3.87	60.0	36.55	37.74
5.16	60.0	34.65	36.15
7.74	60.0	33.55	34.01
2.60	90.0	29.75	29.56
3.87	90.0	27.37	27.84
5.16	90.0	26.02	26.67
7.74	90.0	24.04	25.09

Table 4-3 Comparison of experimental data and correlations

CHAPTER 5

SUMMARY AND CONCLUSIONS

The present work described the experimental work carried out during the process of development of airblast atomisers for gas turbine combustors. The first major task of this work is to study the breakup mechanism of a two dimensional liquid sheet of Kerosene Jet A1 fuel in a prefilming airblast atomiser and compare it with the liquid sheet breakup mechanism in nonprefilming airblast atomisers under elevated pressure conditions. It is found that the primary breakup mechanism of liquid sheet on prefilming surfaces is considerably different from the well established theories on classical liquid sheet breakup. To understand the fundamental aspects of liquid sheet behaviour on prefilming surface, experiments are conducted at low operating conditions. New insights are observed into the physics of liquid sheet behaviour. Phenomena like "surface wave plunging" and "surface stripping" on the liquid surface are observed. Surface waves similar to gravity waves are formed on the surface of the liquid sheet on the prefilming surface. The propagation of these waves appears to be similar to gravity waves. Surface stripping of the liquid sheet is observed on the prefilming surface at high Weber numbers. The operating conditions where surface stripping occurs correspond to realistic operating conditions in gas turbines. The liquid sheet breakup in nonprefilming atomisers follows the usual breakup of ligaments into clusters and droplets.

The instability of the liquid sheet at the atomiser slit is also investigated. It is found that the liquid does not fill up the entire atomiser slit and the liquid sheet breaks chaotically in nonprefilming atomisers. The liquid sheet is rather more stable for prefilming atomisers. Higher mass flow rate/liquid loading is required for nonprefilming atomiser to have a stable liquid sheet at high pressures when compared with prefilming airblast atomiser. The stability of the sheet influences the uniformity of fuel placement, mixing efficiency of spray and production of NO_x at realistic operating conditions.

Several aspects like the speed of surface wave propagation on prefilming surfaces, liquid sheet oscillation in case of nonprefilming airblast atomisers, breakup length and ligament spacing are quantified. The sheet oscillations are suppressed at higher operating conditions for prefilming atomisers. The width of the spray is more for a nonprefilming atomiser due to the oscillatory behaviour of the liquid sheet. An effort was made to quantify the liquid sheet thickness on the prefilming surface by imaging techniques. It is found that thickness of the liquid sheet varies on the prefilming surface. It can reach twice the initial liquid sheet thickness at low operating conditions. A maximum liquid sheet thickness of ~600 μm is observed at We = 32 even though the

initial liquid sheet thickness is 300 μm. The minimum amplitude is ~100 μm. The variation of sheet thickness is due to the propagation of surface waves. At higher operating conditions, due to surface stripping the maximum liquid thickness observed is ~ 378 μm and minimum thickness is ~90 μm. The thickness of the edge of the prefilming surface also influences the breakup of the liquid sheet. The liquid mass accumulates at the prefilmer edge due to the Coanda effect and liquid fuel gets accumulated at the edge. The storage mechanism at the edge affects the phase of the liquid mass entering the combustion zone.

PIV is adopted to obtain the velocity flow field of the liquid phase in the near-field of the atomisers where the presence of large structures hinders the measurements by other non-intrusive techniques. PIV results indicate that the surface of the liquid sheet propagates 3-5 m/s and ligaments travel at 5-10 m/s at We = 48. PIV velocity measurements are compared with PDA measurements and a close agreement in the measurements has been established. Application of PIV seems to be a promising measurement technique in the near-field of the atomiser. These parameters are expected to provide information for simulations.

The second task of this work is to characterise the spray emerging from the 4 mm prefilming and nonprefilming atomisers. PDA measurements are carried at various operating conditions to measure characteristic diameters, fuel placement, dispersion of the spray and to analyse whether there the parameters that govern the primary breakup mechanism influence the final droplet size. The results show that the new atomiser design provides a highly two dimensional spray which can be used for both basic studies and characterising atomisers. The effect of positioning of transmitting optics on quality of measurements is discussed. PDA measurements reveal that the measurements in the near field are prone to bias due to the high density of the spray. Beyond the centre of the spray validation rates are very low and the effects of beam steering are high. The analysis shows that at an axial location of z = 90 mm is an ideal location for comparison of atomisers. The spray dispersion analysis shows that there is no significant dispersion of spray for both atomisers and the dispersion is purely due to turbulence generated in the wake of the atomiser and in the test section. Beyond the axial location of z = 90 mm the volume flux is well captured by PDA measurements.

The comparison of GSMD made at z = 90 mm, shows that at low Weber numbers, the performance of the nonprefilming atomiser is better than the prefilming atomisers. Beyond Weber number 450, the performance of prefilming atomiser is better. This is due to surface stripping. This corresponds to the idle operating condition of gas turbine combustor. The results are in agreement with the flow visualisation experiments. The difference in GSMD in very marginal in the range of operating conditions tested and fall into the error range for a PDA system. However, as explained the surface

stripping phenomena is more predominant at higher operating conditions and prefilming atomiser has tendency to produce finer spray at higher operating conditions. There is another advantage of using a prefilming atomiser. The liquid film is stable at the slit of the atomiser and forms a closed film even at higher operating conditions.

Considering the above advantages of prefilming atomiser over nonprefilming atomiser, it is recommended to use prefilming atomiser.

RECOMMENDATIONS FOR FUTURE WORK

The present experimental study does not include swirl components of air which are present in practical airblast atomisers for gas turbine applications. The effect of swirl on the liquid sheet breakup and atomisation characteristics will be interesting to study. It can have significant effect on the prefilming atomiser producing a stable liquid film, with finer spray and mixing of spray with the free stream. Due to complicated design features of the atomisers only a prefilming atomiser with 4 mm prefilming surface and a nonprefilming atomiser are studied. The effect of variation of length of the prefilming surface can have a significant influence on the atomisation characteristics of the atomiser. In the present study the liquid loading is kept constant with the thickness of the liquid sheet to be 300 μm and liquid mass flow rate of 2.91 g/s giving the effect of the velocity of the liquid sheet at the slit of the atomiser to be ~1 m/s. The combination of liquid sheet thickness and the mass flow rate of liquid is another interesting feature that can be studied for stability analysis of liquid sheet at the slit of the atomiser. In realistic operating conditions the static temperature of the air is ~850 K. However in the present experimental studies, ambient temperature is chosen to limit the parameters effecting the liquid sheet breakup. For spray characterisation this has to be taken into account as this will effect the surface tension of the liquid and hence the atomisation quality.

And lastly, advanced image processing techniques can be applied to obtain size distribution of large individual non-spherical structures. PIV technique along with the particle sizing techniques can be applied to obtain size-velocity correlation of non-spherical particles providing information in the near-field of the atomisers.

REFERENCES

1. AGGARWAL, S. K.: *Dispersion of Evaporating Droplets in a Swirling Axisymmetric Jet*. AIAA Journal, 37(12): 1578-1587, 1999.

2. ARAI, T. and HASHIMOTO, H.: *Behaviour of Gas-Liquid Interface on a Liquid Film Jet (instability of liquid film jet in a co-current gas stream).* Bulletin of JSME, 28(245): 2652-2659, 1985.

3. BACHALO, W. D., HESS, C. F. and HARTWELL, C.A.: *An Instrument for Spray Droplet Size and Velocity Measurements*. Journal of Fluids Engineering, 102: 798-806, October, 1980.

4. BEHRENDT, T.: *Strömung und Verbrennung in einem neuen Düsenkonzept für die magere Vormischverbrennung in Fluggasturbinen.* DLR Forschungsbericht 2003-14, 2004. ISSN 1434-8454

5. BEHRENDT, T. and HASSA, C.: *Investigation of the Spray Dynamics of Aero engine Fuel Injectors under Atmospheric and Simulated Pressure Conditions.* Symposium on Advanced Non-Intrusive Instrumentation for Propulsion Engines, October, 1997.

6. BEHRENDT, T., HEINZE, J. and HASSA, C.: *Optical Measurements of the Reacting Two-Phase Flow in a Realistic Gas Turbine Combustor at Elevated Pressures*. ILASS Europe 2000, Darmstadt, Germany, 2000.

7. BERTHOUMIEU, P. and CARENTZ, H.: *Experimental study of a Thin Planar Liquid Sheet Disintegration.* ICLASS -2000, July, 2000.

8. BERTHOUMIEU, P., CARENTZ, H. and MULLER, A.: *Video Techniques Applied to the Characterization of Liquid Sheet Breakup.* 9th International Symposium on Flow Visualisation: 28.1-28.6, 2000.

9. BERTHOUMIEU, P.: *Désintégration de nappe liquide*. Fiche D'Identification due document ONERA, N°RT 1/05684-01F DMAE, 2001.

10. BLÜMCKE, EICKHOFF, H. and HASSA, C.: *Dispersion of Monosized Droplets in a Turbulent Swirling Flow.* ICLASS-88, 1988.

11. BRANDT, M.: *Liquid and Gaseous Fuel Measurements in a Premix Duct.* ILASS-Europe 95, 33-42March, 1995.

12. BRANDT, M., GUGEL, K.O. and HASSA, C.: *Experimental Investigation of the Liquid Fuel Evaporation in a Premix Duct for Lean Premixed and Prevapourised Combustion.* Journal of Engineering for Gas Turbines and Power, 119: 815-821, October, 1997.

13. CHIGIER, N. A.: *The Physics of Atomisation.* ICLASS 91, July, 1991.

14. CLIFT, R., GRACE, J. R. and WEBER, M. E.: *Bubbles, Drops and Particles.* Academic Press, ISBN-0-12-176950-X, 1978.

15. CRAPPER, G. D. and DOMBROWSKI, N.: *A Note of the Effect of Forced Disturbances on the Stability of Thin Liquid Sheets and on the Resulting Drop Size.* International Journal of Multiphase Flow, 10(6): 731-736, 1984.

16. CRAPPER, G. D., DOMBROWSKI, N., JEPSON, W. P. and PYOTT, G., A.: *A Note on the Growth of Kelvin-Helmoltz Waves on Thin Liquid Sheets.* Journal of Fluid Mechanics, 57(4): 671-672, 1973.

17. DANTEC MEASUREMENT TECHNOLOGY: *DANTEC PDA User's Manual,* 1992. Publ. No. 9150 A 9206.

18. DOMBROWSKI, N. and JOHNS, W. R.: *The Aerodynamic Instability and Disintegration of Viscous Liquid Sheets*. Chemical Engineering Science, 18: 203-214, 1963.

19. DOMBROWSKI, N. and FRASER, R. P.: *A Photographic Investigation into the Disintegration of Liquid Sheets,* 247 (9): 101-130, 1954.

20. DRISCALL, K. D, Sick. V. and Gray, C.: *Simultaneous Air/Fuel-Phase PIV Measurements in a Dense Fuel Spray.* Experiments in Fluids, 35(1), 112-115, 2003.

21. EDWARDS, C. F. and MARX, K. D.: *Analysis of the Ideal phase-Doppler System: Limitations Imposed by the Single-Particle Constraint*. Atomisation and Sprays, 2: 319-366, 1992.

22. EINSTEIN, A.: *Elementare Theorie der Wasserwellen und des Fluges.* Naturwissenschaften, 4: 509, 1916.

23. EL SHANAWANY, M. S. M. R., LEFEBVRE, A. H.: *Airblast Atomisation: The Effect of Linear Scale on Mean Drop Size.* Journal of Energy, 4(4): 184-189, 1980.

24. EROGLU, H. and CHIGIER, N.: *Coaxial Atomiser Liquid Intact Lengths*. Physics of Fluids A, 3(2): 303-308, 1991.

25. EROGLU, H. and CHIGIER, N.: *Initial Drop size and velocity Distribution for Airblast Coaxial Atomisers.* Journal of Fluids Engineering, 453-459, September , 1991.

26. FEYNMAN P. R., LEIGHTON, R. B., MATTHEW, S.: *Lectures on Physics.* Addison-Wesley Publishing Company, Inc, ISBN 81-85015-83-X, 1964

27. FLÖGEL, H. H.: *Modifizierte Laser-Doppler Anemometrie zur simultanen Bestimmung von Geschwindigkeit und Größe einzelner Partikeln.*-Ber. VDI Reihe 3, 140, VDI Verlag Düsseldorf, 1987.

28. FRASER, R. P.: *Liquid Fuel Atomisation.* 6th Symposium on Combustion, New York: 687-701, 1957.

29. FRASER, R. P. and EISENKLAM, P.: *Research into the Performance of Atomisers for Liquids.* AIChE Journal, 7: 52-68, 1953.

30. FRASER, R. P., EISENKLAM, P., DOMBROWSKI, N. and HASSON, D.*: Drop Formation from Rapidly Moving Liquid Sheets*. A.I.Ch.E. Journal, November: 672-680, 1962.

31. HAENLEIN, A.: *Disintegration of Liquid Jet*, NACA TN 659, 1932.

32. HAGERTY, W. W. and SHEA, J. F.: *A study of the Stability of Plane Fluid Sheets.* ASME Applied Mechanics, December: 509-514, 1955.

33. HASSA. C., HEINZE J., RACKWITZ L. and DOERR, T.: *Validation Methodology for the Development of Low Emission Fuel Injectors for Aero-Engines.* ISABE, Munich, Germany, 2005-1143, 2005.

34. HESPEL, J. M., BRUNET, Y. and DYMENT, A.: *Liquid Sheet and Film Atomization: A Comparative Experimental Study*. Experiments in Fluids, 19: 388-396, 1995.

35. HETSRONI, G.: *Particles-Turbulence Interaction*. International Journal of Multiphase Flow. 15(5): 735-746, 1989.

36. HIMMELSBACH, J., NOLL, B. and WITTIG, S.: *Experimental and Numerical Studies of Evaporating Wavy Fuel Films in Turbulent Air Flow.* International Journal of Heat and Mass Transfer, 37(8): 1217-1226, 1994.

37. HINZE, J. O.: *Fundamentals of the Hydrodynamic Mechanism of Splitting in Dispersion Processes*. A.I.Ch. E. Journal, 1(3): 289-295, 1955.

38. HURLBURT, E. T. and NEWELL, T. A.: *Optical Measurements of Liquid Film Thickness and Wave Velocity in Liquid Film Flows.* Experiments in Fluids, 21, 357-362, 1966.

39. ICAO Annex 16. *International Standards and Recommended Practices, Environmental Protection*, 2, Aircraft engine emissions. 2nd Edition, 1993.

40. JASUJA, A. K.: *Atomisation of Crude and Residual Oils.* ASME Journal of Fluid Engineering and Power, 101(2): 250-258, 1979.

41. JASUJA, A. K.: *The Role of Air and Fuel Properties in Mean Drop Size Correlations for Airblast Atomised Gas Turbine Sprays.* ILASS-Europe: 31-36, 2004.

42. JASUJA, A. K. and LEFEBVRE, A. H.: *Influence of Ambient Pressure on Drop-size and Velocity Distribution in Dense Sprays.* 25th Symposium (international) on Combustion/The Combustion Institute: 345-352, 1994.

43. JEANDEL, X. and DUMUOUCHEL, C.: *Influence of the Viscosity on the Linear Stability of an Annular Liquid Sheet.* International Journal of Heat and Fluid Flow, 20: 499-506, 1999.

44. KENYON, E. KERN: *Capillary Waves Understood by an Elementary Method.* Journal of Oceanography, 54: 343-346, 1998.

45. KENYON, E. KERN and SHERES, D.: *Einstein's Gravity Wave Method applied to a Two-Layer Fluid with Current Shear*, Physics Essays, 10(1): 55-63, 1997.

46. LAZARO, B. J. and LASHERAS, J. C.: *Particle Dispersion in a Turbulent, Plane, Free Shear Layer,* Physics of Fluids A, 1(6): 1035-1044, 1989.

47. LEFEBVRE, A., H.: *Energy Considerations in Twin-Fluid Atomisation.* Journal of Engineering for Gas Turbines and Power, 114: 89-95, 1992.

48. LEFEBVRE, A. H.: *Atomisation and Sprays*. Hemisphere Pub., ISBN- 0-89116-603-3, 1989.

49. LEFEBVRE, A. H.: *Airblast Atomisation*. Prog. Energy Combustion Science, 6: 233-261, 1980.

50. LIN, S. P.: *Absolute and Convective Instability of a Liquid Sheet.* Journal of Fluid Mechanics, 220, 673-689, 1990.

51. LOZANO, A., CALL, C. J., DOPAZO, C. and GARCIA-OLIVARES, A.: *Experimental study of the atomisation of a planar liquid sheet.* Atomization and Sprays, 6 : 77-94, 1996.

52. MAEDA, T., MORIKITA, H., HISHIDA, K. and MAEDA, M.: *Determination of Effective Measuring Area in a Conventional Phase-Doppler Anemometry,* 8th International Symposium on Application of Laser Techniques to Fluid Mechanics, Lisbon, 1996.

53. MANSOUR, A. and CHIGIER, N.: *Dynamics Behaviour of Liquid Sheets*. Physics of Fluids A, 3(12): 2971-2980, 1991.

54. MAYER, E.: T*heory of Liquid Atomisation in High Velocity Gas Streams*. ARS Journal, December: 1783-1785, 1961.

55. MEHRING, C. and SIRIGNANO, W. A.: *Capillary Stability of Modulated Swirling Liquid Sheets.* Atomisation and Sprays, 14: 397-436, 2004.

56. MEIER, U., HEINZE, J., and HASSA, C.: *Response of Spray and Heat Release to Forced Air Flow Fluctuations in a Gas Turbine Combustor at Elevated Pressure.* Proceedings of 2007 ASME Turbo Expo Power for Land, Sea and Air, Montreal, Canada, 2007.

57. MUGELE, R.A. and EVANS, H. D.: *Droplet Size Distribution in Sprays.* Industrial and Engineering Chemistry, 43: 1317-1324, 1951.

58. OHNESORGE, W.: *Formation of Drops by Nozzles and the Breakup of Liquid Jets.* Z. Angew. Math. Mech., 16: 355-358, 1936.

59. PARK, J., KANG Y. HUH, XIANGUAO LI and RENKSIZBULUT, M.: *Experimental Investigation on Cellular Breakup of a Planar Liquid Sheet from an Air-blast Nozzle*. Physics of Fluids, 16(3): 625-632, 2004.

60. PERLIN, M. and SCHULTZ, W. W.: *Capillary Effect on Surface Waves.* Annual Review of Fluid Mechanics, 32: 241-274, 2000.

61. PITCHER G., WIGLEY, G. and SAFFMAN, M.: *Sensitivity of Drop Size Measurements by Phase Doppler Anemometry to Refractive Index Changes in Combusting Fuel Sprays.* Proceeding of 5th Int. Symposium on Application of Laser Techniques to Fluid Mechanics, Lisbon, Portugal, 1990.

62. RACHNER, M.: *Die Stoffeigenschaften von Kerosin Jet A1.* Mitteilung 98-01, 1998. ISSN 1434-8462.

63. RACHNER, M., BECKER, J., HASSA, C. and DOERR, T.: *Modelling of the Atomisation of a Plain Liquid Fuel Jet in Crossflow at Gas Turbine Conditions.* Aerospace Science and Technology. 6: 495-506, 2002.

64. RANGEL, R. H. and SIRIGNANO, W.A.: *Nonlinear Growth of Kelvin-Helmholtz Instability: Effect of surface tension and density ratio*. Physics of Fluids, 7: 1845-1855, 1988.

65. RANGEL, R. H. and SIRIGNANO, W. A.: *The Linear and Nonlinear Shear Instability of a Fluid Sheet*. Physics of Fluids A, 3(10): 2392-2400, 1991.

66. RAYLEIGH: *On the instabilities of Jets.* Proceedings London Mathematical Society, 10: 4-13, 1878.

67. RIZK, N. K. and LEFEBVRE, A. H.: *The Influence of Liquid Film Thickness on Airblast Atomization.* Trans. ASME Journal of Engineering Power, 102: 706-710, 1980.

68. RIZKALLA, A. and LEFEBVRE, A. H.: *The Influence of Air and Liquid Properties on Air Blast Atomisation*. ASME Journal of Fluids Engineering, 97(3): 316-320, 1975.

69. ROSIN, P. and RAMMLER, E.: *The Laws Governing the Fineness of Powdered Coal.* The Institute of Fuel, October: 29-36, 1933.

70. ROSSKAMP, H., WILLMANN, M., MEISL, J., MEIER, R., MAIER, G. and WITTIG, S.: *Effect of the Shear Driven Liquid Wall Film on the Performance of Prefilming Airblast Atomisers*, Gas Turbine Symposium and Exposition, Sweden, 1998.

71. SAFFMAN, M.: *Automatic Calibration of LDA Measurement Volume Size.* Applied Optics, 26(13): 2592-2597, July, 1987.

72. SAFFMAN, M., BUCHHAVE, P. and TANGER, H.: *Simultaneous Measurement of Size, Concentration and Velocity of Spherical Particles by a Laser Doppler Method.* Proceedings of 2nd International Symposium on Applications of Laser Anemometry to Fluid Mechanics, Lisbon, 1984.

73. SANKAR, S. V. and BACHALO, W. D.: *Performance Analysis of Various Phase Doppler Systems,* 4th International Congress on Optical Particle Sizing, Nürnberg, Germany, 1995.

74. SCHÖNE, F., BAUCKHAGE, K. and WRIEDT, T.: *Size of the Detection Area of a Phase-Doppler Anemometer for Reflecting and Refracting Particles*. Part. System. Characteristics, 11: 327-338, 1994.

75. SCHWEITZER, P. H.*: Mechanism of Disintegration of Liquid Jets.* Journal of Applied Physics, 8: 513-521, 1937.

76. SEAY, J., MCDONELL, V. and SAMUELSON, G.: *Atomization and Dispersion from a Radial Airblast Injector in a Subsonic Cross flow.* AIAA Joint Propulsion Conference and Exhibit, San Diego, July, 1995.

77. SENECAL, P. K.: *Modeling High-Speed Viscous Liquid Sheet Atomization*. International Journal of Multiphase Flow, 25: 1073-1097, 1999.

78. SHUELN, J. S., CHEN, L. D., and FAETH, G. M.: *Evaluation of a Stochastic Model of Particle Dispersion in a Turbulent Round Jet.* AIChE Journal, 29(1): 167-170, 1983.

79. SLEICHER, C. A.: *Maximum Stable Drop Size in Turbulent Flow*. A.I.Ch.E. Journal, 8(4): 471-477, 1962.

80. STAPPER, B. E., SOWA, W. A. and SAMUELSEN, G. S.: *An Experimental Study of the Effects of Liquid Properties on the Breakup of a Two-Dimensional Liquid Sheet*. Journal of Engineering for Gas Turbines and Power, 114(1): 39-45, 1992.

81. STERLING M. A. and SLEICHER, C. A.: *The Instability of Capillary Jets.* Journal of Fluid Mechanics, 68(3): 477-495, 1975.

82. SYNDER, W. H. and LUMLEY, J., L.: *Some Measurements of Particle Velocity Autocorrelation Functions in a Turbulent Flow.* Journal of Fluid Mechanics, 48: 41-71, 1971.

83. TYLER, F.: *Instability of Liquid Jets.* Philosophical Magazine. (London), 16, 504-518, 1933.

84. UMESH, C. B., GIULIANI, F. and HASSA, C.: *A Study of Planar Liquid Sheet Breakup of Prefilming Airblast Atomisers at High Ambient Air Pressures.* 20th Annual Meeting of the Institute of Atomisation and Spray systems (Europe), Orléans, 5th-7th September, 2005.

85. UMESH, C. B. and HASSA, C.: *Capillary Wave Propagation and Breakup of Planar Liquid Sheets in Pre- and Nonprefilming Airblast Atomisers*. ICLASS-2006, Kyoto, Japan, 2006

86. WEBER, C.: *Disintegration of Liquid Jets.* Z. Angew. Math. Mech, 11(2):136-159, 1931.

87. WILLIAMSON, C. H. K.: *Vortex Dynamics in the Cylindrical Wake.* Annual Review of Fluid Mechanics, 28: 477-539, 1996.

88. WITTIG, S., KOCH, R., SCHÄFER, O. and SCHOBER, P.: *Report on Validation Experiments for Film Flow on Plane Surfaces.* Deliverable Report, EU-contract No.: G4D-CT-1999-00075, Project No.: GRD1-1999-10325D3.8, 1999.

89. YORK, J. L., STUBBS, H. E. and TEK, M. R.: *The Mechanism of Disintegration of Liquid Sheets.* Transactions of ASME, October: 1279-1286, 1953.

90. YULE, A. J. and AKHTAR, S. W.: *Break-up of a Liquid Sheet Adjacent to a Single Air Stream.* ILASS-Europe 99, July, 1999.

91. YULE, A. J., VAMVAKOGLOU, K. and SHRIMPTON, J. S.: *Break-up of a Thin Flat Sheet Adjacent to a Wide, High Velocity Air Stream.* ILASS-Europe 98, July, 1998.

APPENDIX A

OPERATING CONDITIONS

	Reynolds number of Flow (Re)† x 10^5			
P_a (bar)	**V_a (m/s)**			
	30	**40**	**60**	**90**
2	2.4	3.2	4.8	7.2
3	3.6	4.8	7.2	10.8
4	4.8	6.4	9.6	14.4
6	7.2	9.6	14.4	21.6

Table A-1 Operating conditions tested

		Weber number of Flow $We = \frac{\rho_a u_a^2 t}{\sigma}$			
P_a (bar)	**ρ_a (kg/m^3)**	**V_a (m/s)**			
		30	**40**	**60**	**90**
2	**2.6**	32	56	127	285
3	**3.9**	48	84	190	428
4	**5.2**	63	113	253	570
6	**7.7**	95	169	380	855

at T = 275 K

Table A-2 Weber number at the operating condition

† **c**haracteristic diameter of test section d = (40 mm x 40 mm)$^{0.5}$= 56.56 mm.

gas turbine operating conditions [4]								
	Pressure (bar)	Temp (K)	Velocity (m/s)	μ (N.s) ($x10^{-5}$)	P (kg/m^3)	σ‡ (N/m) ($x10^{-3}$)	Re⌂	We
Start	36	850	98	3.97	14.76	2.32	20.6	18327
Idle	4.8	477	74	2.71	3.51	18.8	5.4	305
Take off	29.6	809	96.8	3.85	12.75	4.48	18.1	7994
Cruise	14.7	759	93.3	3.70	6.75	10.5	9.6	1678
Landing	18.4	709	90.3	3.54	9.04	8.79	13.1	2515

Table A-3 Typical gas turbine operating conditions

‡ Surface tension [N/m] of kerosene is calculated based on the equation [62] $\sigma(T) = 1.55 \cdot 10^{-5} \cdot (684.3 - T)^{1.222}$ at atmospheric pressure, where T [K] is the temperature of kerosene. In the present study, Kerosene in injected at atmospheric pressure and temperature. In realistic gas turbine conditions the temperature of kerosene depends on heat transfer from air. The effect of combustor pressure has influence on heat transfer rate. Considering these aspects, surface tension is calculated and hence has to be taken as an approximation. Weber number depends on surface tension of the liquid and hence has to be taken as an approximation.

⌂ Reynolds number is calculated based on characteristic diameter of test section.

APPENDIX B

TEST SECTION FLOW CONDITIONS

LDA measurements are performed to obtain the mean and RMS velocity profiles in the test section (cross-section 40 mm x 40 mm). The measurements are made by using the standard 2D PDA instrument with scattering angle of 18° and without diameter validation. For seeding the flow, an oil particle seeder is used which can produce particles of size less than 2 μm. The particle seeder is obtained from the Measurement group of Institute of Propulsion Technology.

The atomiser slit has a span of 12 mm and is positioned at the centre of the test section. Figure B.1 shows the axial mean velocities at the entrance of the test section at bulk velocity[⊗] of 50 m/s and static pressure of 4 bar. The measurements are performed 20 mm upstream of the atomiser at room temperature. The white rectangular box in the middle of the figure shows the atomiser slit position in the test section. Due to thick boundary layers at the walls of the test section, the velocity in the centre of the test section is relatively higher compared to the bulk velocity in the test section. The liquid sheet which emerges from the atomiser slit hence sees relatively higher velocity compared to the bulk velocity in the test section. The mean velocity in the centre of the test section is approximately 20% higher compared to the bulk velocity.

Figure B.2 shows the axial RMS velocities in the test section. The axial RMS velocity in the centre of the test section is ~5 m/s. The transverse mean velocity in the test section is ~ -1 m/s. The negative sign indicates the transverse velocity is towards the bottom of the test section. Figure B.3 shows the transverse RMS velocity in the test section. The transverse RMS velocity in the centre of the test section is ~ 2.5 m/s which is relatively lower compared to the axial RMS velocity.

[⊗] The bulk velocity is calculated based on the metered mass flow rate of air to the test section.

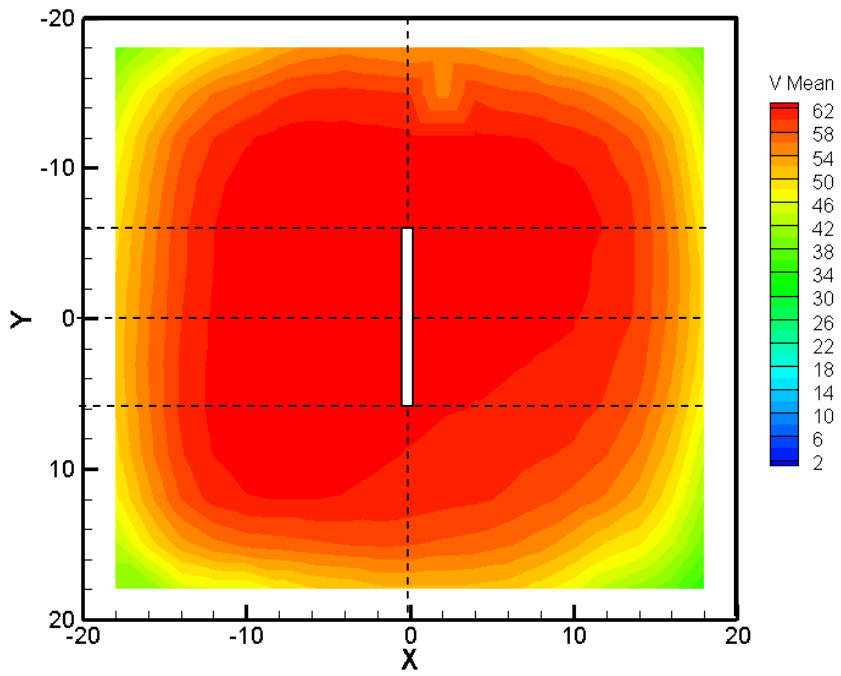

Fig. B-1 Axial mean velocity field at 20 mm upstream of the atomiser

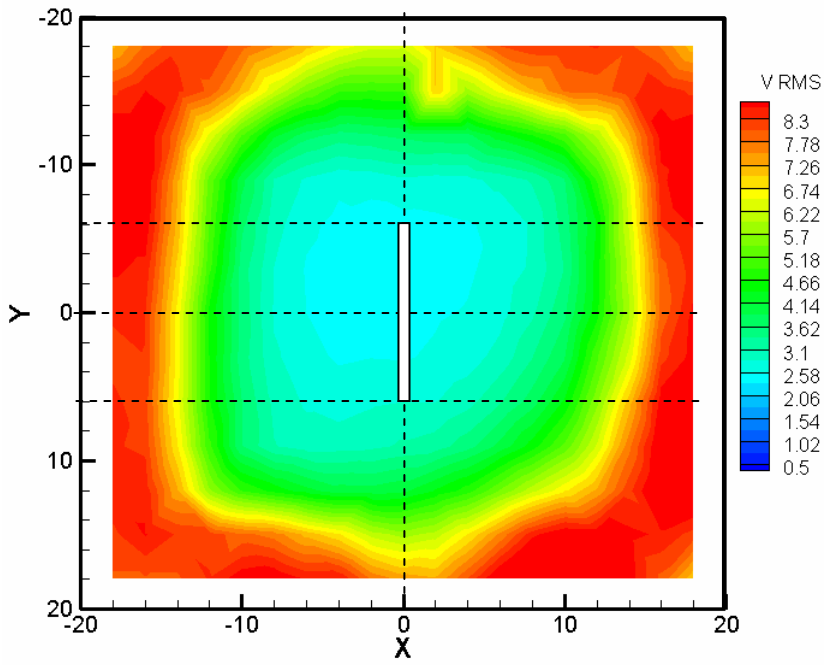

Fig. B-2 RMS velocity field at 20 mm upstream of the atomiser

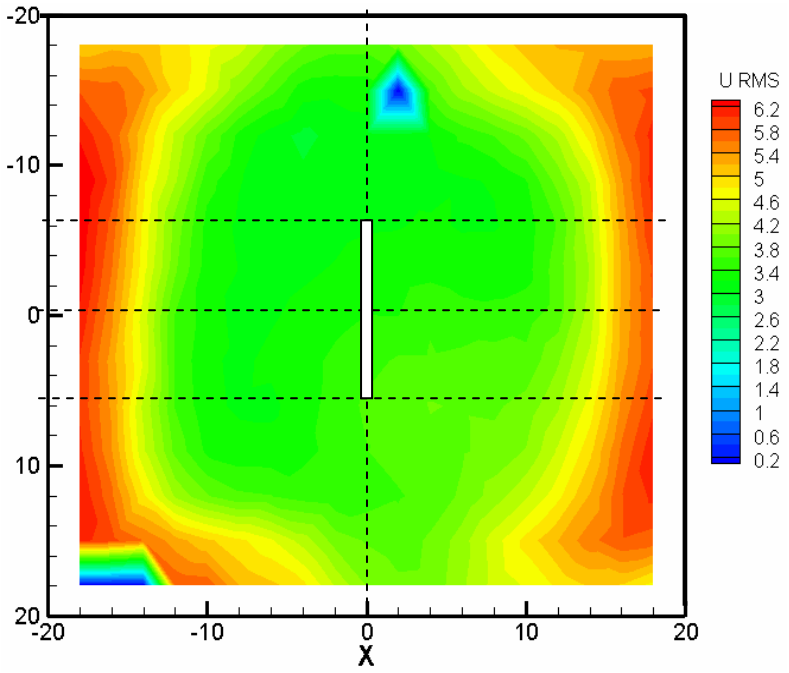

Fig. B.3 Transverse RMS velocity at 20 mm upstream of the atomiser

All the measurements and correlations in the dissertation are based on the bulk air velocity in the test section. Calibration data is performed to calculate the difference between the bulk velocity and the measured velocity from LDA measurements. The measured velocity is the average velocity in the test section from LDA measurements. Figure B.4 shows the bulk velocity and the measured velocity. The difference between the bulk velocity and the measured velocity is approximately 19%.

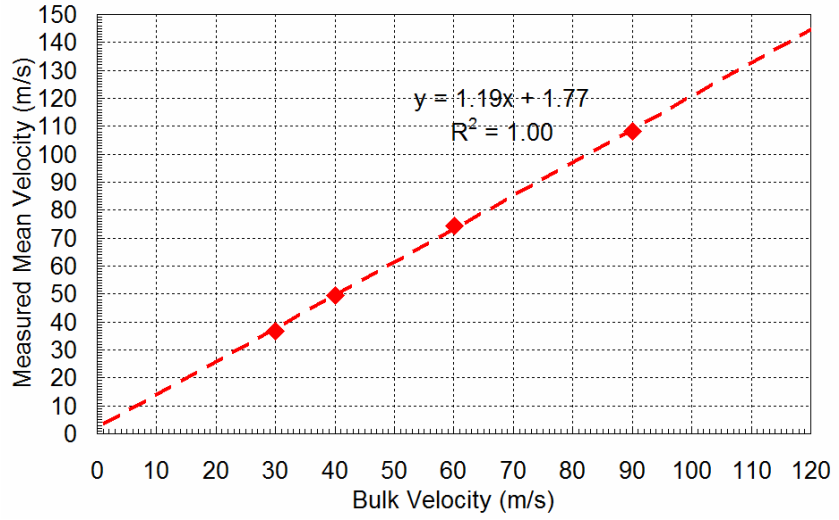

Fig. B.4 Difference between bulk velocity and measured velocity

APPENDIX C

SPANWISE VARIATION OF LOCAL SMD AND MEAN VELOCITY

Spanwise variation of SMD distribution

Figure C.1 shows the variation of local SMD along the span of the atomisers. As can be observed in Figure C.1(a) the SMD profiles are symmetric and the X-profiles from y = -4 mm to 4 mm lie over each other indicating the size distribution of the spray is symmetric and uniformly distributed along the span of the atomiser. The differences in the SMD profiles at the edges at +X edge and –X edge of X-axis profiles are due to few number of droplets acquired at a specified time-out limits for PDA data acquisition and also due to position of the transmitting optics of the PDA instrument. The details of the effect of transmitting are explained in detail in Appendix D. Figure C.1(b) shows the SMD distributions for the 4 mm prefilming airblast atomiser. It can be observed that there is a shift of ~1mm in the SMD profiles towards +X direction. As explained in section 4.1, Chapter 4, the shift in +X direction is due to the positioning error. Nevertheless the SMD profiles from y = -4mm to 4 mm are coincident indicating that kerosene is uniformly distributed along the span of prefilming airblast atomiser. For the prefilming atomiser, SMD's are smaller in –X direction compared to +X direction. The comparison of SMD profiles in –X direction compared for the atomisers in Figure C.1(a) and C.1(b) show that the SMD's are relatively smaller in –X direction for prefilming atomiser. This is due to the surface stripping phenomena occurring on the free surface of the liquid sheet that is exposed to free stream air. The details of effect of surface stripping on the SMD distribution are explained in Chapter 4.

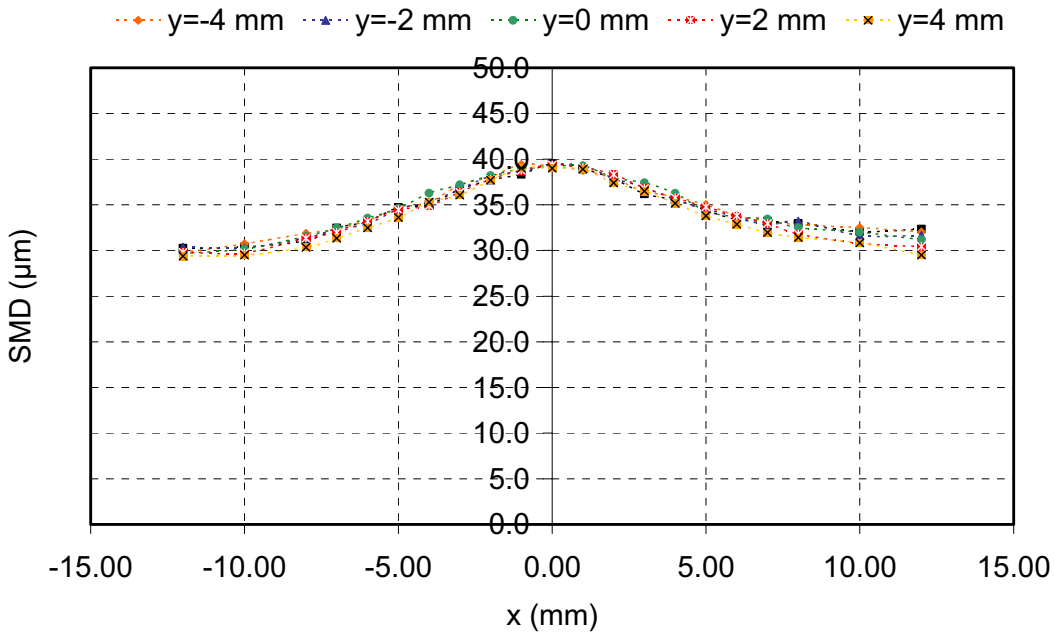

(a) nonprefilming airblast atomiser

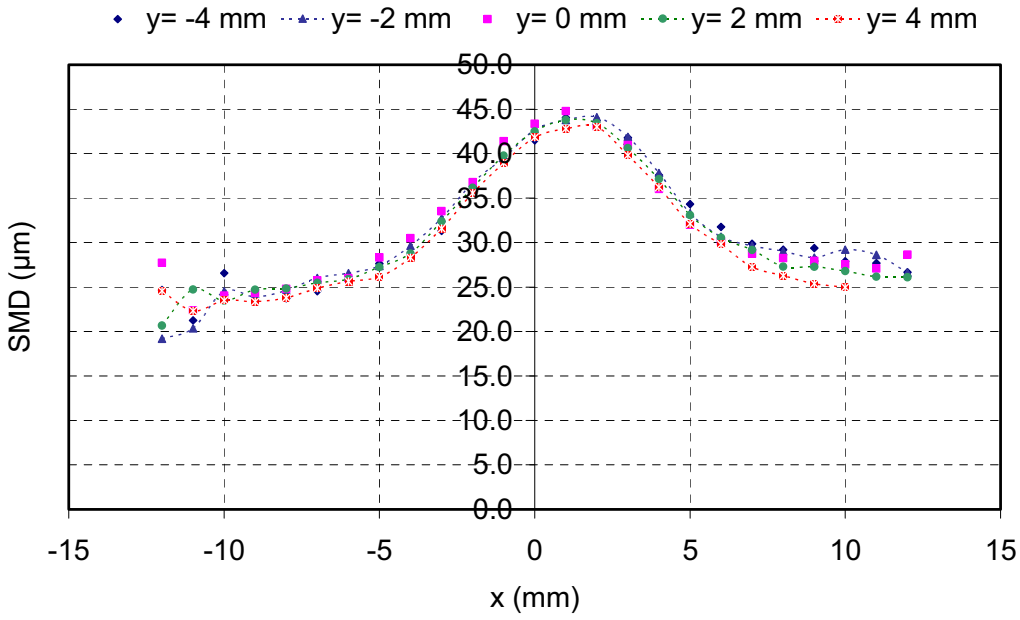

(b) 4mm prefilming airblast atomiser

Fig. C.1 Local SMD profiles along the span of atomisers at P_a = 4 bar and V_a = 60 m/s (Z = 90 mm)

Spanwise Variation of Mean Velocity profiles

Figure C.2 shows the variation of mean and RMS velocity for both prefilming and nonprefilming airblast atomisers. The mean velocity is calculated based on the velocities of 40,000 droplets measured at each measurement location.

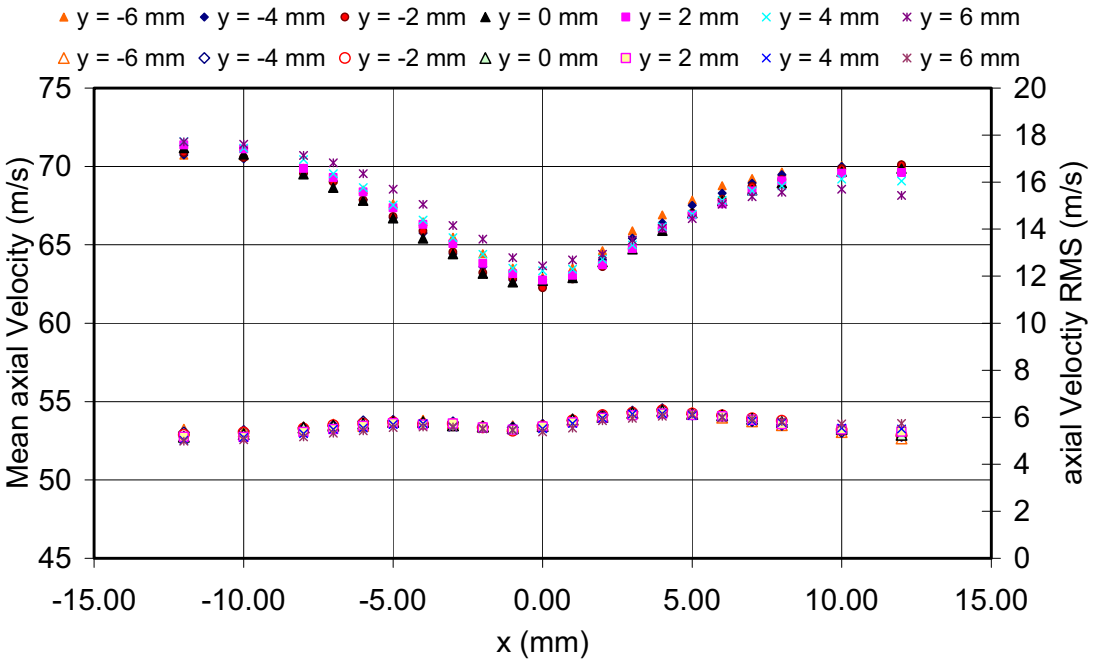

(a) nonprefilming airblast atomiser

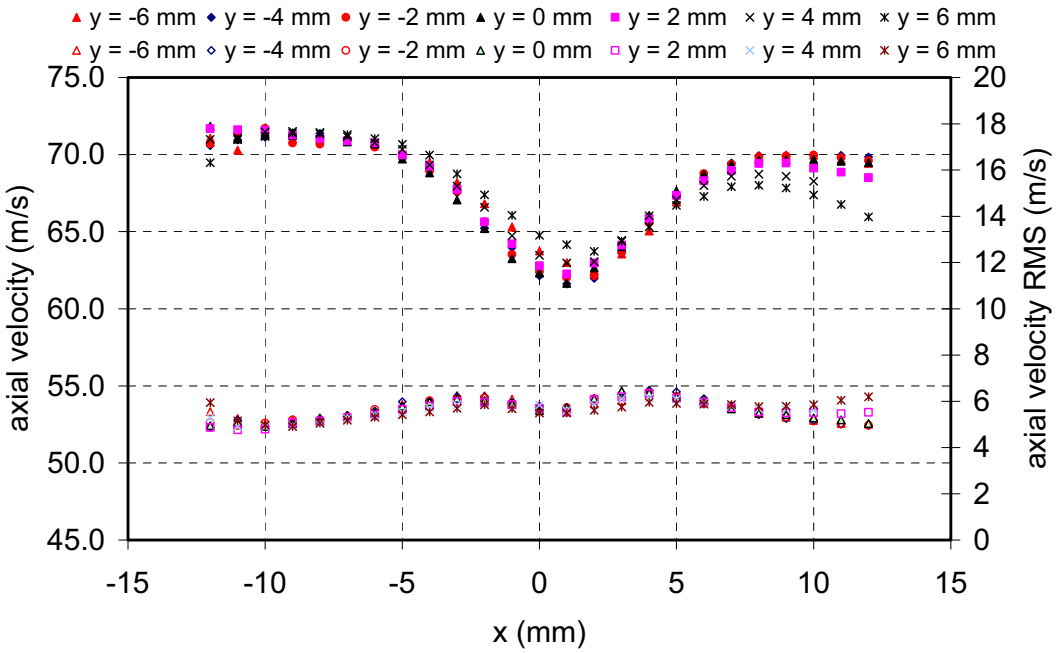

(b) 4mm prefilming airblast atomiser

Fig. C.2 Mean axial velocities along the span of atomisers at P_a = 4 bar and V_a = 60 m/s (Z = 90 mm)

The mean velocity is based on 'number count of droplets'. The profiles show that the velocity is symmetric across the Y-axis and the RMS velocities indicate that the fluctuating components of velocity are consistent along the entire span of the atomiser. The mean velocity does not necessarily indicate the velocity of mass flux of kerosene at

a location. In order to take into consideration the mass flow rate of kerosene at a location, weighted mean velocity based on the droplet volume is considered. Figure C.3 shows the volume weighted mean velocity profiles for the nonprefilming atomiser. These profiles too indicate that the mean velocity is symmetric along the whole span of the atomiser.

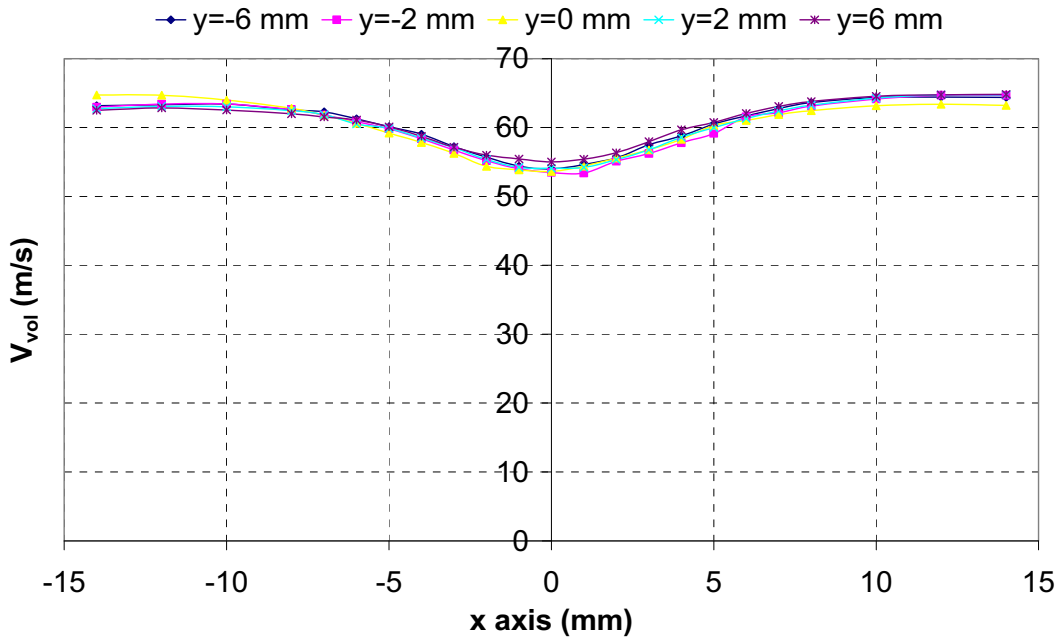

Fig. C.3 Volume weighted mean velocity profiles for nonprefilming airblast atomiser P_a = 4 bar and V_a = 60 m/s (Z = 90 mm)

APPENDIX D

EFFECT OF POSITIONING THE PDA OPTICS IN DENSE SPRAYS

Effect of Transmitting Optics offset angle on PDA measurements

As described in Figure 2.17, Chapter 2, the transmitting optics is positioned at an offset angle to the cross-sectional plane that is perpendicular to the axial flow direction. Even though the measurement of the droplet size is not affected by the offset angle of the transmitting optics, it has a direct influence on the measurement of the velocity of droplets. 2D-PDA measurements are performed in the present studies. The first component of the droplet velocity is measured along the axial flow direction (along Z-axis) and the second component is along the span of the atomiser (along Y-axis). The third component of the velocity (along X-axis) is in the cross-sectional plane perpendicular to the axial flow direction and perpendicular to the span of the atomiser. This component is not measured. The offset angle of the transmitting optics directly influences the measurement of the first and third component. Since it is unavoidable in the present studies to do measurements without positioning the transmitting optics at an offset angle, few measurements are performed to quantify the effect of the offset angle in the positioning of the transmitting optics on the velocity measurements. By performing PDA measurement at two offset angles, mean velocities of all three components can be calculated. In fact the initial purpose of measuring at two offset angles is to measure all three components of velocity. But, the difference in offset angles is too small for obtaining a reliable data on the third velocity component. Due to constraints at the experimental test facility, it was not possible to provide a large difference in the offset angles. The measurements at the two offset angles are used for comparison of relative differences in the axial velocity measurements and also as repeatability of the PDA measurements on two different days. Figure D.1 shows the mean axial velocity (along Z-axis) at two offset angles of 4.5° and 6.5°. The mean velocity measurements with 4.5° offset angle show consistently higher velocities in comparison with 6.5° offset angle. As can be observed from the graph, the difference in mean velocities at two offset angles is insignificant. This indicates that the chosen offset angles have minimal effect in the measurement of axial velocities of the droplets. The maximum difference of velocities between the two offset angles is less than 5%. Since, the 4.5° offset angle shows consistently the higher velocities, the actual velocities in the axial direction will be higher than the velocity measured with an offset angle.

Figure D.2 shows the effect of offset angles on global SMD for both prefilming and nonprefilming atomisers. Theoretically the effect of offset angle should have no

effect on SMD measurements. As can be observed in Figure D.2 (a) the maximum difference between SMD measurements at the two offset angles is 2.68% for nonprefilming atomiser which is minimal. The measurements are performed on two different days and hence the repeatability in the measurements is considered to be good. However, for the prefilming atomiser the maximum difference in measurements in 6 %. This is an acceptable range considering the wide range of parameters that affect PDA measurements.

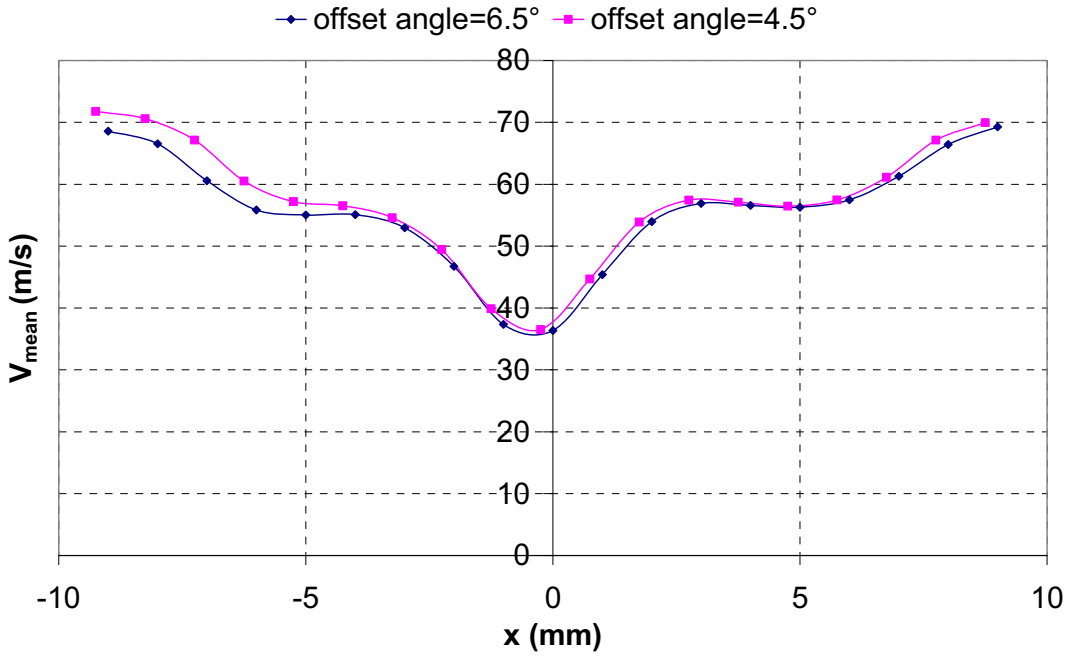

Fig. D.1 Effect of transmitting optics offset angle on mean velocity measurements (4 mm prefilming atomiser P_a = 2 bar, V_a = 60 m/s)

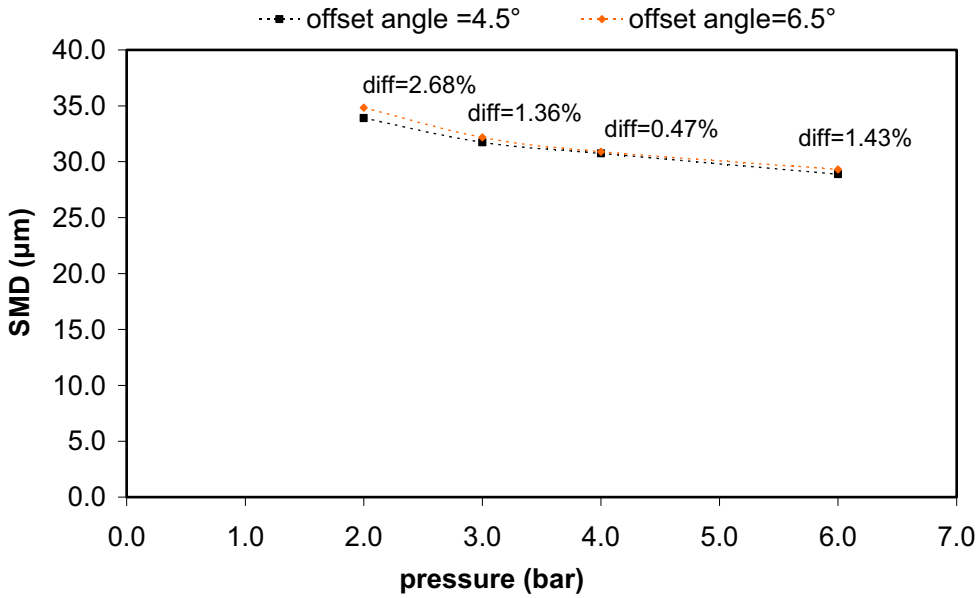

(a) nonprefilming airblast atomiser

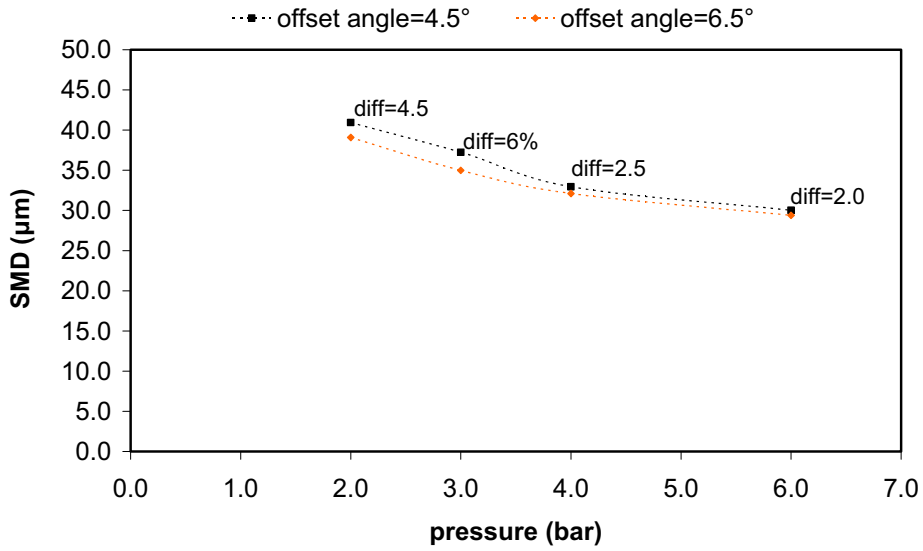

(b) 4mm prefilming airblast atomiser

Fig. D.2 Global SMD at V_a = 60 m/s at Z = 45 mm

Effect of the measurement volume positioning with respect to the spray on the spray results

PDA measurements are always difficult in dense sprays due to beam attenuation, beam steering and laser absorption in some cases. These can cause severe bias in PDA measurements. The reliability of PDA measurements also depends on the size of the measurement volume and the position of the transmitting optics with respect to the spray. The measurements are more reliable at the edges of the spray closer to transmitting optics than at the edge of the spray that is away from the transmitting optics, as shown in Figure D.3. An effort has been carried out to have an estimate of the

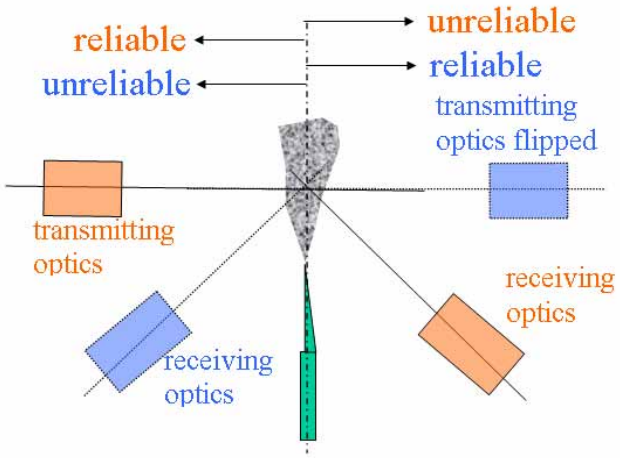

Fig. D.3 Reliability of PDA measurements

error involved in measurements at the regions of maximum volume flux of the spray. The transmitting optics is sequentially positioned on both sides of the spray and measurements are carried out along the X-axis to obtain profiles at y = 0 mm. The X-profiles are also obtained at several axial locations. The comparison of X-profiles by positioning transmitting optics on both sides at a given axial location gives roughly how deep into the spray one can measure accurately. The comparison of SMD profiles by positioning the transmitting optics on both sides of the spray was carried out only until axial distance of 45 mm. By measuring at several axial locations one can estimate how far from the atomiser reliable PDA measurements can be made in dense sprays.

Figure D.4 shows the effect of the position of the transmitting optics on validation rates at two axial locations, z = 10 mm and z = 45 mm, for both prefilming and nonprefilming atomisers. As can be observed in Figure D.4(a), for the 'toptics_Z = 10 mm' curve, which corresponds to the X-axis profiles at y = 0 mm and at axial location z = 10 mm for nonprefilming atomiser that the validation rates are as high as 85% at the edge of the spray closer to the transmitting optics at x = -8 mm. The validation rates decrease as the measurements are made deep into the dense spray.

At x = 0 mm, the validation rate drops to ~ 45%. By flipping the transmitting optics to the other side of the spray and repeating the measurements, similar validation rates are observed but now validation rates are higher on the other side of the spray. This indicates that the rejection rate of the Burst signals by the PDA processor increases as the measurements are made deep inside the spray in the near-field of the atomiser (z = 10 mm). At x = -5 mm and at z = 10 mm it can be observed that the difference in validation rates is as high as 60% when shifting transmitting optics. The difference in validation rates at the same location in the spray but with different relative location of transmitting optics is mainly due to the passing of laser beam being affected by the dense spray. The dense spray causes a 'beam steering effect' and affects the beams crossing in the measurement volume. If the beam steering effect is high then the beam crossing in the measurement volume depends on the droplet size distribution and can lead to bias towards droplet size measurements. Also, the poor validation rates lead to bias towards relatively larger droplets. This is because SNR is higher for large droplets and there are relatively less affected by the beam steering effect. As the measurements are made further downstream of the atomiser at z = 45 mm, the spray density decreases and this increases the validation rates. The validation rates are ~ 60% (at z = 45 mm, x = 0 mm) irrespective of the positioning on transmitting optics on either side of the spray. Also the difference in validation rates at x = -5 mm decreases to ~ 20%. The validation rates of 60% in the maximum dense spray region are considered to be in an acceptable range. This is based on consistency achieved in measurement of droplet mean diameters at this axial location (z = 45 mm) and beyond. As measurements are made further downstream of the atomiser z > 45 mm, the validation rates increase due to the decrease in spray density. The variation in droplet mean diameters is marginal due to dispersion effects of the spray. A similar behaviour can be observed for the 4 mm prefilming atomiser as shown in Figure D.4 (b). However, it has to be known whether the rejected burst signals by the PDA processor is only due to the beam steering effect, spray density or due to the presence of non-spherical particles. The details of the presence of the non-spherical particles are explained in Chapter 4.

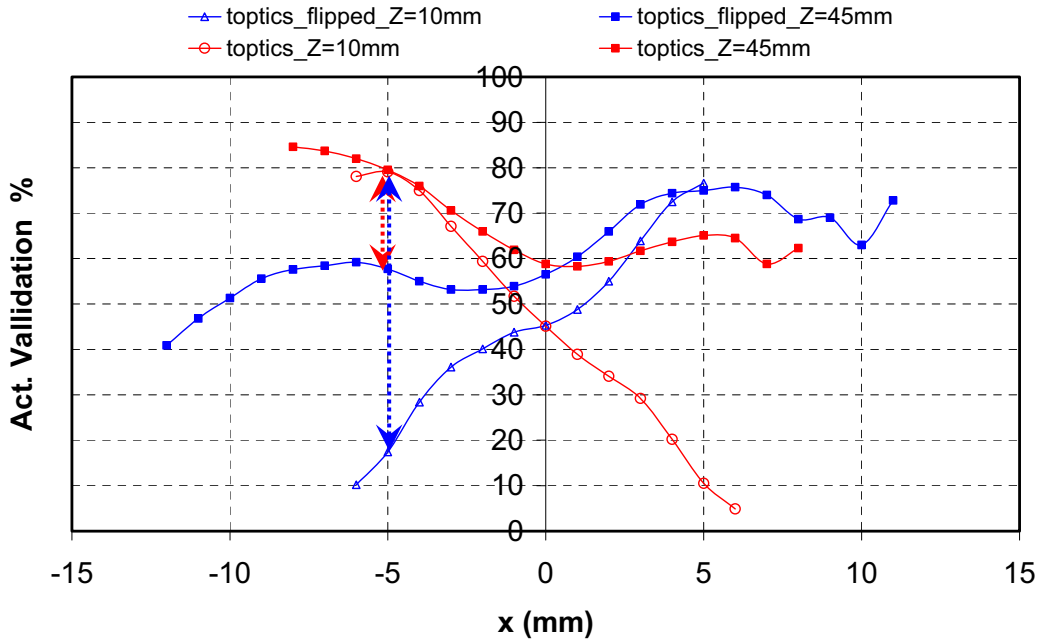

(a) nonprefilming airblast atomiser

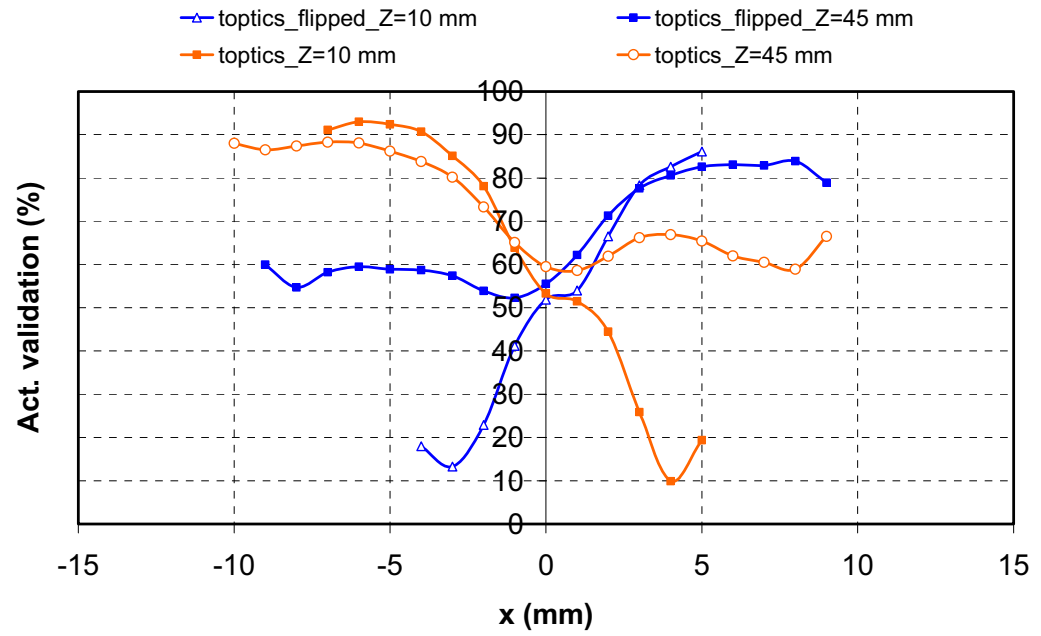

(b) 4mm prefilming airblast atomiser

Fig. D.4 Effect of spray density on validation percentage at P_a = 3 bar and V_a = 60 m/s

These effects of positioning of transmitting optics will have a significant effect on the droplet size measurements and on the overall analysis of the comparison of spray characteristics of the atomisers. As explained earlier, the key factor that has to be known is how deep inside the spray one can get reliable droplet size measurements and how far away from the atomiser. Figure D.5 shows the effect of positioning of the transmitting

optics on SMD profiles at two different axial locations for both the prefilming and the nonprefilming atomiser. At z = 10 mm, three curves are drawn. The curves with solid lines indicate the actual PDA measurements performed by positioning the transmitting optics on both sides of the spray. The dotted curve is just a representation of the PDA measurements performed with 't_optics_Z = 10 mm' position but with X-axis flipped to observe whether the PDA measurements coincide with the measurements performed by flipping the transmitting optics to the other side of the spray. From the curves it is clear that the bias in PDA measurements at the far end of the spray is due to beam steering effect. The reasoning is already given in earlier paragraphs. The SMD profiles measured on the side of the transmitting optics are lower compared to the far side of the spray indicating the bias in PDA measurements is towards larger droplets. As beam steering is more dominant on the far side of the spray, the beam crossing is minimal in the measurement volume. Only large droplets are recognised as they have higher SNR. This is also confirmed by low validation rates as explained earlier. At the far-field of the atomiser, z = 45 mm, the variation in SMD measurements is less affected by the position of the transmitting optics as the two solid lines have identical profiles. The difference in SMD measurements at x = ±3 mm for nonprefilming atomiser is ~ 5.6% at z = 45 mm and ~ 28% at z = 10 mm. The difference in SMD measurements at x = ±3 for prefilming atomiser is ~ 14% at z = 45 mm and ~ 47% at z = 10 mm. The black curves indicate how the actual SMD profiles probably should look like for the spray. The curve is drawn by considering each half of the spray closer to transmitting optics. However there is an amount of uncertainty in SMD measurements in the middle of the spray which is the limitation of PDA measurements in dense sprays.

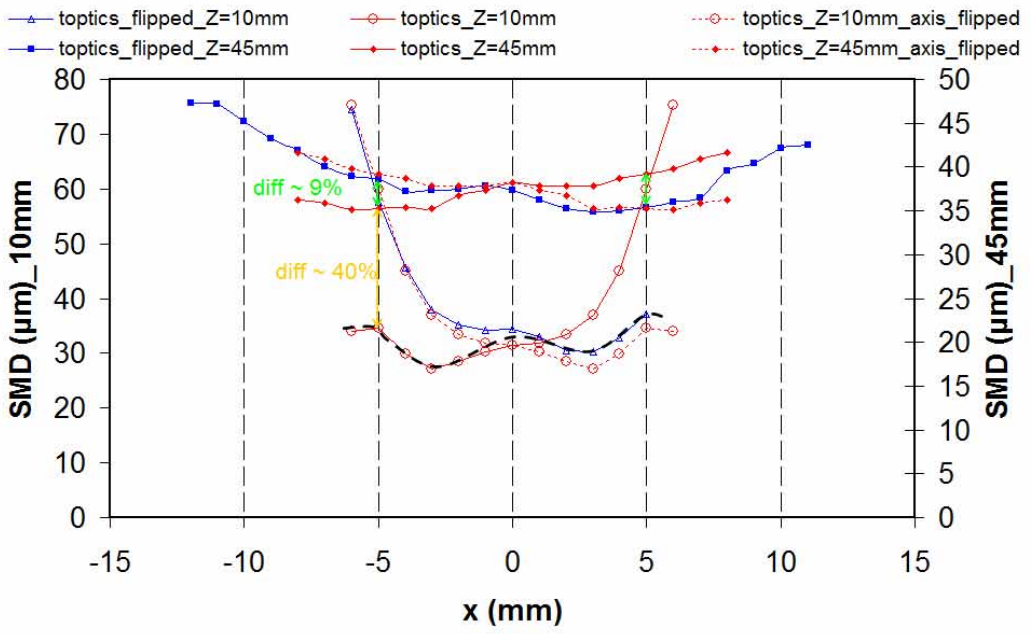

(a) nonprefilming airblast atomiser

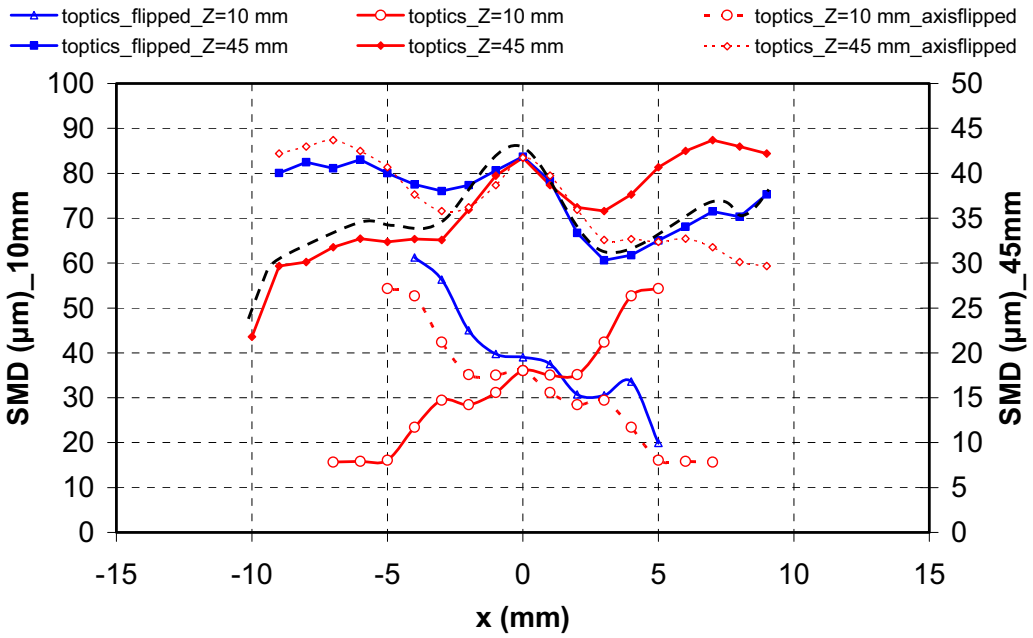

(b) 4mm prefilming airblast atomiser

Fig. D.5 Local SMD X-profiles at two axial locations at P_a = 3 bar, V_a = 60 m/s

The question which has to be addressed is, if for the calculation of the global SMD only the half-width of the spray is considered instead of the full-width of the spray, will there be any effect on the global SMD? This is necessary as beyond the certain region in the spray the PDA measurements seem to be very much dependent on the position of the transmitting optics and location in the spray. This is also important in the present context as the nonprefilming atomiser is symmetric along the centre plane whereas the 4 mm prefilming atomiser is asymmetric because of the prefilming surface. For the nonprefilming atomiser, a volume flux weighted averaging of the half-width of the spray is sufficient to calculate the global SMD. However, as discussed in chapter 3, the primary breakup mechanism is different for both of the atomisers hence there is the question if there is an effect on global SMD for prefilming airblast atomiser when only the half width of the spray is considered? Usually volume flux is relatively low at the edges of the spray. Table 4.1 shows the effect of considering half-width and full-width of the spray for the calculation of the global SMD for both the nonprefilming and the prefilming atomiser at various operating conditions for z = 45 mm. As can be observed the difference is less than ± 2%. The effect of the bias in PDA measurements on one edge of the spray has minimal effect on global SMD calculations. This is due to the low volume fluxes of spray involved in the regions where the PDA measurements show bias. Even though the breakup mechanism for both atomisers is different, the spray dispersion is significant and plays a crucial role in the droplet distribution in the far-

field of the atomiser. In the present studies, for calculating global SMD's only the half width of the spray is considered.

z = 45 mm		nonprefilming atomiser		
P_a (bar)	**V_a (m/s)**	**(half-width) GSMD**	**(Full-width) GSMD**	**Difference (%)**
3.0	40.0	49.7	50.4	-1.52
6.0	40.0	48.2	47.9	0.40
3.0	60.0	36.6	37.2	-1.78
6.0	60.0	33.6	33.5	0.02
3.0	90.0	27.3	27.0	1.00
6.0	90.0	24.0	23.8	0.88

z = 45 mm		4mm prefilming atomiser		
P_a (bar)	**V_a (m/s)**	**(Half-width) GSMD**	**(Full-width) GSMD**	**Difference (%)**
3.0	40.0	54.9	54.7	0.37
6.0	40.0	48.7	48.0	1.47
3.0	60.0	38.7	38.3	1.07
6.0	60.0	32.1	31.9	0.41
3.0	90.0	25.2	25.1	0.53
6.0	90.0	21.5	21.6	-0.68

Table D.1 Effect of considering half- and full-width of spray for global SMD calculation

Curriculum Vitae

Personal Details

Name	Umesh Chandra
Surname	Bhayaraju
Nationality	Indian
Date of Birth	18th Nov 1975
Gender	Male
E-mail	Umesh.Bhayaraju@gmail.com

Education

MS (Aero), IIT Madras, India, 2003-2000

BE (Mech), Osmania University, India, 1997-1993

Higher Secondary School, Gautami Jr. College, 1993-1991

Secondary School, HVS Public School, 1991-

Work Experience

Marie Curie Experienced Researcher, *Cambridge University,* Sept. 2007-working on cooling effects on Thermo-acoustic instabilities

Mitarbeiter, *DLR (German Aerospace Centre), Germany,* 2003-2007, characterisation of fuel placement of dense sprays emerging from airblast atomiser at elevated pressures and temperatures

Research Scholar, *IIT Madras 2000-2003,* worked on high speed mixing studies in supersonic flows in scramjet combustors

Fellowships & External Recognitions

Marie-Curie Fellowship under RTN program, 2007-

Marquis Who's Who in Science and Engineering, Sept 2006

Research Assistant Fellowship from IIT Madras, 2000-2003